Dissertation
submitted to the
Combined Faculty of Mathematics, Engineering and Natural Sciences
of Heidelberg University, Germany
for the degree of
Doctor of Natural Sciences

Put forward by
Aleksandr V. Boitsov

born in: Kirovsk, Leningradskaya obl., Russia
Oral examination: 24-07-2025

Relativistic scaling method for the numerical simulation of the x-ray strong field ionization

Referees: Prof. Dr. Christoph Keitel
Prof. Dr. Thomas Gasenzer

Abstract

In this thesis, the coordinate scaling method, previously developed for the numerical solution of the time-dependent Schrodinger equation, is generalized for the numerical treatment of the time-dependent Dirac equation (TDDE) and has been applied for the atomic ionization problem in relativistically strong laser fields. To enable the use of the scaling method in relativistic settings, the Foldy-Wouthuysen (FW) transformation is employed within the quasiclassical approximation, reducing TDDE to the square root Klein-Gordon-like equation. The method has been tested on the example of a 1D problem of the 1D atom exposed to a laser field, demonstrating its computational advantage over the standard direct implementation of the TDDE solution, especially in the case of an applied non-uniform mesh. Next, the method in the 2D form has been applied to investigate the strong field ionization of an atom in a XUV laser field in the stabilization regime in the nondipole domain. The pulse duration effect leading to the periodic modulation of the ionization yield has been revealed with the numerical solution and intuitive explanations have been advanced in both dipole and nondipole cases.

Zusammenfassung

In dieser Doktorarbeit wird die Koordinatenskalierungsmethode, die zuvor für die numerische Lösung der zeitabhängigen Schrödingergleichung entwickelt wurde, für die numerische Behandlung der zeitabhängigen Diracgleichung (ZDG) verallgemeinert und für das Problem der Atomionisation in relativistisch starken Laserfeldern angewendet. Um die Skalierungsmethode in relativistischen Umgebungen nutzen zu können, wird die Foldy-Wouthuysen (FW)-Transformation innerhalb der quasiklassischen Näherung verwendet, wodurch ZDG auf die Quadratwurzel einer Klein-Gordon-ähnlichen Gleichung reduziert wird. Die Methode wurde am Beispiel eines 1D-Problems eines 1D-Atoms getestet, das einem Laserfeld ausgesetzt ist. Dabei zeigte sich ihr rechnerischer Vorteil gegenüber der standardmäßigen direkten Implementierung der ZDG-Lösung, insbesondere im Fall eines verwendeten nicht-uniformen Gitters. Anschließend wurde die Methode in der 2D-Form angewendet, um die Starkfeldionisation eines Atoms in einem EUV-Laserfeld im Stabilisierungsregime im Nicht-Dipolbereich zu untersuchen. Der Impulsdauereffekt, der zur periodischen Modulation der Ionisationsausbeute führt, wurde mit der numerischen Lösung aufgedeckt und es wurden intuitive Erklärungen sowohl für Dipol- als auch für Nicht-Dipol-Fälle vorgelegt. [1]

---

[1] Die Zusammenfassung wurde mit hilfe von DeepL Übersetzer übersetzt.

Contents

Chapter 1

Introduction

Strong-field ionization is the basic process triggering phenomena in attoscience [1, 2]. With the present advancement of laser techniques, intensities approaching 10^{23} W/cm^2 have been attained [3], and intensities allowing the relativistic regime are routinely achievable. In a relativistically strong laser field, the electron oscillatory velocity approaches the speed of light, which for infrared lasers, with a wavelength of about 1 μm, is the case at a laser intensity exceeding 10^{18} W/cm^2 [4]. The experimental investigation of the relativistic strong-field ionization has already quite long history [5–11]. Recently, the high-precision measurement technique allowed even to observe nondipole (weakly relativistic) effects at lower intensities [12–17].

Generally, strong field ionization is governed by two independent parameters [18], which can be chosen to be the Keldysh parameter $\gamma = \sqrt{I_p/2U_p}$ and $\zeta = U_p/\omega$, where I_p is the ionization energy of the atom, and $U_p = E_0^2/(4\omega^2)$ is the free electron oscillatory energy in the laser field, where E_0 is an electric field strength, and ω is the laser frequency. Depending on these parameters the ionization can be broken down into a few regimes. In low frequency infrared or mid-infrared laser fields when $\hbar\omega \ll I_p$, the strong field ionization is dubbed as multiphoton ionization at low laser intensities when $\gamma > 1$ and the ionization occurs by the absorption of multiple photons. This regime is perturbative when $\gamma \gg 1$. Vice versa, for the large intensities $\gamma \ll 1$, the so called tunnel ionization unfolds, in which an electron tunnels through the combined effective atomic-laser potential. Tunneling ionization is fully nonperturbative process.

The strong field ionization is significantly modified in a high frequency regime $\hbar\omega > I_p$. While the parameters γ and ζ still delimit the nonperturbative regime $\gamma < 1$ and/or $\zeta > 1$, the physical interpretation of underlying phenomena is modified. In particular, it is known that at high laser frequencies the atomic stabilization phenomenon occurs, whereby the ionization rate decreases as the laser intensity increases. The latter takes place the free electron oscillation amplitude in a laser field $\alpha = E_0/\omega^2$ exceeds the atomic potential size $\sim a_B$, with the Bohr radius a_B. In the systems, studied in the thesis, $\hbar\omega \gg I_p$ and U_p spans from $U_p \sim I_p$ to $U_p \gg Ip$. This allows us to observe a wide range of the phenomena, including the stabilization regime in the dipole cases, which breaks by the influence of the nondipole effects. The nondipole effect is the relativistic v/c effect which includes the influence of the laser magnetic field on the process dynamics. It enters into play when the parameter $\xi = E/(c\omega) \sim 1$, i.e. when the free electron oscillatory velocity in the laser field becomes comparable with the speed of light.

It is worth noting that the single active electron approximation (SAE) approximation [18] is quite popular for the theoretical and numerical treatment of strong field ionization phenomena, capturing in many cases the main essence of the processes while neglecting electron correlation effects during ionization [19]. In this work we will discuss the ionization of hydrogen-like ions, such as He^{+}, Li^{2+} or Be^{3+}, when SAE is an exact approach.

While analytical theories for the treatment of strong-field processes in the relativistic regime are available, such as the imaginary-time method [20], and the strong-field approximation [21], they have known limitations, not including the Stark-shift and atomic polarization, which becomes important when approaching the over-the-barrier ionization regime, see e.g. [22–24], and numerical solutions of the Dirac and Klein-Gordon equations are highly desirable [25] which, however, are computationally very demanding in practice. Indeed, the treatment of solutions with both negative and positive energies requires a very small numerical propagation time step $\Delta t \sim \hbar/mc^2$, with the speed of light c, the electron mass m, and the Planck constant $\hbar$. Moreover, in the case of relativistic ionization, one expects ionized electrons to have large momenta $p \sim mc$, accommodating of which requires a small spatial step size of the grid $\Delta x \sim \hbar/mc$. These two circumstances complicate the numerical solution and have been addressed from different perspectives.

Over time, different techniques to solve time-dependent Dirac equation (TDDE) have been developed, such as the pseudo-spectral method and method of characteristics, see e.g. Ref. [26] for the comparison. To reduce computational efforts, time integrating procedures of 4th order were developed [27–32]. For the investigation of spin effects in strong laser fields with highly-charged ions in a weakly relativistic regime, direct numerical solution of Pauli equation was applied [33–35]. Direct solutions of TDDE for a simple 1D relativistic ionization problem are analyzed in Refs. [36, 37]. The 2D case, including spin effects, has been also treated in different ways, using the split-operator pseudo-spectral approach [24, 38, 39], Krylov-Arnoldi type integrator [40], and applied for the comparison of solutions of the TDDE and Klein-Gordon equation (KGE) in the high frequency regime [41, 42].

In recent years, increasing computing power enabled 3D simulations within different direct approaches via separation into radial and angular components of the wavefunction. In Ref. [43], a time-dependent close-coupling method was developed. An approach based on the spectral expansion in field-free eigenstates, where the radial wavefunctions are expressed on a B-spline basis, was applied in Ref. [44]. In Ref. [45] an envelope approximation was elaborated to include multipole effects from the full laser field. A procedure based on the relativistic generalization of the matrix iteration method was proposed in Ref. [46]. In Ref. [47], a modified generalized pseudospectral (GPS) method was used. A direct solution of TDDE in the high-intensity x-ray regime was obtained in Ref. [48].

Some of the methods were aimed at the reduction of computational complexity by introducing alternatives to the direct solving of TDDE. Among them are approaches, employing the KGE [22] or square root Klein-Gordon equation (SKGE) [49]. In Ref. [50], it was proposed to evolve the envelope of the wave function, rather than solving standard TDDE. Other approaches harnessed methods, previously proved useful for the solution of the time-dependent Schrodinger equation (TDSE), to facilitate the solution of TDDE. For instance, in [51] a method of complex coordinate scaling [52] was employed for the solution of TDDE. The use of the method of absorbing potentials [53] was discussed for TDDE in Ref. [54].

However, one of the advantageous approaches to TDSE, namely, the so-called method of scaled coordinates, has not been so far implemented in the relativistic realm. The method was firstly introduced in a different context in Ref. [55] and later elaborated for a strong-field ionization problem via TDSE in Refs. [56–58]. The method consists of two steps. First of all, one introduces an ansatz with a kinetic phase, resembling a free solution, which cancels out the highly oscillating phase of the numerical solution. As a result, rather than solving TDSE for a highly oscillating wave function, one solves a TDSE-like equation for a presumed smooth function. Second, a time-dependent coordinate scaling is applied, aiming to gradually expand the simulation box. Thus, the approach of the scaled coordinates resolves the two problems that are similar in relativistic and nonrelativistic cases: high oscillations of the wavefunction and limited size of the simulation area. One more advantage of the method is the direct access to the spectrum, as the coordinate dependence of the wavefunction in far-field mimics the asymptotic momentum distribution. However, the extension of the scaling method to the relativistic regime meets an additional problem. The relativistic wavefunction contains fast oscillations corresponding to the virtual transitions between positive and negative energies, which should be coped with to reduce the TDDE solution to the numerical simulation of the slow oscillating wavefunction.

In this thesis an author numerically investigates the ionization process of a one electron two-dimensional atom in a relativistically strong field of a plane electromagnetic wave. In order to accomplish this task, the method of scaled coordinates for the application to TDDE was developed. The method utilizes a previously known Foldy-Wouthuysen (FW) transformation, which is implemented in the quasiclassical approximation, derived by Silenko [59–61], reducing TDDE to the square-root Klein-Gordon-like equation. This transformation makes it possible to remove virtual transitions between positive and negative energies and to enable removing fast oscillations in the wavefunction. Such an application of FW in Silenko's form to the relativistic ionization problem was proposed for the first time and was thoroughly tested on the 1D example. Also, an efficiency of the proposed approach was examined in comparison to the regular procedures to the TDDE and SKGE solving, establishing the possible advantages.

The developed approach was applied to the solution of the two dimensional ionization. This part of the work has a few components. First, an influence of the non-dipole effects was examined and singled out from the pure relativistic effects, such as mass shift. Second, a dependence of the ionization probability on the pulse duration was studied. The study reveals, that the probability oscillates with the length of the pulse in both dipole and non dipole cases. However, it was proven, that these oscillations have different root causes, which were identified for the both cases. In addition, two simple models were presented to explain and estimate oscillations.

The structure of the thesis is the following. Chapter 2 begins with the presentation of the general approach to ODE and PDE time integration. Later, this theory is applied in the existing manner to the solution of both non relativistic and relativistic ionization problems. For the both cases, the minimal reproducible algorithms and their comprehensive analyses are given. In Chapter 3, the scaling coordinates approach is derived for the relativistic case and applied to the one dimensional ionization problem with respect to the standard direct solution of TDDE and TDSE. Chapter 4 deals with the application of the method, developed in Chapter 3, to the ionization of the two dimensional atom. The dependence of the ionization on the field strength in both dipole and nondipole case is presented and analyzed. Also, the dependence of the ionization probability on the laser pulse length is revealed and explained.

Chapter 2

Numerical treatment of time-dependent dynamics

2.1 Mathematical foundations of the time integration

Many physical problems are described by partial differential equations (PDEs). Although the particular form of such equations might be different, they still might belong to the same class. For example, time-dependent Schrodinger (TDSE), time-dependent Dirac (TDDE) and even heat equations are the so called parabolic equations. If we want to understand, how a certain system or a property evolves with time, we must write down an initial value problem (IVP) for such an equation and solve it. The numerical methods for the solution can be written in a general way for the entire classes and later specified for the particular cases. In this chapter, we will start from the general IVP for an ordinary differential equation (ODE) and then focus on the methods for the numerical treatment of the TDSE and TDDE.

Let us start with a simple IVP, which an ODE combined with an initial condition on function ψ

$$\begin{cases} \dot{\psi}(t) = H(t)\psi(t) \\ \psi(0) = \psi_0 \end{cases} \tag{2.1}$$

in which H is an operator. If the operator H does not depend on variable t, i.e. $H(t) = H_0$, then the solution of Eq. (2.1) is given by an exponent

$$\psi(t) = e^{tH_0}\psi_0. \tag{2.2}$$

However, if the operator H depends on time $H(t) \neq H_0$, then the solution becomes more sophisticated. In order to clarify this question, we can solve Eq. (2.1) iteratively.

First, we apply an integral operator to the both sides of Eq. (2.1)

$$\psi(t) - \psi(0) = \int_0^t H(t')\psi(t')dt' \tag{2.3}$$

and move ψ_0 to the right part

$$\psi(t) = \psi_0 + \int_0^t H(t')\psi(t')dt', \tag{2.4}$$

which yields an integral equation. Second, we use Eq. (2.4) to express $\psi(t')$ in the integral

$$\psi(t) = \psi_0 + \psi_0 \int_0^t H(t')dt' + \int_0^t H(t')dt' \int_0^{t'} H(t'')\psi(t'')dt''. \tag{2.5}$$

Third, we can continue this procedure by inserting Eq. (2.4) into Eq. (2.5)

$$\begin{aligned}\psi(t) = \psi_0 + \psi_0 \int_0^t H(t')dt' + \psi_0 \int_0^t H(t')dt' \int_0^{t'} H(t'')dt'' + \\ + \int_0^t dt' \int_0^{t'} dt'' \int_0^{t''} H(t')H(t'')H(t''')\psi(t''')dt'''.\end{aligned} \tag{2.6}$$

Let us take a closer look at the term

$$\int_0^t H(t')dt' \int_0^{t'} H(t'')dt'' = \int_0^t dt' \int_0^{t'} H(t')H(t'')dt''. \tag{2.7}$$

Here we have to deal with an integration over the triangle $t'' \in [0, t'],\ t \in [0, t]$, which can be converted to more useful integration over the square $t', t'' \in [0, t]$ via an introduction of a so called time-ordering operator τ

$$\tau H(t')H(t'') = \begin{cases} H(t')H(t''), & t' > t'' \\ H(t'')H(t'), & t' \le t''. \end{cases} \tag{2.8}$$

With this operator, we can express an integral over the square as two integrals over the triangle

$$\begin{aligned}\tau \iint_{[0,t]^2} H(t')H(t'')dt'dt'' = \int_0^t dt' \int_0^{t'} H(t')H(t'')dt'' + \int_0^t dt'' \int_0^{t''} H(t'')H(t')dt' = \\ = 2\int_0^t dt' \int_0^{t'} H(t')H(t'')dt''.\end{aligned} \tag{2.9}$$

The same procedure can be applied to all the other terms of Eq. (2.6), providing us with a series, which is, due to its similarity to Taylor's series of exponent, is by definition called "time ordered exponent"

$$\psi(t) = \left[1 + \tau \sum_{n=1}^{\infty} \frac{1}{n!} \int_{[0,t]^n} H(t_1)...H(t_n)dt_1...dt_n\right] \psi_0 \equiv \tau e^{tH}\ \psi_0 \tag{2.10}$$

In principle, a series Eq. (2.10) is not fast to compute. However, the exponent can be represented as Magnus expansion, which can be written as

$$\tau \exp\left[tH\right] = \exp\left[\sum_{m=1}^{\infty} \Omega_m(t)\right] \tag{2.11}$$

A few first $\Omega_m(t)$ terms of Magnus expansion are known in analytical form, but for our purposes we can right down just the first two of them

$$\Omega_1(t) = \int_0^t H(t')dt' \tag{2.12}$$

$$\Omega_2(t) = \frac{1}{2}\int_0^t dt' \int_0^{t'} [H(t'), H(t'')]dt''. \tag{2.13}$$

The terms of higher orders contain combinations of commutators of operators $H(t)$ at different times. It is clearly seen, that if operator H commutes with itself for all times $t' \in [0, t]$, then the solution for the problem Eq. (2.1) is provided just be the very first Magnus term

$$\psi(t) = \exp\left[\int_0^t H(t')dt'\right]\psi_0. \tag{2.14}$$

For a more complicated case $[H(t_1), H(t_2)] \neq 0$, one can still simplify the procedure. We can notice, that for the problem Eq. (2.1), a solution can be given by an evolutionary operator

$$\psi(t_1) = U(t_1, 0)\psi_0 \tag{2.15}$$

If we are interested in a solution at later time $t_2 > t_1$, then we can formally write down the solution as

$$\psi(t_2) = U(t_2, t_1)\psi(t_1) = U(t_2, t_1)U(t_1, 0)\psi_0. \tag{2.16}$$

Dividing an interval $[0, t]$ into N small subintervals with a step size $\Delta t = t/N$ and noticing, that an evolution operator U is given by the time ordered exponent Eq. (2.10), we arrive to the following solution of the problem Eq. (2.1)

$$\psi(t) = \left[\tau e^{\Delta t H}\right]^N \psi_0. \tag{2.17}$$

The Eq. (2.17) provides us with an efficient way to numerically calculate the solution. Indeed, the first Magnus term for each $\tau e^{\Delta t H}$ can be calculate via, for example, a midpoint rule

$$\Omega_1(\Delta t) = \int_{t_n}^{t_n+\Delta t} H(t')dt = H\left(t_n + \frac{\Delta t}{2}\right)\Delta t + \mathcal{O}(\Delta t^3), \quad t_n \in [0, t] \tag{2.18}$$

Spectacularly, the second Magnus term Eq. (2.13) turns out to be of $\mathcal{O}(\Delta t^3)$ order small

$$\Omega_2(\Delta t) = \frac{1}{2}\int_{t_n}^{t_n+\Delta t} dt' \int_0^{t'} [H(t'), H(t') + (t''-t')H'(t')]\, dt'' \sim \mathcal{O}(\Delta t^3) \tag{2.19}$$

Hence, remaining only the first Magnus term, we can write down the solution of problem Eq. (2.1) as

$$\psi(t) = \exp\left[H\left(t - \frac{\Delta t}{2}\right)\Delta t\right] \dots \exp\left[H\left(\frac{3\Delta t}{2}\right)\Delta t\right] \exp\left[H\left(\frac{\Delta t}{2}\right)\Delta t\right] \psi_0 + \mathcal{O}(\Delta t^2) \tag{2.20}$$

The question to address now is how to apply our individual propagator $e^{\Delta t H}$ to a function ψ. In principle, from the numerical point of view, we should choose an appropriate basis, in which operator H becomes a matrix and function ψ becomes c column-vector. Then, we can calculate the resulting matrix exponential by one of the existing approaches [25]. The simplest case is when H is a diagonal matrix, then

$$e^{\Delta t H}\psi = \begin{pmatrix} e^{\Delta t H_1} & 0 & 0 \\ 0 & \ddots & 0 \\ 0 & 0 & e^{\Delta t H_n} \end{pmatrix} \begin{pmatrix} \psi_1 \\ \vdots \\ \psi_n \end{pmatrix} \tag{2.21}$$

Also, when H is diagonalizable by a matrix F, that is $H = FAF^{-1}$, then it is easy to show, that

$$e^{\Delta t H}\psi = F \begin{pmatrix} e^{\Delta t A_1} & 0 & 0 \\ 0 & \ddots & 0 \\ 0 & 0 & e^{\Delta t A_n} \end{pmatrix} F^{-1} \begin{pmatrix} \psi_1 \\ \vdots \\ \psi_n \end{pmatrix} \tag{2.22}$$

If the matrix is not diagonalizable or the matrix F is complicated itself, then more general approaches can be used. On of the most popular is a Crank-Nicolson scheme, which is a special case of Padé approximant methods:

$$e^{\Delta t H}\psi = \left(1 + \frac{\Delta t}{2}H\right)\left(1 - \frac{\Delta t}{2}H\right)^{-1} \psi + \mathcal{O}(\Delta t^3) \tag{2.23}$$

the disadvantage of this approach is a need to calculate an inverse matrix. Apart from direct methods, such as Crank Nicolson, there exist iterative methods. One of the most famous of them is a Krylov subspace method.

One more way is a splitting approach. It is based on the idea, that an operator H can be decomposed as $H = T + V$, where each of parts can be relatively easy diagonalized. However, since T and V are matrices, one must use Baker–Campbell–Hausdorff formula to decompose a matrix exponential

$$e^{\Delta t H} = e^{\Delta t T} \cdot e^{\Delta t V} \cdot e^{\Delta t^2 [T,V]/2} \cdot \dots \tag{2.24}$$

Of course, computing this infinite series, involving commutators, is not computationally efficient. Therefore, one can use one of the numerous simplified expressions, whose comprehensive analysis can be found in [62]. One of such possibilities is a second order Verlet formula

$$e^{\Delta t(T+V)} = e^{\frac{\Delta t}{2}V} e^{\Delta t T} e^{\frac{\Delta t}{2}V} + \mathcal{O}(\Delta t^3) \tag{2.25}$$

more precisely, the error term in Eq. (2.25) is

$$\mathcal{O}(\Delta t^3) = \left(\frac{1}{12}[T,[T,V]] + \frac{1}{24}[V,[T,V]]\right)\Delta t^3. \tag{2.26}$$

An advantage of the splitting approach in application to the problems of quantum mechanics is described in the next section.

2.2 Time integration in the non relativistic quantum mechanics

2.2.1 The basics

In quantum mechanics, a problem Eq. (2.1) is usually written in the form

$$\begin{cases} i\hbar\dot{\psi}(\mathbf{r},t) = H(\mathbf{r},t)\psi(\mathbf{r},t) \\ \psi(\mathbf{r},0) = \psi_0(\mathbf{r}) \end{cases} \tag{2.27}$$

Depending on the particular setting, the way the Hamiltonian H looks like might be different. Non relativistic problems of time-dependent quantum mechanics, which also include ionization problems, are described by the Hamiltonian

$$H = \frac{1}{2m}\left(\mathbf{p} - \frac{e}{c}\mathbf{A}(\mathbf{r},t)\right)^2 + V(r), \tag{2.28}$$

written in the velocity gauge. Here, $V(r)$ denotes central potential of the atom core, which is usually Coulomb-like. The laser field is included by the vector potential $\mathbf{A}(\mathbf{r},t)$. The kinetic term $T = \frac{1}{2m}\left(\mathbf{p} - \frac{e}{c}\mathbf{A}\right)^2$ is written with the usage of the canonical momentum $\mathbf{p} \longleftrightarrow -i\hbar\partial_{\mathbf{r}}$ for the sake of simplicity.

In principle, the problem Eq. (2.27) with the Hamiltonian Eq. (2.28) can be numerically solved with the usage of any method from section 2.1. Before diving into details, it makes sense to introduce a so called ”minimal reproducible example”, i.e.

a simple procedure, which delivers the solution $\psi(\mathbf{r}, t)$ of Eq. (2.27) with a predetermined accuracy. Therefore, let us exhibit some basic ideas in a simple case of a 1D dipole (i.e. $A(t) \neq A(x, t)$) problem

$$H = \frac{1}{2m}\left(p_x - \frac{e}{c}A(t)\right)^2 + V(x). \tag{2.29}$$

To discretize the Hamiltonian Eq. (2.29), one may introduce a uniform grid $\{x_1 \dots x_{N_x}\}$ with N_x nodes and a spatial step size Δx. In this case, operators $p_x \longleftrightarrow -i\partial_x$ and $p_x^2 \longleftrightarrow -\partial_{xx}^2$ can be discretized using, for instance, finite differences:

$$f'(x_i) = \frac{f(x_{i+1}) - f(x_{i-1})}{2\Delta x} + \mathcal{O}(\Delta x^2) \tag{2.30}$$

$$f''(x_i) = \frac{f(x_{i+1}) - 2f(x_i) + f(x_{i-1})}{\Delta x^2} + \mathcal{O}(\Delta x^2) \tag{2.31}$$

Then, the kinetic part of the Hamiltonian Eq. (2.28) becomes

$$T = -\frac{\hbar^2}{2m\Delta x^2}\begin{pmatrix} -2 & 1 & & & 0 \\ 1 & -2 & 1 & & \\ & \ddots & \ddots & \ddots & \\ & & 1 & -2 & 1 \\ 0 & & & 1 & -2 \end{pmatrix} + i\frac{e}{c}A(t)\frac{\hbar}{m\Delta x}\begin{pmatrix} 0 & -1 & & & 0 \\ 1 & 0 & -1 & & \\ & \ddots & \ddots & \ddots & \\ & & 1 & 0 & -1 \\ 0 & & & 1 & 0 \end{pmatrix} + \frac{e^2}{2mc^2}A(t)^2 + \mathcal{O}(\Delta x^2) \tag{2.32}$$

and the potential term $V(x)$ is a simple diagonal matrix. As a result, the entire Hamiltonian $H = T + V$ comprises of a tridiagonal matrix. Such a matrix can be efficiently inverted via Thomas algorithm, making it possible to use Crank Nicolson method to propagate the solution.

While focusing on propagation of the wave function, we should never forget, that the problem Eq. (2.27) also requires boundary conditions on $\mathbf{r}$ in order to be well-posed. Here comes the contradiction: on the one hand, the size of the simulated area must ideally be infinite; on the other, computer memory can store only a limited number of the grid nodes N_x. Therefore, one must reasonably choose a simulation box of the size L_x and impose relevant boundary conditions. From the point of view of physics, we should define the behavior of the system on the boundaries of such a box. In our simple example Eq. (2.32), we implicitly introduced zero boundary conditions. Indeed, sub- and over-diagonal elements of the matrices in Eq. (2.32) with indices $\{1, 0\}$ and $\{N_x, N_x + 1\}$ are not written explicitly and thus considered to be 0. Overall, the topic of boundary conditions is of crucial importance for the solution of the ionization problem and will be discussed in detail in Section 2.2.3.

The procedure to solve the problem Eq. (2.27) with the Hamiltonian Eq. (2.29) wouldn't be complete without an error analysis. Indeed, so far we have introduced two parameters Δx and Δt, which define the accuracy of computations.

An error term, proportional to Δx^2, comes from the discretization of the derivatives Eq. (2.30) and makes the scheme a second-order with respect to Δx. Although the convergence order is now clear, a particular choice of the value $\Delta x = L_x/N_x$ requires a bit more of analysis. Intuitively, we must have enough grid nodes N_x to resolve the oscillations of the wave function ψ. Formally speaking, we can employ Fourier analysis to be more precise. A well-known relation between the step size of the spatial grid Δx and a maximum momentum $p_{\max}$, which can be resolved on the corresponding grid in Fourier space, reads $p_{\max} = \hbar\pi/\Delta x$. In practice, it leads to the choice $\Delta x = L_x/N_x \ll \hbar\pi/p_{\max}$, where $p_{\max}$ can be estimated beforehand. For instance, as $p_{\max} = \max\left[\frac{e}{c}A(t)\right]$.

An error term, proportional to Δt^2, comes from the two different sources. Firstly, midpoint integration rule and an abandoned second Magnus term deliver an error $\mathcal{O}\left(\Delta t^2 \ddot{H}(t)\right)$, which basically depends on how fast the Hamiltonian changes with time. In Eq. (2.29) the only term depending on time t is a vector-potential $A(t)$. Then, knowing its frequency ω, we can estimate $\Delta t \ll 1/\omega$. As can be seen, such a condition is relatively weak for the typical laser frequencies ($\omega \approx 0.05$ a.u. for the red laser and even for the $\omega \approx 2$ a.u. x-ray laser). Secondly, we introduce a global error term $\mathcal{O}\left(\Delta t^2 H^2\right)$ when approximating matrix exponential in Crank Nicolson form Eq. (2.23). This condition is more severe, than the first one, because it involves a module of the Hamiltonian. Therefore, Δt can be estimated as $\Delta t < m\hbar/p_{\max}^2$. A detailed analysis of the accuracy of the Crank Nicolson method can be found in [25].

2.2.2 Split operator approach

Of course, there are other algorithms, which may outperform the basic scheme, mentioned above. Since the Hamiltonian Eq. (2.28) consists of kinetic T and potential parts V, the respective problem Eq. (2.27) can be solved via the split operator approach, which has a few distinctive features in this case. Namely, we can notice, that the kinetic term T is diagonal in the momentum space. Switching to the momentum space from the coordinate space can be done very efficiently via Fast Fourier Transformation (FFT) [63]. This move allows us not to discretize the derivatives Eq. (2.30), because now, recalling the property Eq. (2.22), we can write down the matrix exponential for the kinetic part of the Hamiltonian as

$$e^{-iT\Delta t/\hbar}\psi = F \begin{pmatrix} e^{-i\Delta t(p_1-A(t))^2/(2m\hbar)} & & 0 \\ & \ddots & \\ 0 & & e^{-i\Delta t(p_{N_x}-A(t))^2/(2m\hbar)} \end{pmatrix} F^{-1} \begin{pmatrix} \psi_1 \\ \vdots \\ \psi_n \end{pmatrix} \tag{2.33}$$

with F being a matrix of the Fourier transform, such that $\hat{\psi}(p) = F\psi(x)$. Then, according to the split operator approach Eq. (2.25), an elementary propagation step becomes

$$e^{-iH\Delta t/\hbar}\psi(x,t) = e^{-i\frac{\Delta t}{2\hbar}V(x)}\ F^{-1}\ e^{-i\Delta t\frac{(p_x-A(t))^2}{2m\hbar}}\ F\ e^{-i\frac{\Delta t}{2\hbar}V(x)}\ \psi(x,t). \tag{2.34}$$

Eq. (2.34) is easy to deal with, because all the matrix exponentials there are in fact ones of diagonal matrices in respective spaces. This means, that the computing of the each matrix exponential becomes trivial (Eq. (2.21)) and an approximation of matrix exponential in any way (such as Crank Nicolson Eq. (2.23)) is no longer needed. Naturally, the computational complexity of the quantum evolution cannot disappear traceless. The transitions from the coordinate space x to the momentum p and back are done via the FFT operator F. Computing an application of the operator F to the function ψ is now the most time and resources computing part of the algorithm. Regarding the boundary conditions, they are now also implicitly set via the Fourier transformation. Indeed, the discrete (or fast, which nowadays is the same matter) Fourier transform implies, that the function being transformed is periodic. Therefore, although we do not set the boundary conditions explicitly, they are essentially periodic, because transformations F and F^{-1} are used at the each time step of the propagation.

Let us now examine in detail the accuracy and limitations of the split operator approach. First, the approach clearly has a better convergence with respect to the spatial step size Δx. Indeed, now we do not need an approximation of the derivatives Eq. (2.30), because in the momentum space a derivative transforms into a simple multiplication. It is known [25, 64], that such spectral methods enjoy "infinite order" or "exponential" convergence $\mathcal{O}\left((1/N_x)^{N_x}\right) \sim \mathcal{O}\left((\Delta x)^{N_x}\right)$. Of course, we still have a condition, which bounds a maximum resolved momentum with the step size $\Delta x = \hbar\pi/p_{\max}$. However, due to the very fast convergence, a condition for the particular choice Δx is not that strict $\Delta x \leq \hbar\pi/p_{\max}$. In practice, it means that for the spectral methods the number of grid points N_x is at least a few times smaller, then for finite differences methods.

Second, an error, related to the time step Δt, again comes from the two sources. An error from the mid-point integration is the same as in the previous case and yields a condition $\Delta t \ll 1/\omega$. Unlike in the Crank Nicolson method, we do not have an error due to the approximation of an individual elementary matrix exponential. Instead, we have an error Eq. (2.26) from the omitted terms while splitting the Hamiltonian Eq. (2.29)

$$\mathcal{O}(\Delta t^3) \sim p_{\max}^2 \Delta t^3. \tag{2.35}$$

which for the entire interval of integration $[0, t]$ gives $\mathcal{O}(\Delta t^2) \sim p_{\max}^2 \Delta t^2$. Hence, the condition on $\Delta t \ll m a_B / p_{\max}$.

As one can see, the splitting operator approach does not demand very small step sizes Δx and Δt. The main complexity of the method comes from the back and forth Fourier transformations of the wave function ψ. However, FFT complexity scales as $\mathcal{O}(N_x \log N_x)$, which is pretty moderate. Moreover, modern implementations of the FFT are very efficient and can be used in a simple and straightforward manner. All these facts make the splitting operator approach an efficient tool for the time propagation of the TDSE.

The splitting operator approach can be utilized for more complicated systems, too. Let us consider a 2D system, exposed to the plane electro-magnetic wave. The non-dipole Hamiltonian of such a system reads

$$H = \frac{1}{2m}\left(p_x - \frac{e}{c}A(t,z)\right)^2 + \frac{1}{2m}p_z^2 + V(r). \tag{2.36}$$

Let us divide the kinetic part $T = T_0 + T_1 + T_2$ into a few sub-parts

$$T_0 = \frac{1}{2m}(p_x^2 + p_z^2) \tag{2.37}$$

$$T_1 = -2\frac{e}{mc}A(z,t)p_x \tag{2.38}$$

$$T_2 = \frac{e^2}{mc^2}A(t,z)^2 \tag{2.39}$$

Here, the term T_1 does not involve spatial derivatives of $A(z)$, because operators p_x and $A(t,z)$ commute. If we define the 2D Fourier transform as $\hat{\psi}(p_x, p_z) = F_2\psi(x,z)$ and the 1D as $\tilde{\psi}(p_x, z) = F_x\psi(x,z)$ and $\tilde{\psi}(x, p_z) = F_z\psi(x,z)$, then the split operator approach can be written as

$$e^{-iH\Delta t/\hbar}\psi(x,z,t) = e^{-i\frac{\Delta t}{2\hbar}V(r)}\ F_2^{-1}\ e^{-i\Delta t T_0/\hbar}\ F_x\ e^{-i\Delta t T_1/\hbar}\ F_z\ e^{-i\Delta t T_2/\hbar}\ e^{-i\frac{\Delta t}{2\hbar}V(r)}\ \psi(x,t). \tag{2.40}$$

The estimations for the Δx and Δt, which were made earlier, remain valid also for the 2D case.

Although the Hamiltonian Eq. (2.36) and the splitting method Eq. (2.40) are mathematically correct, they are not flawless from the perspective of physics. The thing is, that non dipole effects $A = A(z)$ start manifesting themselves when the laser field becomes relativistically strong. As a rule, it is believed that such a regime is entered, when a ponderomotive (i.e. the nonrelativistic cycle-averaged quiver energy) energy U_p becomes comparable to the to the electron's rest energy

$$\frac{U_p}{mc^2} = \frac{e^2E^2}{4m^2c^2\omega^2} \sim 1 \tag{2.41}$$

Of course, for such parameters electron's motion can no longer be described in terms of non relativistic equations, such as TDSE. Therefore, a relativistic description is necessary, which implies an introduction of the Dirac equation or some other approximate approaches, such as Foldy-Wouthuysen equations (Section 3.1.2).

2.2.3 Initial and boundary conditions

So far, we have mentioned the question of the boundary conditions very briefly. However, this aspect is not of less importance, than the time propagation itself. In order to define correct boundary conditions, one should first understand the physics of the ionization problem.

At the initial moment, the system usually consists of a one electron atom at rest. The atom is characterized by the central potential, which is usually Coulomb-like. The initial state is taken as a ground state of the respective potential. Such initial state can be numerically computed by means of various techniques. One of the opportunities is an imaginary time propagation. This approach can be implemented via the methods, described above, such as Crank Nicolson or split operator approaches. The cornerstone of the method is a formal change of the variable $t \to -i\tau$ in Eq. (2.27)

$$\begin{cases} \hbar\dot{\psi}(\mathbf{r},\tau) = -H(\mathbf{r})\psi(\mathbf{r},\tau) \\ \psi(\mathbf{r},0) = \psi_0(\mathbf{r}) \end{cases} \tag{2.42}$$

The solution to the Eq. (2.42) can be expanded into the series

$$\psi(\mathbf{r},\tau) = \sum_n a_n\psi_n(\mathbf{r})e^{-\tau E_n/\hbar} \tag{2.43}$$

where ψ_n are eigenstates $H\psi = E_n\psi$ and E_n are respective energies. Since the ground energy is $E_0 < E_n$, then after the evolution with some imaginary time τ all the terms will be small, comparing to the $a_0\psi_0(\mathbf{r})e^{-\tau E_0/\hbar}$. Hence, we can extract $\psi_0(\mathbf{r})$ from the simulation results.

Other approaches consider stationary Schrödinger equation $H\psi = E\psi$ as a boundary value problem (BVP). Such mathematical problems have been extensively studied and as of today, there are many methods and programmes to solve general BVP. For instance, there is a MATLAB package MATSLISE [65], which is designed to solve Sturm-Liouville problem numerically. Conveniently, a stationary Schrödigner equation is a particular case of the general Sturm-Liouville problem. The programme MATSLISE implements constant reference potential perturbation method (CP-method), which allows us to obtain ground states even for the slow decaying potential like $V(r) \sim 1/r$.

With the initial wave function $\psi_0(\mathbf{r})$ at hand, we are ready to turn on the laser. The electro-magnetic field in a velocity gauge is introduced via the vector potential $\mathbf{A}(\mathbf{r}, t)$, which is for the case of the plane wave is represented as

$$\mathbf{A}(\mathbf{r}, t) = \mathbf{e}_x A_0 \cdot f\left(\omega\left(t - \frac{z}{c}\right)\right) \cdot \sin\left(\omega\left(t - \frac{z}{c}\right)\right), \tag{2.44}$$

where f is a smooth envelope function. There are some conditions on the vector-potential $\mathbf{A}$. First, the envelope function f must turn on and turn off the field relatively slowly. If f is a Gaussian, then its standard deviation τ must be $\tau > 2\pi/\omega$ and the time of the turn on and off must be at least a few τ. Second, usually an integral $\int_{-\infty}^{\infty} \mathbf{A}(t)dt = 0$. Such a condition is justified by the fact, that a classical free electron trajectory in dipole case is given by the formula

$$\alpha(t) = \frac{e}{mc}\int_{-\infty}^{t} A(t')dt'. \tag{2.45}$$

Therefore, if we want to study electron's motion in a potential V, then it is useful to have a "free electron's" offset to be zero. For the propagating laser wave, the condition should be fulfilled:

$$\int_{-\infty}^{\infty} E(t')dt' = 0. \tag{2.46}$$

During the interaction with the laser field Eq. (2.44), electron's motion consists of two main components. Along the $\mathbf{x}$ axis, an electron experiences a quiver motion with a frequency ω due to the periodic electric field $E = -\frac{1}{c}\dot{A}(t)$. Along the $\mathbf{z}$ axis, an electron drifts under the influence of the Lorenz force. In principle, in the absence of the central potential V, the drift has a constant average speed v_z [66]

$$v_z = c\frac{a_0^2/2}{1 + a_0^2/2} \approx \frac{c}{2}a_0^2, \tag{2.47}$$

where a_0 is a non dipole parameter $a_0 = E/(\omega c) = eA/(mc^2)$. Although, it also experiences small oscillations with frequency 2ω. If the potential V is present, then electron's motion is also influenced by the Coulomb force $-\nabla V$ and the trajectory could become oscillating with a period, much larger than $2\pi/\omega$. If we consider an electron not as a point-like particle, but as a wave packet, then during the interaction, the packet scatters, rescatters on the central potential and spreads. However, looking ahead, the most impact on the ionization have a turn on and turn off stages. Right after the interaction, an electron tends to scatter on the potential center, leaving most of the ionized part to travel into the $-z$ direction. To sum up, an electron remains quite localized during the interaction phase, but the ionized part of the wave function travels infinitely after the end of the pulse.

For most of the applications (such as a calculation of the ionization spectrum), one must perform the simulation for some long time after the end of the pulse. For the cases, addressed in this thesis, it is about $15 - 30\tau$. The problem is, that the simulation box is finite, but the motion of the ionized electron is infinite. As a result, a long grid size is required to accommodate the full ionized wavepacket, especially at high laser intensities. However, the large grid size makes it hard to store the grid in the computer memory and makes computations slow. For instance, if the split operator approach is used, then the computing time grows as $N \log N$, where N is a total number of the grid nodes. Therefore, a special attention must be aimed on the boundary conditions, so that they correctly keep the dynamics of the electron throughout the simulation and the simulation box size remains reasonable.

One of the straightforward approaches to the boundary conditions is to introduce an imaginary absorbing potential V_A

$$V(r) = -\frac{1}{r} + iV_A(r) \tag{2.48}$$

which absorbs the wave function on the edges of the simulation box [53]. This allows us to enforce zero or periodic boundary conditions. So, an absorbing potential V_A must be localized near the boundaries and have a smooth turn on, so that the wavefunction, approaching the edge of the box, is not reflected from V_A.

Another possible approach is a complex coordinate scaling [52]. An idea of the method is a smooth introduction of the complex phase θ into the coordinate x, starting from the certain (in general, large) distance R_0

$$x \to \begin{cases} x, & |x| < R_0 \\ e^{i\theta}(x \pm R_0) \mp R_0, & \mp x > R_0 \end{cases} \tag{2.49}$$

Such scaling is also sometimes referred as a "perfect absorber".

However, both methods, mentioned above, has disadvantages. Although they suppress a non-physical reflection of the wavefunction from the boundaries, the dynamics of the system will be lost, if an ionized electron reaches the boundary. Moreover, as can be seen from the analysis of the free Hamiltonian, the moving wavepacket far from the potential center after the end of the pulse can be propagated as

$$\hat{\psi}(\mathbf{p}, t) = e^{-i(t-t_0)p^2/(2m\hbar)}\hat{\psi}(\mathbf{p}, t_0). \tag{2.50}$$

Hence, the wave packet acquires an additional phase, proportional to the time of propagation t, which demands more grid nodes in physical space in order to resolve the oscillations. Therefore, a method of scaling coordinates was introduced. The method tackles both the kinematic oscillations and an infinite motion of the wavefunction.

2.2.4 Scaling coordinates method

The large range of the electron motion in the continuum after ionization is handled within the framework of the scaling coordinates by the introduction of a time-dependent coordinate scaling $x = R(t)\xi$, between the real space coordinate x, and a computational coordinate ξ, the scaling factor $R(t)$ satisfying conditions

$$R(0) = L, \; R(t) \xrightarrow[t\to\infty]{} vt, \tag{2.51}$$

where L is an initial box size and the parameter v should be chosen to correspond to the characteristic velocity (e.g. the group velocity) of the ionization wavepacket. In general, the particular choice of the intermediate time dependence of $R(t)$ is arbitrary. One of the common choices is [56]:

$$R(t) = \begin{cases} L & , \; t < t_0 \\ \sqrt[4]{L^4 + v^4(t-t_0)^4} & , \; t \geq t_0 \end{cases} \tag{2.52}$$

where t_0 is scaling's turn-on time. As a result of the scaling and the constant expansion $R(t)$ of the grid, the ionized wavepacket never reaches the boundary at a given rather small grid, which allows one to enforce any of the simple boundary conditions. Moreover, with a good choice of the parameters one can achieve a stationary wavepacket in the computational space ξ. How fast the wavepacket becomes stationary can be regulated by the parameter v, to be equal or greater than the fastest group velocity in the system.

The disadvantage of the coordinate scaling is that the core potential $V(\xi R(t))$ shrinks in computational space ξ. Hence, the number of grid nodes inside the core of the potential decreases with time. However, to resolve the dynamics of the bound state wavefunction correctly, the grid must always have a certain minimal amount of knots near the core. For this reason, either one has to have an excessive amount of knots at the beginning of the simulation, such that at the end there is a sufficient number of nodes near the core to sustain the potential V. Alternatively, this problem can be overcome by employing a non-uniform mesh, or by dynamical adding of knots.

The key idea of dealing with fast oscillations of the wavefunction due to the non-relativistic kinetic phase, was representing the wave function as a product of the fast oscillating $f(x,t)$ part and the smooth evolving one $\phi(x,t)$ [56–58]:

$$\psi(x,t) = \phi(x,t) f(x,t), \tag{2.53}$$

and in Fourier space

$$\hat{\psi}(p,t) = \hat{\Phi}(p,t)\hat{f}(p,t), \tag{2.54}$$

such that a Fourier transform $\hat{f}$ of f

$$\hat{f}(p,t) \xrightarrow[t\to\infty]{} e^{-i\frac{p^2}{2\hbar m}t}, \tag{2.55}$$

approaches a solution of the free electron TDSE as $t \to \infty$. In order to derive $f(x,t)$, one can write down the Fourier integral:

$$\psi(x,t) = \frac{1}{2\pi\hbar}\int_{-\infty}^{\infty} \hat{\Phi}(p,t) e^{-\frac{i}{2m\hbar}p^2 t} e^{+\frac{i}{\hbar}px} dp. \tag{2.56}$$

Since we consider Eq. (2.53) as an ansatz with two, in principle, arbitrary functions, it is sufficient to estimate the integral Eq. (2.56) using stationary phase approximation (SPA) [67]. The integrand in Eq. (2.56) has a saddle-point p_0 at large t: $p_0 = mx/t$, and SPA yields

$$\psi(x,t) \sim \hat{\Phi}\left(\frac{mx}{t}, t\right) e^{\frac{i}{2\hbar t}mx^2} + O\left(\frac{1}{\sqrt{t}}\right), \ t \to \infty \tag{2.57}$$

When R/t is replaced with $\dot{R}$ in the latter expression, it will read in scaled coordinates as

$$\psi(R\xi,t) \sim \hat{\Phi}\left(m\dot{R}\xi,t\right) e^{\frac{i}{2\hbar}mR\dot{R}\xi^2} + O\left(\frac{1}{\sqrt{t}}\right),\ t\to\infty \tag{2.58}$$

Thus, providing the fast oscillating term:

$$f(\xi R,t) \sim e^{i\frac{m}{2\hbar}R\dot{R}\xi^2}. \tag{2.59}$$

The choice of the phase above intuitively corresponds asymptotically ($t\to\infty$) to the kinetic phase of $(mv^2/2\hbar)t\xi^2$, with the characteristic velocity v. It is also seen from Eqs. (2.51) and (2.57), that

$$\xi \xrightarrow[R\to vt]{} \frac{p}{mv}. \tag{2.60}$$

Thus, the coordinate dependence of the wavefunction of the electron ionized part repeats the photoelectron asymptotic momentum distribution. This allows us to access the spectrum $|\hat{\Phi}|$ directly from the wavefunction $|\psi|$ with the substitution (2.60).

As a result, the function $f(x,t)$ incorporates high kinetic oscillations of the wavefunction, and the presumably smooth function $\phi(x,t)$ fulfills the following equation [58]:

$$i\hbar\frac{\partial\phi}{\partial t} = \left[-\frac{\hbar^2}{2mR^2}\frac{\partial^2}{\partial\xi^2} + V(R\xi,t) + \frac{m}{2}R\ddot{R}\xi^2\right]\phi. \tag{2.61}$$

The latter equation has two distinctive features, apart from the shrinking central potential $V(R\xi,t)$. Namely, an additional localized in time potential $\frac{m}{2}R\ddot{R}\xi^2$ and the decreasing with time kinetic term $\frac{\hbar^2}{2mR^2}\frac{\partial^2}{\partial\xi^2}$. The additional potential does not posses any computational difficulties as long as $\ddot{R}(t)$ is smooth (see Eq. (2.52)). In turn, the disappearing as $1/R(t)^2$ kinetic term guarantees, that the envelope function $\phi(R\xi,t)$ eventually becomes stationary and approaches $\hat{\Phi}(m\dot{R}\xi,t)$ as $R(t)\to vt$.

The latter equation can be numerically evolved with much smaller number of spatial grid nodes than the original TDSE. This is achieved by the fact that the function $\phi(x,t)$ is smooth comparing to the original function $\psi(x,t)$ and, consequently, we no longer need a small step size Δx to resolve its oscillations. Also, the total length of the box L is no longer should be large, because any wave packet with the group velocity v_g is stuck at the position. An example of the evolution of the free Gaussian package in scaled coordinates is demonstrated in [56, 57].

2.3 Time integration in the relativistic quantum mechanics

2.3.1 Time-dependent Dirac Equation

In case of the large laser intensities, i.e. larger than 10^{18} W/cm^2, the relativistic description of the ionization becomes absolutely necessary. This can be done by means of the Relativistic Quantum Mechanics. An evolution of the wavefunction, describing the one electron atom interacting with the field $\mathbf{A}(\mathbf{r}, t)$, is governed by time-dependent Dirac equation (TDDE)

$$i\hbar\dot{\psi}(\mathbf{r}, t) = \left[mc^2\beta + c\alpha\left(\mathbf{p} - \frac{e}{c}A(t)\right) + V(\mathbf{r})\right]\psi(\mathbf{r}, t) \tag{2.62}$$

Although Eq. (2.62) formally has the same appearance as Eq. (2.27), it has a more complicated structure. First of all, TDDE governs both particles with positive (electrons) and negative (positrons) energies. Therefore, the wave function $\psi(\mathbf{r}, t)$ is no longer a scalar function, but a vector. In 1D, where the spin is naturally absent, $\psi(\mathbf{r}, t)$ is a two-component vector (spinor). In 2D and 3D both electrons and positrons have a spin, so this degree of freedom is taken into account by the further expansion of $\psi(\mathbf{r}, t)$, making it a 4-component vector (bispinor). This is why coefficients α become 4×4 matrices

$$\alpha_x = \begin{pmatrix} 0 & 0 & 0 & 1 \\ 0 & 0 & 1 & 0 \\ 0 & 1 & 0 & 0 \\ 1 & 0 & 0 & 0 \end{pmatrix}, \quad \alpha_y = \begin{pmatrix} 0 & 0 & 0 & -i \\ 0 & 0 & i & 0 \\ 0 & -i & 0 & 0 \\ i & 0 & 0 & 0 \end{pmatrix} \quad \alpha_z = \begin{pmatrix} 0 & 0 & 1 & 0 \\ 0 & 0 & 0 & -1 \\ 1 & 0 & 0 & 0 \\ 0 & -1 & 0 & 0 \end{pmatrix} \tag{2.63}$$

$$\beta = \begin{pmatrix} 1 & 0 & 0 & 0 \\ 0 & 1 & 0 & 0 \\ 0 & 0 & -1 & 0 \\ 0 & 0 & 0 & -1 \end{pmatrix}, \tag{2.64}$$

which also satisfy certain commutative relations

$$\alpha_i^2 = \beta^2 = 1, \quad \{\alpha_i, \alpha_j\} = 2\delta_{i,j}, \quad \alpha_i\beta + \beta\alpha_i = 0. \tag{2.65}$$

Also, matrices α_i can be written by means of Pauli matrices σ_i

$$\alpha_i = \begin{pmatrix} 0 & \sigma_i \\ \sigma_i & 0 \end{pmatrix}, \quad \sigma_x = \begin{pmatrix} 0 & 1 \\ 1 & 0 \end{pmatrix}, \quad \sigma_y = \begin{pmatrix} 0 & -i \\ i & 0 \end{pmatrix}, \quad \sigma_z = \begin{pmatrix} 1 & 0 \\ 0 & -1 \end{pmatrix}, \tag{2.66}$$

In case of the free Hamiltonian in Eq. (2.62), i.e. when $V = 0$ and $\mathbf{A} = 0$, one can write down the free solutions of TDDE

$$\begin{aligned}\hat{\chi}_+^{u,d} &= \frac{1}{\sqrt{2E(E+mc^2)}}\begin{pmatrix} s^{u,d}(E+mc^2) \\ s^{u,d}c\sigma\cdot\mathbf{p}\end{pmatrix} e^{-i\frac{mc^2}{\hbar}t\sqrt{1+\frac{p^2}{m^2c^2}}} \\ \hat{\chi}_-^{u,d} &= \frac{1}{\sqrt{2E(E+mc^2)}}\begin{pmatrix} -s^{u,d}c\sigma\cdot\mathbf{p} \\ s^{u,d}(E+mc^2)\end{pmatrix} e^{i\frac{mc^2}{\hbar}t\sqrt{1+\frac{p^2}{m^2c^2}}}.\end{aligned} \tag{2.67}$$

where indices + and − denote positive or negative energy states, indices u and d correspond to spin up and spin down states, respectively. Vectors s^u and s^d are orthogonal two-component unit vectors

$$s^u = \begin{pmatrix}1\\0\end{pmatrix}, \quad s^d = \begin{pmatrix}0\\1\end{pmatrix} \tag{2.68}$$

and E denotes a classical relativistic energy-momentum relation

$$E = mc^2\sqrt{1+\frac{p^2}{m^2c^2}}. \tag{2.69}$$

In 1D case Eq. (2.62) simplifies due to the absence of spin and can be written as

$$i\hbar\dot{\psi}(x,t) = mc^2\begin{bmatrix}1 & 0\\0 & \text{-1}\end{bmatrix}\psi + c\begin{bmatrix}0 & 1\\1 & 0\end{bmatrix}\left(-i\hbar\frac{\partial}{\partial x} - \frac{e}{c}A(t)\right)\psi + V(x)\psi, \tag{2.70}$$

with the positive and negative energy state components of the 1D relativistic wavefunction $\psi(x,t)$. 1D TDDE has a well-known plane wave solution in the case of a free electron with $V(x) = 0$, and $A(t) = 0$, with the time-dependent parts:

$$\begin{aligned}\hat{\chi}_+ &= \frac{1}{\sqrt{2E(E+mc^2)}}\begin{pmatrix} E+mc^2 \\ cp\end{pmatrix} e^{-i\frac{mc^2}{\hbar}t\sqrt{1+\frac{p^2}{m^2c^2}}} \\ \hat{\chi}_- &= \frac{1}{\sqrt{2E(E+mc^2)}}\begin{pmatrix} -cp \\ E+mc^2\end{pmatrix} e^{i\frac{mc^2}{\hbar}t\sqrt{1+\frac{p^2}{m^2c^2}}}.\end{aligned} \tag{2.71}$$

As we may notice, $\hat{\chi}_+$ and $\hat{\chi}_-$ are orthogonal, which makes their time-independent parts a good basis for the general solution of Eq. (2.70). Hence, a general solution $\hat{\psi}(x,t)$ of the 1D TDDE can be presented as

$$\hat{\psi}(p,t) = \hat{f}_e(p,t)\frac{1}{\sqrt{2E(E+mc^2)}}\begin{pmatrix} E+mc^2 \\ cp\end{pmatrix} + \hat{f}_p(p,t)\frac{1}{\sqrt{2E(E+mc^2)}}\begin{pmatrix} -cp \\ E+mc^2\end{pmatrix} \tag{2.72}$$

where scalar functions $\hat{f}_e(p,t)$ and $\hat{f}_p(p,t)$ describe electron's and positron's components of the total wave function $\hat{\psi}(p,t)$. Since $\hat{\chi}_+$ and $\hat{\chi}_-$ are orthogonal, the squared module of the wavefunction

$$|\hat{\psi}(p,t)|^2 = |\hat{f}_e(p,t)|^2 + |\hat{f}_p(p,t)|^2 \tag{2.73}$$

As in the case of 1D TDSE, it makes sense to present a numerical minimal reproducible example of the solution of Eq. (2.70). We start with the initial condition $\psi(x,0)$. If we consider light atoms, such as H or He, then we may use the same procedure, as described in Sec. 2.2.3, because relativistic effects in case of the small nuclear charge $Z \ll 137$ do not manifest themselves for the ground state. Let us call such a ground state $\psi_g(x)$. We assume that at the initial moment $t = 0$ there are now positrons in our system, so an initial wave function is

$$\hat{\psi}(p,0) = \begin{pmatrix} \hat{\psi}_1(p) \\ \hat{\psi}_2(p) \end{pmatrix} = \hat{\psi}_g(p) \frac{1}{\sqrt{2E(E+mc^2)}} \begin{pmatrix} E+mc^2 \\ cp \end{pmatrix} \tag{2.74}$$

with $E = mc^2\sqrt{1+\frac{p^2}{m^2c^2}}$. It is easy to see, that in the non relativistic limit $p \ll mc$ the second component is small comparing to the first one. Now, having both $\hat{\psi}_1(p)$ and $\hat{\psi}_2(p)$ at hand, we are ready to start the time evolution.

Let us first regroup terms from the Hamiltonian in Eq. (2.70) into an interaction part H_i and a free-particle H_0 parts

$$H_i = -c \begin{bmatrix} 0 & 1 \\ 1 & 0 \end{bmatrix} \frac{e}{c} A(t) + V(x) \tag{2.75}$$

$$H_0 = mc^2 \begin{bmatrix} 1 & 0 \\ 0 & -1 \end{bmatrix} - ic \begin{bmatrix} 0 & 1 \\ 1 & 0 \end{bmatrix} \hbar \frac{\partial}{\partial x} \tag{2.76}$$

At the first glance, H_0 looks simple. The term βmc^2 just rotates the phases of the respective wavefunctions by $\pm mc^2$, while the term $\sigma_x p_x c$ contains just a first derivative with the respect to x. However, unlike to the TDSE case, now we need to take into account, that β and σ_x are matrices and, moreover, $[\beta, \sigma_x] = 2\sigma_x$. Therefore, we are not going to split H_0 further, but work with it as with a single entity. Since H_0 is Hermitian, it can be diagonalized by the matrix of its eigenvectors. Such vectors have been already written in Eq. (2.71). Hence, diagonalization matrix Q is

$$Q = \frac{1}{\sqrt{2E(E+mc^2)}} \begin{bmatrix} E+mc^2 & -cp \\ cp & E+mc^2 \end{bmatrix} \tag{2.77}$$

and

$$Q^T H_0 Q = E\beta. \tag{2.78}$$

Recalling the property Eq.(2.22), we can now write down the evolution operator as

$$e^{-i\Delta t H_0} = Q^T e^{-i\Delta t \beta E/\hbar} Q \tag{2.79}$$

where $e^{-i\Delta t\beta E/\hbar}$ is a simple diagonal matrix.

Handling H_i is also non trivial due to the presence of σ_x. Although parts with $-\sigma_x eA(t)$ and $V(x)$ commute and H_i can be further split into $H_i = H_A + H_V$, the part H_A requires some more attention. In fact, if we expand an evolution operator $e^{-i\Delta t H_A}$ into a series by definition

$$e^{-i\Delta t H_A} = \sum_{k=0}^{\infty} (ieA(t)\Delta t)^k \sigma_x^k \tag{2.80}$$

and use the property

$$\sigma_x^{2k} = 1, \quad \sigma_x^{2k+1} = \sigma_x \;\text{ for }\; k > 0 \tag{2.81}$$

then it turns out, that

$$e^{-i\Delta t H_A} = \begin{bmatrix} \cos(e|A(t)|\Delta t) & -i\sin(e|A(t)|\Delta t) \\ -i\sin(e|A(t)|\Delta t) & \cos(e|A(t)|\Delta t) \end{bmatrix}. \tag{2.82}$$

The general formula for the 3D case can be found in [25]. So, having Eq. (2.79) and Eq. (2.82) at hand, we are ready to write down a one propagation step for the full Hamiltonian Eq. (2.70) using the split operator approach

$$e^{-i\Delta t H\hbar} = e^{-i\frac{\Delta t}{2\hbar}V} e^{-i\frac{\Delta t}{2\hbar}H_A}\; Q^T\; e^{-i\Delta t\beta E/\hbar} Q\; e^{-i\frac{\Delta t}{2\hbar}H_A} e^{-i\frac{\Delta t}{2\hbar}V}. \tag{2.83}$$

It is, of course, absolutely necessary to estimate an error of the Eq. (2.83) and find suitable spacial Δx and time Δt step sizes. Regarding Δx, an error analysis is the same as for the TDSE. Again, we have $\Delta x \leq \pi/p_{\max}$. In the relativistic case, it is reasonable to consider $p_{\max} \sim mc$. Although Δx turns out to be small for the relativistic problem, it is not drastically different from the TDSE case.

For the Δt, the situation is different. In many works [25, 36, 37], an estimation $\Delta t \leq \hbar/(mc^2)$ is usually postulated. Actually, this estimation has both mathematical and physical ground. From the mathematical point of view, we can turn to the error term Eq. (2.26). Since matrices σ_x and β do not commute, we have

$$[H_0, [H_0, H_i]] \sim mc^3 p \tag{2.84}$$

Then, estimating $p \sim mc$, we have for the global error $\mathcal{O}(m^2c^4\Delta t^2)$. As we may say, a condition on the time step $\Delta t \leq \hbar/(mc^2)$ is much more severe, than for TDSE. This makes the numerical solution of the TDDE so demanding. Spectacularly, that the condition on the Δt hold even if there is no external field $A(t)$. As an example, one may introduce a Klein tunneling. In a simulation of this experiment, a wavepacket comes from the left to the step-like potential of the large amplitude $eV \approx mc^2$. In this case, relativistic effects become important and the packet can tunnel through the potential. From the point of view of physics, an interaction between the states with negative and positive energies complicates the procedure. In the relativistic case, such interaction unfolds even if there were no positrons initially, via the virtual states.

2.3.2 Foldy-Wouthuysen transformation

Over the years, numerous efforts of the community have been directed towards the reducing the computational complexity of TDDE. One of the approaches was focused on finding the alternatives to the direct solving of TDDE. Among them are approaches, employing the Klein-Gordon (KGE) [22] or square root Klein-Gordon equation (SKGE) [49]. In this regard, a method, based on the Foldy-Wouthuysen (FW) transformation [68], would be of the interest. Indeed, FW transformation naturally removes an interaction between the positive and negative energy solutions, which would allow to use larger time step size Δt. Besides, FW Hamiltonian has a block-diagonal structure, so it correctly describes spin interactions. However, an exact form of the FW transformation in case of the applied external time-dependent field is unknown. Although, there have been developed different methods on the obtaining of approximate FW Hamiltonians. Until recent times, only approximation for the weak field have been known [59]. That changed with Silenko's approach, who managed to derive and approximate FW Hamiltonian for the arbitrary strong external time-dependent fields within a quasi-classical approximation [59–61, 69]. To be precise, in Silenko's form, all the terms of the zeroth and first order in $\hbar$ are exact, while some of the $\hbar^2$ terms are also presented.

Let us present the main formulae, leading to the FW transformation in Silenko's form. To begin with, we can write Dirac's Hamiltonian as

$$H_D = \beta mc^2 + O + V \tag{2.85}$$

where operators

$$\begin{gathered} O = c\alpha\left(\mathbf{p} - \frac{e}{c}\mathbf{A}(\mathbf{r},t)\right), \quad V = V(\mathbf{r}) \\ \beta V = V\beta, \quad \beta O = -O\beta. \end{gathered} \tag{2.86}$$

The key idea is to introduce a unitary operator such that

$$\psi_{FW} = U_{FW}\psi = e^{iS_{FW}}\psi. \tag{2.87}$$

Eriksen [70] proposed a condition, eliminating the ambiguity in the definition of U_{FW}

$$\beta S_{FW} = -S_{FW}\beta \iff \beta U_{FW} = U_{FW}^{\dagger}\beta. \tag{2.88}$$

With such an operator U_{FW}, FW Hamiltonian becomes

$$H_{FW} = U\Big(H_D - i\hbar\partial_t\Big)U^{-1} + i\hbar\partial_t. \tag{2.89}$$

Although Erikson [70] found an operator U_{FW}, which satisfies the condition Eq. (2.88), its form in general case of the time-dependent external field is very complicated. Therefore, the Hamiltonian Eq. (2.89) was found only as a v/c expansion, which limits its applications only to the weak field cases. Not a long time ago, Silenko proposed [69] the following operator U_{FW}

$$U = \frac{\beta\epsilon + \beta mc^2 - O}{\sqrt{(\beta\epsilon + \beta mc^2 - O)^2}}\beta \tag{2.90}$$

$$U^{-1} = \beta\frac{\beta\epsilon + \beta mc^2 - O}{\sqrt{(\beta\epsilon + \beta mc^2 - O)^2}}, \tag{2.91}$$

which yields another type of the FW Hamiltonian and where

$$\epsilon = mc^2\sqrt{1 + \frac{O^2}{m^2c^4}}. \tag{2.92}$$

Hence, in a case of electron, exposed to the external field, the operator U_{FW} becomes

$$U = \frac{\beta\epsilon + \beta mc^2 - O}{\sqrt{2\epsilon(\epsilon + mc^2)}}\beta \tag{2.93}$$

For the 1D case, the further simplification yields

$$U = \frac{1}{\sqrt{2\epsilon(\epsilon + mc^2)}}\begin{bmatrix} \epsilon + mc^2 & (p - \frac{e}{c}A)c \\ -(p - \frac{e}{c}A)c & \epsilon + mc^2 \end{bmatrix} \tag{2.94}$$

$$U^{-1} = \frac{1}{\sqrt{2\epsilon(\epsilon + mc^2)}}\begin{bmatrix} \epsilon + mc^2 & -(p - \frac{e}{c}A)c \\ (p - \frac{e}{c}A)c & \epsilon + mc^2 \end{bmatrix} \tag{2.95}$$

Applying an operator Eq. (2.93) in Eq. (2.89), we receive an approximate FW Hamiltonian

$$H_{FW} = \beta\epsilon + V - \frac{1}{8}\left\{\frac{1}{\epsilon(\epsilon + mc^2)}, [O, [O, \mathcal{F}]]\right\} + \mathcal{O}(\lambda^2) \tag{2.96}$$

where $\lambda = \hbar/(mc)$ and

$$\mathcal{F} = V - i\hbar\partial_t, \quad O = c\sum_{n=1}^{3}\alpha_n\left(p_n - \frac{e}{c}A_n(\boldsymbol{r}, t)\right), \quad \epsilon = mc^2\sqrt{1 + \frac{O^2}{m^2c^4}}. \tag{2.97}$$

The Hamiltonian Eq. (2.96) is not exact. Actually, terms proportional to zeroth and first order of $\hbar$ are exact and satisfy Erikson condition. However, not all the operators of the $\hbar^2$ terms are presented. Appendix A is focused on the analysis of the omitted term and show, that such an approximate Hamiltonian is sufficient for the ionization regimes, discussed in this thesis. An operator O can be further expanded in ϵ

$$\epsilon = mc^2\sqrt{1+\frac{\left(\boldsymbol{p}-\frac{e}{c}A(\boldsymbol{x},t)\right)^2}{m^2c^2}-\frac{e\hbar}{m^2c^3}\boldsymbol{\Sigma}\cdot\boldsymbol{B}}, \tag{2.98}$$

where Σ_i are 4×4 matrices are defined as follows

$$\Sigma_i = \begin{pmatrix}\sigma_i & 0\\ 0 & \sigma_i\end{pmatrix}. \tag{2.99}$$

Also, the term with anti-commutator can be expanded in a more familiar way

$$\frac{1}{8}\left\{\frac{1}{\epsilon(\epsilon+mc^2)},[O,[O,\mathcal{F}]]\right\} = -\frac{e\hbar}{8}\left\{\frac{1}{\epsilon(\epsilon+mc^2)},[\Sigma\cdot(\mathbf{p}\times\mathbf{E}-\mathbf{E}\times\mathbf{p})-\hbar\Delta V]\right\}, \tag{2.100}$$

which is useful for the comparison of Eq. (2.96) with Pauli equation [71] or for the analysis of the order of the approximation Appendix A.

In fact, with the Hamiltonian Eq. (2.96) an equation Eq. (2.27) splits into the two independent parts, which dramatically simplifies the solution. As we may see, the resulting 4×4 matrices in Eq. (2.96) are β, $\beta\Sigma_i$ and $\alpha_i\alpha_j$. All of them are block-diagonal and do not mix up solutions for the positive and negative energies. So, one of the parts of Eq. (2.96) governs an evolution of electrons both with spin up and spin down, and the other one of positrons. Indeed, now there are no explicit transitions between the positive and negative energy states. In FW representation, the virtual states are covered implicitly via the transformation U_{FW}, because an original Dirac wavefunction $\psi = U_{FW}^{-1}\psi_{FW}$ can always be restored from the FW wavefunction. Let us show, how to calculate any original Dirac observable, using the FW function ψ_{FW}. In 1D, we first transform ψ_{FW} to ψ by means of Eq. (2.94)

$$\hat{\psi}(p,t) = \begin{pmatrix}\hat{\psi}_1\\ \hat{\psi}_2\end{pmatrix} = U(p,t)\begin{pmatrix}\hat{\psi}_{FW}^{+}\\ \hat{\psi}_{FW}^{-}\end{pmatrix} \tag{2.101}$$

Now, having ψ as a spinor $(\psi_1,\psi_2)^T$, we can present it in form of Eq. (2.72)

$$\begin{pmatrix}\hat{f}_e(p,t)\\ \hat{f}_p(p,t)\end{pmatrix} = Q\begin{pmatrix}\hat{\psi}_1(p,t)\\ \hat{\psi}_2(p,t)\end{pmatrix} \tag{2.102}$$

where matrix Q is defined in Eq. (2.77). Thus, any observable can be written by definition as

$$\langle W\rangle(t) = \int_{-\infty}^{\infty}\hat{W}(p,t)\left(|f_e(p,t)|^2+|f_p(p,t)|^2\right)dp. \tag{2.103}$$

Hence, we obtain an alternative Eq. (2.96) to govern relativistic ionization and calculate corresponding observables. Of course, the Hamiltonian Eq. (2.96) is not exact. However, as an analysis in Appendix A shows, it can be reliably utilized for the systems, considered in this thesis. Moreover, previous studies [46, 72] show, that if the ground state consists of only electrons, then spin effects are negligible even for relativistically strong $\mathbf{A}(t)$.

Regarding the evolution of the ψ_{FW} function, we must distinguish dipole $\mathbf{A}(t)$ and non dipole $\mathbf{A}(\mathbf{r},t)$ regimes. In the dipole case, an evolution operator with the H_{FW} can be constructed in the usual manner. Just as with TDSE or TDDE, we split the operator into the kinetic H_k and potential V parts

$$H_k = \beta\epsilon - \frac{1}{8}\left\{\frac{1}{\epsilon(\epsilon+mc^2)}, [O,[O,\mathcal{F}]]\right\}, \tag{2.104}$$

and rewrite the Eq. (2.25) as

$$e^{-i\Delta t H_{FW}/\hbar} = e^{-i\frac{\Delta t}{2\hbar}V(x)}\ F^{-1}\ e^{-i\Delta t H_k/\hbar}\ F\ e^{-i\frac{\Delta t}{2\hbar}V(x)} \tag{2.105}$$

where F denote respective Fourier transformation. However, in the non dipole case, the situation becomes much less trivial. Indeed, the square root term ϵ, as well as the other terms, containing ϵ, are pseudo spectral operators and lack a space, in which they have a diagonal matrix representation. In order to overcome this problem, a few approaches were suggested [49, 73]. It is also worth noting, that such an obstacle was observed not only in quantum physics, but for instance, in oceanology [74] . Therefore, while working with nondipole case, we must rely on one or another workaround. One of such ways, closely related to the scaling coordinates approach, is developed in Chapter 3.

In practice, the solution of the FW equation is less computationally demanding, than TDDE. Indeed, as was mentioned previously, the main complexity of TDDE stems from the transitions between positive and negative energy states. Or, in other words, due to the presence of the terms with matrices α_i in the Hamiltonian Eq. (2.85). FW Hamiltonian Eq. (2.96) completely resolves this problem by the decoupling of the negative and positive energy states. Hence, the condition on Δt is weaker, than for TDDE. Analyzing the commutator in the error term Eq. (2.26) we come to the conclusion, that $\Delta t \ll m a_B/p_{\max}$. The condition on Δx remains the same and $\Delta x \leq \hbar\pi/p_{\max}$.

Chapter 3

The Development of the Relativistic Scaling Coordinates Method

3.1 The relativistic scaling method

3.1.1 Time-dependent coordinate scaling

In this chapter, the scaling method for the relativistic strong field ionization problem generalizing the nonrelativistic method for TDSE [56] is developed. The scaling method is designed to overcome two key hurdles: (1) A long grid size is required to accommodate the full ionized wavepacket, especially at high laser intensities; (2) The growing electron momenta in the ionized electron wavepacket demand a small grid step size for a good precision. The third hurdle specific for the relativistic case to be addressed is: (3) During the propagation of the wavefunction, there are virtual transitions between the positive and negative energy states, even in the regime when the real pair production is suppressed.

The coordinates scaling $x = R(t)\xi$ in the relativistic case is in the following applied identically to the nonrelativistic one presented in Sec. 2.2.4. Namely, Eqs. (2.51) and (2.52) are used. As a result, the hurdle (1) is tackled by the expansion $R(t)$ of the physical space x with time.

Let us develop the prototype of the relativistic scaling method on the example of a 1D problem. In the relativistic case our starting point is a 1D TDDE Eq. (2.70) with the positive and negative energy state components of the 1D relativistic wavefunction

$\vec{\psi}$, the atomic potential $V(x)$, the laser vector potential $A(t)$, and the electron charge e. As was mentioned in Sec. 2.3.1, 1D TDDE has a well-known plane wave solution Eq. (2.71) in the case of a free electron with $V(x) = 0$, and $A(t) = 0$.

Consequently, we expect to absorb the relativistic kinetic phase of the wavefunction employing the ansatz of Eq. (2.54) with

$$\hat{f}_{\pm}(p,t) \xrightarrow[t\to\infty]{} e^{\mp i\frac{mc^2}{\hbar}t\sqrt{1+\frac{p^2}{m^2c^2}}}, \tag{3.1}$$

where the corresponding coordinate dependent wavefunction $f_{\pm}(x,t)$ is derived from $\hat{f}_{\pm}(p,t)$ via inverse FT. Unfortunately, there is no exact analytical form of the inverse FT for the right-hand part of Eq. (3.1), and we will carry out approximate FT using SPA:

$$f_{\pm}(x) = \frac{1}{2\pi\hbar}\int_{-\infty}^{\infty} e^{\mp i\frac{mc^2}{\hbar}t\sqrt{1+\frac{p^2}{m^2c^2}}} e^{+i\frac{px}{\hbar}}\,dp. \tag{3.2}$$

The saddle-point in relativistic case is $p_0 = \pm\frac{mx}{\sqrt{t^2-x^2/c^2}}$ and, employing SPA, we obtain

$$f_{\pm}(x) \propto e^{\mp i\frac{mc^2}{\hbar}\sqrt{t^2-\frac{x^2}{c^2}}}, \quad t\to\infty. \tag{3.3}$$

The latter in the computational coordinate reads

$$f_{\pm}(R\xi) \propto e^{\mp i\frac{mc^2}{\hbar}\sqrt{t^2-\frac{R^2}{c^2}\xi^2}}, t\to\infty. \tag{3.4}$$

The highly oscillating functions $f_{\pm}$, in contrast to the nonrelativistic one of Eq. (2.59), have restricted validity region inside the light cone $x < ct$. Moreover, oscillations of $f_{\pm}$ become infinite at $x \to ct$. To have a consistent $f_{\pm}$ in the full simulation box $x \in [-L, L]$ and throughout the entire simulation time $t \in [0, t_F]$, we modify Eq. (3.4). One of the ways to do that is to make an analogy to Eq. (2.59)

$$f_{\pm}(R\xi) \sim e^{\mp i\frac{mc^2}{\hbar}t\sqrt{1-\frac{\dot{R}^2}{c^2}\xi^2}}, \tag{3.5}$$

where the singularity is not reached because the characteristic scaling velocity v is smaller than speed of light c. Yet, it is more practical to introduce an additional factor $\beta(t)$, which hinders approaching the singularity. It does not only relax the singularity, but also incorporates an information about the initial wavefunction, making (3.6) a better approximation for intermediate times of the interaction:

$$f_{\pm}(R\xi) \sim e^{\mp i\frac{mc^2}{\hbar}\sqrt{t^2-\frac{R^2}{c^2}\beta^2\xi^2}}, \qquad \beta(t) = \frac{ut}{\sqrt{1+u^2t^2}},\ u = 2\hbar w^2. \tag{3.6}$$

The parameter w can be chosen so that it reflects an information about the initial wavefunction $\psi(x_0, 0)$, particularly, the width of $\psi(x_0, 0)$. To do that, we choose parameter w such that $\psi(x_0, 0) = e^{-w^2 x_0^2} = 1/2$. The condition on the light cone then becomes

$$\frac{x}{c}\frac{u}{\sqrt{1+u^2t^2}} < 1. \tag{3.7}$$

The formula Eq. (3.6) does not include the effect of the vector potential $A(t)$. The effect of the vector potential is incorporated by the following procedure:

Algorithm 1 The procedure of the phase φ calculation at each time step Δt

```
Take the exact phase in momentum space $\hat{\varphi} = \mp \int_0^t \sqrt{1 + \frac{[p - \frac{e}{c}A(t')]^2}{c^2}} dt'$
Calculate a critical point $x_0(p) = -\frac{d\hat{\varphi}}{dp}$
Calculate the phase as $\varphi(x)|_{x=x_0(p)} = \hat{\varphi}(p) + p x_0(p)$
Rescale $x' = \beta(t)x$ and obtain values $\varphi(x')$ via interpolation.
```

In principle, this procedure implements inverse FT of the fast oscillating function $\hat{f}_\pm(p,t)$ via SPA at each Δt and then introduces factor $\beta(t)$ in Eq. (3.6). Hence, the conditions for the application of procedure 2 are the same as for regular SPA via Eq. (3.2).

The property of the scaling method of Eq. (2.60), allowing one to obtain the photoelectron asymptotic momentum distribution via far-field coordinate wavefunction, is still applicable in the relativistic case. An expression for ξ in this case also includes a relativistic factor

$$\xi \xrightarrow[R\to vt]{} \frac{p}{mv}\frac{1}{\sqrt{1+\frac{p^2}{m^2c^2}}}. \tag{3.8}$$

Although the formulae for the fast oscillating part of the wavefunction in the nonrelativistic Eq. (2.59) and relativistic Eq. (3.6) cases look similar, the further procedure of the phase cancellation is very different and demands an introduction of a special transformation which we discuss next.

3.1.2 Foldy-Wouthuysen transformation

In the nonrelativistic case, the transformation of Eq. (2.59) eliminates the fast oscillating phase of the TDSE solution. In the relativistic case, the similar transformations of $f_\pm$ via Eq. (3.6) do not remove high-oscillating components in the wavefunction completely. This is because the coupling between the positive and negative components of the wavefunction with phases of opposite sign induces highly oscillating terms in the wavefunction. Therefore, it makes sense to employ FW transformation to derive two decoupled equations of evolution in a form

$$i\hbar\dot{\hat{\psi}}_\pm(p,t) = H_{FW\pm}\hat{\psi}_\pm. \tag{3.9}$$

The FW transformation in Silenko's form is explicitly calculated using a quasiclassical $\hbar$ expansion. It will allow us to obtain relativistic Hamiltonian up to $\hbar^2$-order. In principle, this renders possible to take spin and spin-orbit effects into account for 2D case, if needed. For the 1D case, FW Hamiltonian in Silenko's form Eq. (2.96) reads

$$\begin{gathered}H_{FW\pm} = \pm\varepsilon + V(x) + H_{DW} + O\left(\lambda^2\right)\\ \varepsilon = mc^2\sqrt{1+\frac{(p-\frac{e}{c}A(t))^2}{m^2c^2}},\, H_{DW} = \frac{\hbar^2}{8m}\left\{\frac{mc^2}{\varepsilon(\varepsilon+mc^2)}, V''(x)\right\}.\end{gathered} \tag{3.10}$$

where $\lambda \equiv \hbar/mc$ is the electron Compton wavelength. Here we have no terms, proportional to λ, because spin is naturally absent in the 1D case. The Darwin term H_{DW} has the order λ^2, while the other terms $\sim \lambda^2$ are omitted because of additional smallness, see Appendix A.1. Note that in 2D case spin-orbit coupling terms will appear at λ^2-order. From the computational point of view, solving Eq. (3.10) does not require a very small time step $\Delta t \sim \lambda/c$. Such a relief is possible due to the absence of terms, mixing positive and negative energies as in Eq. (2.62).

Regarding an application of scaling coordinates method, the main difficulty now is an action of the square-route operator ϵ from Eq. (3.10) on a function ψ. FT of the operator ϵ reads

$$F^{-1}\left[\epsilon\right] = -mc^2\frac{1}{\pi}\frac{K_1(|x|/\lambda)}{|x|}e^{+i\frac{x}{\hbar}\frac{e}{c}\frac{A(t)}{mc}}, \tag{3.11}$$

where K_1 denotes the modified Bessel function of the second kind. In coordinate space we have

$$F^{-1}\left[\epsilon\hat{\psi}\right] = -mc^2\frac{1}{\pi}\int_{-\infty}^{\infty}\frac{K_1(|x-x_0|/\lambda)}{|x-x_0|}e^{+i\frac{x-x_0}{\hbar}\frac{e}{c}\frac{A(t)}{mc}}\phi(x_0,t)f(x_0,t)dx_0 \tag{3.12}$$

in which we applied the ansatz of Eq. (2.54). This convolution-type integral has two distinctive features:

(1) the modified Bessel function of the second kind $K_1(|x|)$ has a discontinuity at point $x = 0$, $K(|x|) \xrightarrow[x\to 0]{} \infty$. Moreover, the integral $\int_{-\infty}^{\infty}\frac{K_1(|x|)}{|x|}dx$ does not converge, which complicates an analysis of Eq. (3.12), in particular, one cannot straightforwardly apply a stationary phase approximation.

(2) Although the Bessel function $K_1(|x|)$ is non-zero for all $x \in \mathbb{R}$, it decays exponentially fast via $K(|x|/\lambda) \xrightarrow[x/\lambda\to\infty]{} e^{-|x|/\lambda}$.

Thus, the core function $\frac{K_1(|x-x_0|/\lambda)}{|x-x_0|}$ has a compact support of size λ. Using two considerations above, we expand function $\phi(x_0, t)$ in Eq. (3.12) at point $x = x_0$ into a Taylor series

$$F^{-1}\left[\varepsilon\hat{\psi}\right] \approx mc^2\left[\phi T_0(x,t) - i\lambda\phi' T_1(x,t) - \frac{\lambda^2}{2}\phi'' T_2(x,t) + O\left(\lambda^3/\lambda_e^3\right)\right] \tag{3.13}$$

in which

$$\begin{gathered} T_0 = F^{-1}\left[\sqrt{1+\frac{(p-\frac{e}{c}A)^2}{m^2c^2}}\hat{f}\right],\ T_1 = F^{-1}\left[\frac{p-\frac{e}{c}A}{mc}\frac{1}{\sqrt{1+\frac{(p-\frac{e}{c}A)^2}{m^2c^2}}}\hat{f}\right], \\ T_2 = F^{-1}\left[\left(1+\frac{(p-\frac{e}{c}A)^2}{m^2c^2}\right)^{-\frac{3}{2}}\hat{f}\right], \end{gathered} \tag{3.14}$$

and $\phi' \sim 1/\lambda_e$ Next, we take a closer look at $\hat{f}$ in Eq. (3.14). Since it is presumed to be a high-oscillating component of the wave function, we represent it as $f(x,t) = e^{i\varphi(x,t)}$ with phase φ corresponding to Eq. (3.6) in the case of $A(t) = 0$, or to the procedure of Algorithm 1, if $A(t) \neq 0$. Since the phase $\varphi(x)$ is presumed to be smooth on the scale of λ, we expand φ into a Taylor series at point $x = x_0$

$$f(x_0,t) = e^{i\varphi(x_0,t)} \approx e^{i\varphi(x,t) - i\varphi'(x,t)(x-x_0)}\left[1 + \frac{i}{2}\varphi''(x,t)(x-x_0)^2 + O\left(\frac{\lambda^2}{\lambda_l^2}\right)\right], \tag{3.15}$$

where λ_l is the laser wavelength and the omitted terms are estimated using Eq. (3.6) as

$$\varphi^{(n)}(x-x_0)^n \sim \varphi^{(n)}\lambda^n = \left(\frac{\lambda}{c}\frac{1}{t}\right)^{n-1} \cdot \tilde{\varphi}(x,t)^{(n)},\ n \geqslant 2 \tag{3.16}$$

with $\tilde{\varphi}$ being a dimensionless time-dependent function. The series (3.15) is valid within the following simulation box

$$x = R(t)\xi < \frac{ct}{\beta}\sqrt{1-\left(\frac{\beta^2}{2\tilde{t}}\right)^{2/3}}, \tag{3.17}$$

with the dimensionless time $\tilde{t} = t\omega_l/(2\pi)$.

For instance, in the case of $w \approx 0.5$ a.u., which corresponds to the ground state of hydrogen, $\omega_l = 1$ a.u., and the initial box size $L = 10/w,\ x \in [-L, L]$, two of the many options to choose scaling parameters are

$$R(t) = \sqrt[4]{L^4 + v^4(t-t_0)^4},\quad t_0 \approx 0.7,\quad v \lesssim 0.985c \quad \text{or} \quad t_0 = 0,\quad v \lesssim 0.95c. \tag{3.18}$$

Such a choice of parameters would guarantee, that the box x obeyed the condition (3.17) throughout the entire simulation and allowed to track wave packages with group velocities smaller than v.

Substituting Eq. (3.15) into (3.14), we obtain

$$T_0(x,t) \approx e^{i\varphi}\sqrt{1+\lambda^2\Big(\varphi'-\frac{e}{c\hbar}A\Big)^2}\left[1-\frac{i}{2}\lambda^2\varphi''\left[1+\lambda^2\Big(\varphi'-\frac{e}{c\hbar}A\Big)^2\right]^{-2}\right]+O\left(\frac{\lambda^2}{\lambda_l^2}\right) \tag{3.19}$$

One can write similar formulae for $T_1(x,t)$ and $T_2(x,t)$ (Appendix A.2). As a result, we obtain an expression for $F^{-1}\left[\varepsilon\hat{\psi}\right]$, involving the wavefunction $\phi(x,t)$ and the phase $\varphi(x,t)$. In this way the equation for the wavefunction $\phi(x,t)$ is obtained

$$i\hbar\partial_t\phi = mc^2\left[\bar{T}_0(x,t)-i\lambda\bar{T}_1(x,t)\partial_x-\frac{\lambda^2}{2}\bar{T}_2(x,t)\partial^2_{xx}\right]\phi+V(x)\phi+\hbar\dot{\varphi}\phi+O\left(\lambda^2/a_B^2\right), \tag{3.20}$$

where $\bar{T}_k = e^{-i\varphi}T_k,\ k=0,1,2,\ldots$. In scaled coordinates $\xi = x/R(t)$ Eq.(3.20) reads

$$\begin{aligned} i\hbar\partial_t\phi =& mc^2\left[\bar{T}_0(\xi R,t)-i\lambda\bar{T}_1(\xi R,t)\frac{1}{R}\partial_\xi-\frac{\lambda^2}{2}\bar{T}_2(\xi R,t)\frac{1}{R^2}\partial^2_{\xi\xi}\right]\phi+V(\xi R)\phi\\ &+\hbar\phi\left[\dot{\varphi}-\frac{\dot{R}}{R}\xi\partial_\xi\varphi\right]+i\hbar\frac{\dot{R}}{R}\xi\partial_\xi\phi+O\left(\lambda^2/a_B^2\right). \end{aligned} \tag{3.21}$$

In estimating the error in Eqs. (3.20) and (3.21), we assumed that the function ϕ is low-oscillating. As we show in the next section, this could be violated for the scattered parts of ψ, which will increase the error for the weak tails of the wave function. The full Dirac equation after the scaling procedure is presented in Appendix A.1.

3.1.3 Free wave packet propagation

Let us illustrate the relativistic scaling method on a simple example of the propagation of a Gaussian wave packet. In Fig. 3.1, the simulation of the motion with a group velocity $v_g = 0.2c = 27.4$ a.u. without applying the scaling method is depicted. A simulation box with a length $L = 400$ a.u. is used, and snapshots of the wave packet from $T = 0$ to $T = 5$ a.u. are made. To compare, the same motion is shown in Fig. 3.2, but with the scaling being turned on. There, the expansion parameter of the scaling method, Eq. (2.52) of the paper is $v_m = 120$ a.u.

Although we can clearly see, that $v_g < v_m$, nevertheless the wave packet is stuck at a certain point ξ_s. We can estimate the point ξ_s, where the wave packet stops, using the mapping between the physical coordinate x and the computational coordinate ξ:

$$x = R(t,v)\ \xi \approx v_m t\ \xi.$$

As $\xi \in [0,1]$ by definition, the scaling method for the simulation works for the case of $v < v_m$, where v is the typical (maximal) velocity involved in the wave packet, and there is no other condition imposed on the velocity v. With a rough estimate $v \sim v_g$, we arrive at the condition

$$\xi_s \sim v_g/v_m.$$

For the parameters of Fig. 3.2, $\xi_s L = 27.4/120 \approx 91.3$ a.u., which is in accordance with Fig. 3.2. The scaling method works well for any $v_m > |v_g|$, even when $v_g < 0$, as illustrated in Figs. 3.1-3.4.

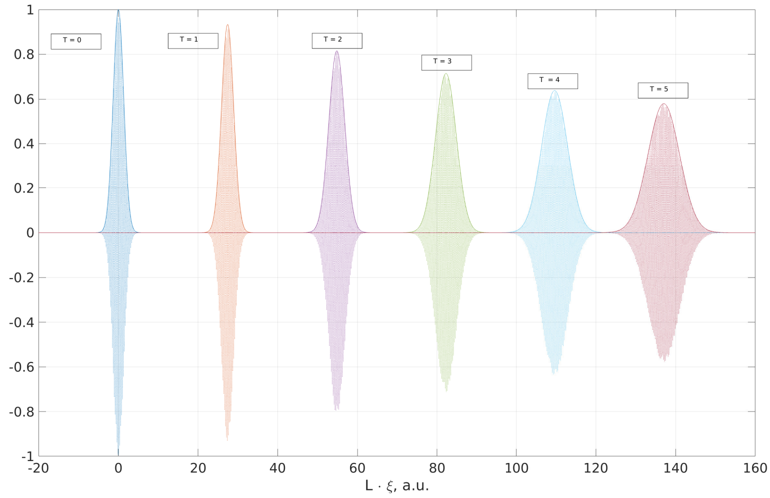

Figure 3.1: The wave packet $e^{-(0.53x)^2+ix0.2c}$ in coordinate space moving to the right, with snapshots at at different times. No scaling is applied.

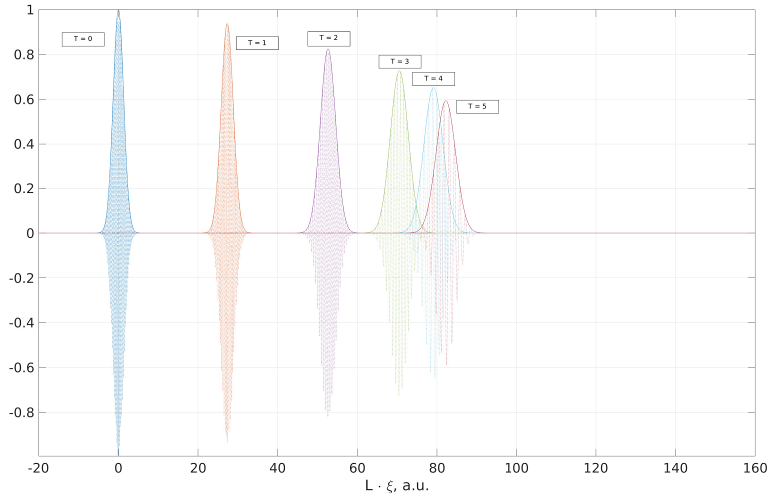

Figure 3.2: The wave packet $e^{-(0.53x)^2+ix0.2c}$ moving to the right. Scaling is ON with the parameter $v_m = 120$ a.u.

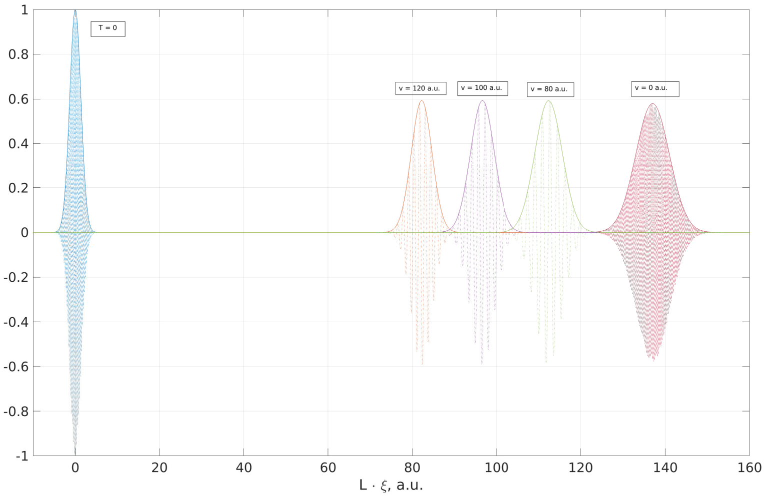

Figure 3.3: The wave packet $e^{-(0.53x)^2+ix0.2c}$ moving to the right with the group velocity $v_g = 0.2c$. Scaling is ON with different parameters $v_m = 120$ a.u., 100 a.u., 80 a.u., 0 a.u.. The snapshot is taken at time $T = 5$ a.u. Depending on v_m, the packet stops at different coordinates $\xi_s L$.

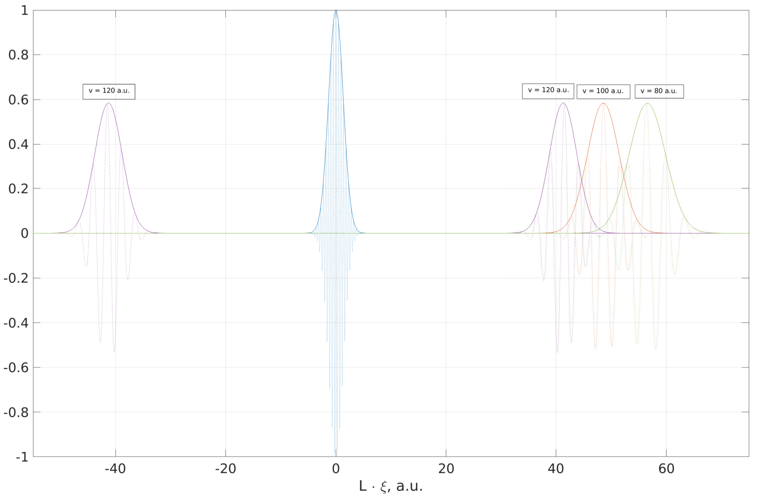

Figure 3.4: The wave packet $e^{-(0.53x)^2+ix0.1c}$ moving to the right and a wave packet $e^{(-(0.53x).^2)-ix0.1c}$ moving to the left, with $v_g = 0.1c$ and $v_g = -0.1c$, respectively. Scaling is ON with different parameters $v_m = 120$ a.u., 100 a.u., 80 a.u.. The snapshot is taken at time $T = 5$ a.u.

We can conclude that the coordinate scaling method is not limited to processes with a single asymptotic characteristic velocity of the electrons. The scaling parameter v_m should be larger than the maximum physical velocity involved in the system and it describes how fast the wave packet becomes localized at a certain coordinate.

3.2 Relativistic ionization in 1D

In order to show the advantage of the proposed method with respect to the direct solution of the Dirac equation, and discuss the possible disadvantages, we perform a few simple 1D simulations. Let us consider the interaction of a 1D atom with a strong laser field described by the 1D Dirac equation

$$i\hbar\partial_t\psi = \{mc\sigma_x[p_x - \frac{e}{c}A(t)] + V(x) + mc^2\sigma_z\}\psi, \tag{3.22}$$

with the Pauli matrices σ_x, σ_z, and the atomic potential $V(x) = \frac{e^{-|x|} - e^{-\epsilon|x|}}{|x|}$ with $\epsilon = 10^{-3}$ (the direct solutions of the Dirac equation for the similar problems are given in Ref. [36, 37]). The atom is exposed to two-cycle laser pulse

$$A(t) = A_0 \sin(\omega t) \sin^2(t/4) \left[\theta(2\pi - t) + \theta(t - 2\pi) \exp\left(-4 \cdot 1.774 \cdot (t/\pi - 2)^2\right)\right], \tag{3.23}$$

which grows as a $\sin^2$ and finally switched off as $\exp(-x^2)$, with θ being Heaviside function.

For numerical solution of the scaled equation Eq. (3.21), the following numerical procedures are used. For the time propagation of Eq. (3.21) a simple split operator approach Eq. (2.25) [62, 75, 76] is used, with $V(\xi R)$ being the potential part and the rest of the Eq. (3.21) being the kinetic part. Note, that calculating the action of kinetic matrix exponential on the wave function is not straightforward. Indeed, on the one hand, in Eq. (3.21) we have terms, proportional to the products $f(\xi) \cdot \partial_\xi$ or $f(\xi) \cdot \partial^2_{\xi\xi}$. On the other hand, we prefer to employ the spectral method to calculate derivatives due to their faster convergence [63, 64, 77]. As a result, there is no explicit analytical expression for the kinetic operator in Fourier space. Therefore, we use Krylov subspace methods to calculate the kinetic matrix exponential. In particular, we employ Krylov subspace propagation [40] based on Arnoldi decomposition [78].

For the spatial discretization, the scaling approach allows us to use a non-uniform mesh. Since we cancel the kinetic phase, the spatial step size $\Delta x = R\Delta\xi$ can be small at large distances x, unlike in TDSE or TDDE simulations. Indeed, in latter cases we do not remove oscillations and do not apply the scaling, thus, we must have a small step size Δx throughout the entire simulation and entire simulation box. However, we still have two conditions on Δx at $x = 0$. First, there must be always at least a few grid nodes at the very core of the potential in order to resolve it throughout the entire simulation. Second, any effects, caused by scattering or rescattering on the potential, also must be resolved. Thus, we also claim $\Delta x = \pi/p_{\max}$. For the large distances it is reasonable to take $\Delta x \sim \pi/(R(t)p_{\max})$, at $t \to \infty$. Taking the considerations above into account, we choose a map function from $x_{\text{non-uni}} = m(x_{\text{uni}})$ to be

$$m(x) = \operatorname{asinh}\left(\frac{x}{\max(x)}\sinh(1.35)\right) \cdot \frac{\max(x)}{1.35} \tag{3.24}$$

Since the map function $m(x)$ is known analytically, we can calculate any derivatives on the uniform grid, and then transfer the results to the non-uniform grid via $m^{-1}(x)$.

As a first test, we calculate an average coordinate $\langle x\rangle$. The result for the peak electric field $F = \omega A_0/c = 100$ a.u. is depicted on Fig. 3.5. Here, we observe that the relativistic wave package achieves smaller group velocities compared to the non-relativistic one, due to the presence of relativistic factor. As a result, the relativistic one remains closer to the core throughout the simulation. The entire trajectory is shown in the inset. As a reference on the main canvas, we use a numerical solution of SKGE. Also, we plot a trajectory, obtained via a direct solution of TDDE as in [25], and a trajectory, obtained via the method discussed. One can see, that the latter two converge as a time step Δt is getting smaller. It is also worth to note, that the scaling method allows us to use a much smaller time step to achieve the same accuracy of the calculation of $\langle x\rangle$. This is because the main obstacle to efficiently solve Dirac equation is the laser-induced transitions between positive and negative energy states. In the method of scaling coordinates, these transitions are implicitly covered by the FW transformation. Note, that we have also calculated the ionization probabilities for different parameters F (Table 3.1). As was expected, an ionization in the 1D relativistic case is suppressed, compared to the nonrelativistic one.

In order to show, how the transition between states with positive and negative energies influences the trajectory, the share of negative energy states $P_{-}(t)$ is plotted in Fig. 3.6. Here the notation from Ref. [37] is employed, where the authors notice, that $P_{-}(t)$ almost does not depend on the potential $V(x)$. Indeed, this fact becomes clear, when one consider the process from the point of view of FW transformation, for which operator U_{FW} does not include a central potential $V(x)$, although being solely responsible for the energy transitions.

We see that the scaling method performs well in calculations of average charac-

	Method	$F = 50$ a.u., $a_0 = 0.18$	$F = 100$ a.u., $a_0 = 0.36$	$F = 200$ a.u., $a_0 = 0.72$
Ionization prob.	TDSE	0.16	0.31	0.47
	Dirac	0.15	0.28	0.39
	Method	0.15	0.28	0.39
$\langle x \rangle$	TDSE	5.36	11.42	21.67
	Dirac	5.36	10.36	15.18
	Method	5.36	10.36	15.17

Table 3.1: Ionization probabilities and an average coordinate of the wave packet $\langle x \rangle$ after the end of the pulse, comparing the TDSE, the TDDE and the scaling method. The laser frequency is $\omega = 2$ a.u., $F = \omega A_0 / c$ is the peak electric field, and $a_0 = \frac{F}{c\omega}$ the relativistic field parameter.

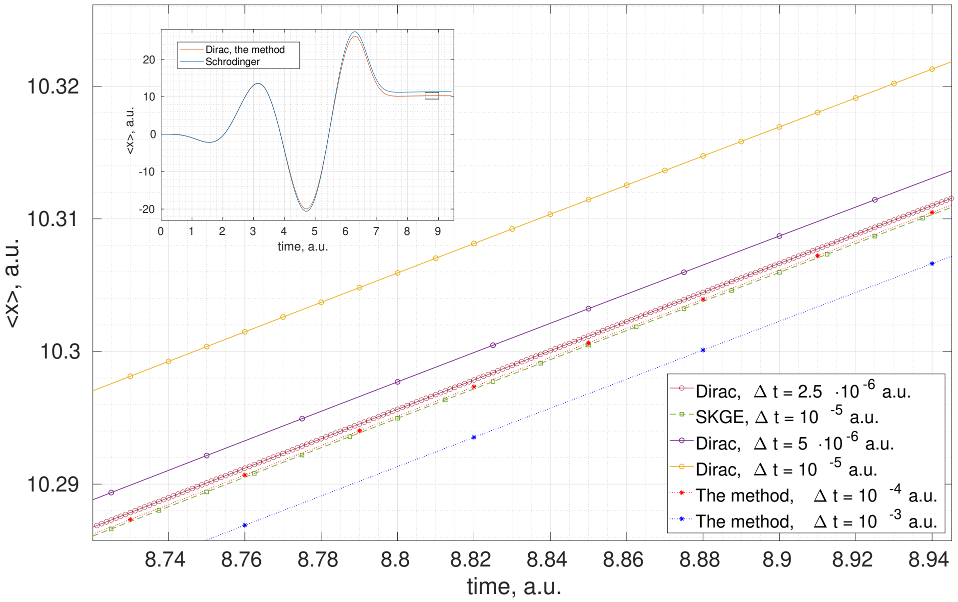

Figure 3.5: Electron trajectory $\langle x \rangle$, calculated via the scaling method (dotted lines with full asterisks), standard TDDE (solid lines with empty cycles), and SKGE (dashed line with empty squares) . The laser field is $F = 100$ a.u. and the frequency $\omega = 2$ a.u. The entire trajectory is shown in the inset. The trajectory, calculated via the scaling method, converges faster and requires a larger time step Δt. The supplementary table A.1 is given in Appendix A.3.

teristics such as $\langle x\rangle$ or $P_-(t)$. Let us further discuss the description of the space-time wave function and the electron spectrum after the interaction. In Fig. 3.7 the wave function in coordinate space after interaction is shown at $t = 9.425$ a.u. One can clearly see an agreement between the wave functions calculated via the direct solution of the Dirac equation [25] and that via the scaling method for the main region of the wave function, centered around the origin. However, one could also see two high-energy peaks, running away from the center, whose Dirac and FW versions do not coincide, although their magnitudes are damped by a factor of 10^{-8}. These parts of the wave function correspond to the scattering on the core which have a phase deviating from the phase φ introduced via Eq.(3.6). As a result, the wave function ϕ in Eq. (3.15) is no longer smooth in those regions, leading to the only semi-relativistic description of the these small peaks.

The question arises why the scaling method accuracy is deteriorated for the scattered part of the wavepacket. The matter is the change of the phase of the wavepacket at scattering, which is discussed in more detail in Appendix A.4. In the scaling method, the phase of the wave function originating from the kinetic propagation is accurately canceled, irrespective of the range of the velocities involved in the wavepacket. The phase cancellation and related inaccuracies arises when the wave packet acquires an additional scattering phase. In this case the kinetic phase cancellation is described only in an approximated manner in our method applying the Taylor-expansion in Eq.(3.19). Consequently, this deficiency limits the scenarios where the method can be applicable. The method will not be efficient for the investigation of recollision effects. However, taking into account that the role of rescattering is suppressed in the relativistic ionization problem [79,80], this difficulty is in fact not a limiting factor for the relativistic strong field ionization problem, where superponderomotive acceleration during above-threshold ionization [11,81], as well as quantum processes including spin effects can happen during the direct ionization step [82].

One of the ways to overcome this problem is to introduce a more advanced method for the calculation of the integral of Eq. (3.12). For instance, rather than expanding into the Taylor series, one could apply the expansion into a short Fourier series, localized near the core of the Bessel function $K_1(|x|)$. Such an approach is similar to the Short-time Fourier Transform and would allow retaining high-frequency components of the function $\phi(x,t)$, making use of the locality of $K_1(|x|)$ at the same time.

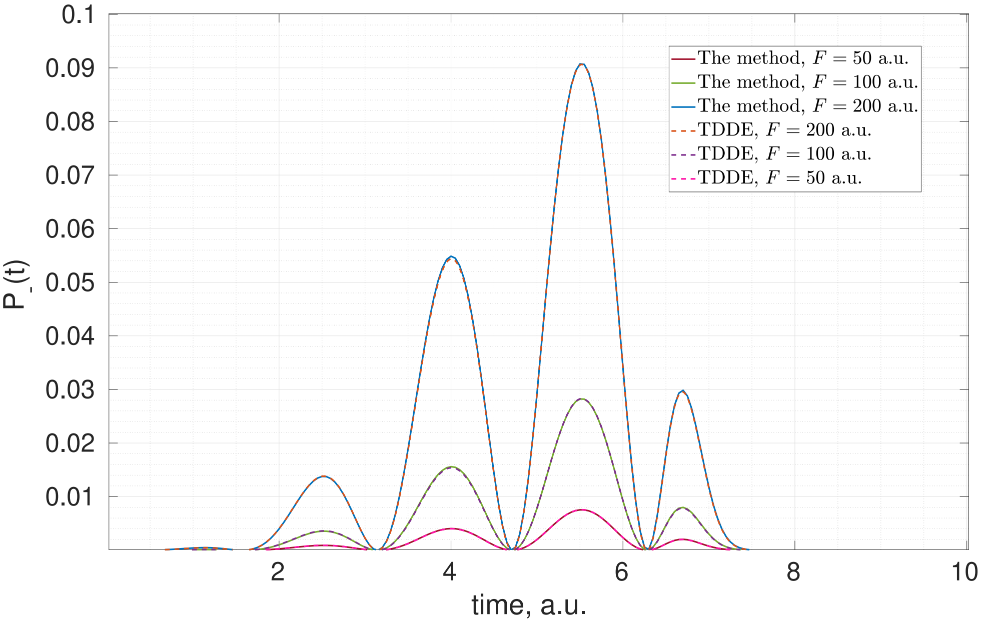

Figure 3.6: The share of negative energy states $P_{-}(t)$ [37] during the interaction. The laser field intensities used are $F = 50; 100, 200$ a.u. and the frequency $\omega = 2$ a.u. The results for the direct TDDE simulation and scaling coordinates method nearly coincide.

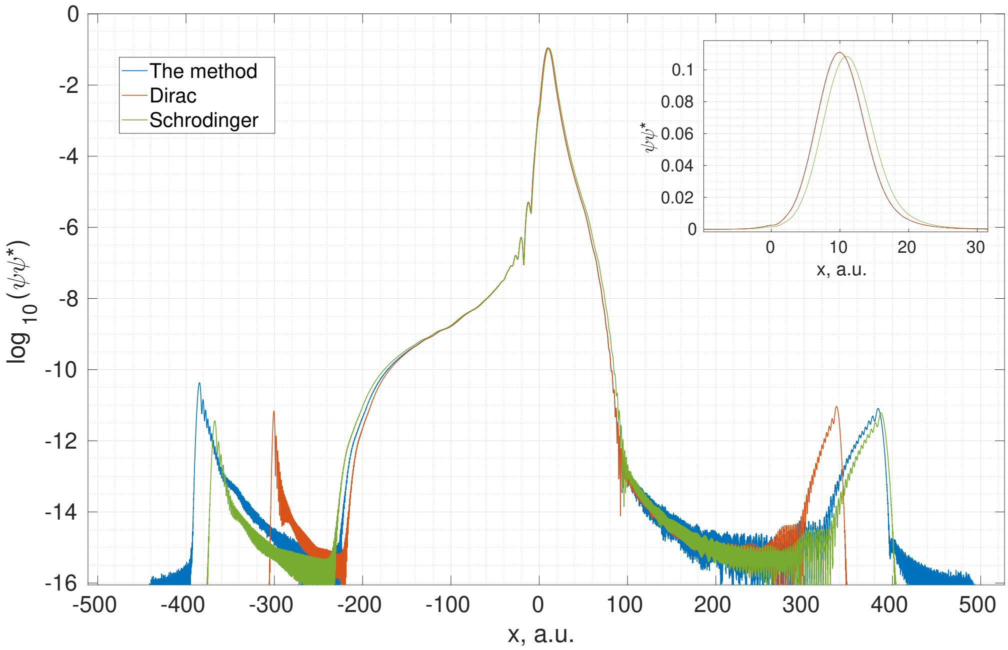

Figure 3.7: Electron density $\rho = \psi\psi^*$, calculated via the scaling method (blue), standard TDDE (red), and standard TDSE (green). The laser field is $F = 100$ a.u. and the frequency $\omega = 2$ a.u.

The electron energy spectrum after the interaction, resembling the one from [36], is shown in Fig. 3.8. Although we see an agreement for the spectrum, which correspond to the kinetic motions of the wave density, the small peaks corresponding to the scattering are overestimated in the FW case.

Regarding the computational efficiency of the method, we would like to emphasize its computational strengths and weaknesses. First, one is able to use larger Δt, which is a few orders larger than the one needed for the regular solution of TDDE (see Fig. 3.5). Second, it is possible to use a non-uniform mesh with step size Δx larger than π/mc outside the core of the potential, which reduces the total number of grid nodes. However, the process of calculating a kinetic exponent on each Δt via Krylov-Arnoldi method is more computational demanding, than a simple propagation via a diagonal matrix exponent as in a regular TDDE. Our pessimistic estimation of a speed-up, comparing to the standard approach, is moderate (2-4 times faster). For example, given a $\Delta t = 10^{-4}$, we obtain corresponding results, depicted in Figs. 3.5-3.8, in 190 minutes on a PC, while obtaining the Dirac solution with $\Delta t = 5 \cdot 10^{-6}$ takes 580 minutes, which yields 3 times acceleration. However, here we should note, that one can suggest different underlying criteria for the efficiency. For instance, if we use a deviation of the average coordinate as a metric alone (Table 1), then the results are more advantageous. Indeed, we can see a quadratic convergence for the standard TDDE (every $\Delta t/2$ yields $\sim$ deviation/4, as was expect with the split-operator approach) and the level of deviation ~ 0.02 must be achieved only with $t_{\text{comp}} \approx 2233$ minutes, which is $2233/190 \approx 11$ times slower, than the proposed method. Of course, there will still be a disagreement between the scattered and rescattered parts, which occurs because of the approximation discussed in 3.1.2. However, if those effects are considered negligible, then we can use this estimation as a measure of computational efficiency.

It is also important to note, that we use a very simple implementation of Krylov-Arnoldi method and, if this stage of the algorithm is improved (such as using the restarted Krylov subspace method or other advanced techniques), then the method is likely to receive a greater speed-up. The details on computations can be found in Appendix A.2.

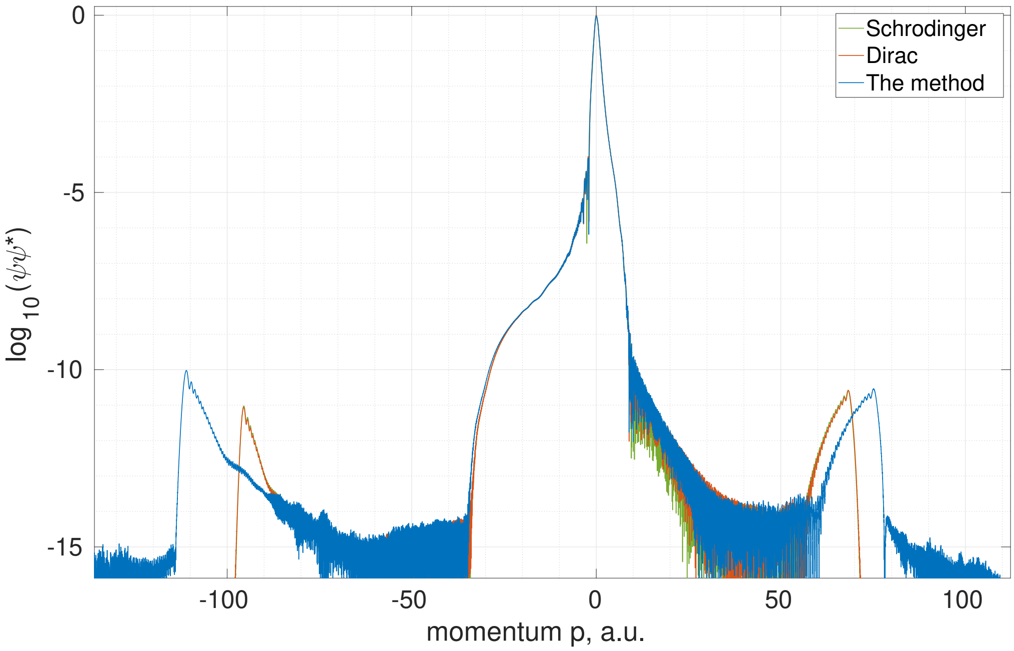

Figure 3.8: Momentum distribution after the interaction via $\hat{\rho} = \hat{\psi}\hat{\psi}^*$, calculated via the scaling method (blue), standard TDDE (red), and standard TDSE (green). The laser field is $F = 100$ a.u. and the frequency $\omega = 2$ a.u.

3.3 Conclusion

In this chapter, the coordinate scaling method for the numerical treatment of the atomic ionization problem in relativistically strong laser fields was developed. Here, the scheme of the relativistic generalization and the study of its performance is carried out for the case of the 1D ionization problem, which is extended straightforwardly to the 2D case in Chapter 3. The relativistic problem requires the application of an additional Foldy-Wouthuysen transformation along with the scaling method to avoid fast oscillation of the wave function due to the virtual transitions to negative energies. To do that, the quasiclassical approximation method, recently developed by Silenko, was invoked, in contrast to the more common v/c-approximation used in textbooks. For relativistic strong field ionization problem, the quasiclassical approximation is relevant as proved by seminal analytical results of Perelomov-Popov-Terent'ev (PPT) theory, see review [20]. PPT theory employs the electron quasiclassical (WKB) wave function in the continuum in laser and Coulomb fields, matching it with the bound wave function. The scaling method employs the same strategy: the initial state is described by the bound state wave function, while the propagation quasiclassically, which is a good approximation if the electron de-Broglie wavelength is smaller than the laser wavelength. Furthermore, the method can be applied in the more common

v/c-expansion version. Here, it will allow to discuss nondipole problems in weakly relativistic laser fields up to the order of v^2/c^2, including spin effects and spin-orbit coupling at ionization.

The accuracy of the results of the scaling method is proved in this chapter on a concrete example in the main region of the wave function. The sources of the inaccuracy on the tails of the wave function are analyzed. The computational advantage of the relativistic scaling method over the standard numerical TDDE [25] solution is demonstrated.

Chapter 4

Pulse duration effect in the nondipole x-ray strong field ionization in stabilization regime

4.1 Introduction

For a free electron in a strong laser field the nondipole and relativistic effects are negligible if the classical strong field parameter is small [4]:

$$a_0 = \frac{eA_0}{mc^2} = \frac{E_0}{mc\omega} \ll 1, \tag{4.1}$$

where A_0 is a magnitude of the electromagnetic vector potential, E_0 is an electric field strength and ω is a laser frequency. This is also the case in strong field ionization. The condition of Eq. (4.1) is easier to violate at low frequencies, for instance, $a_0 = 1$ is achieved in infrared laser fields with a wavelength $\lambda = 1000$ nm at a laser intensity $I = 10^{18}$ W/cm^2, while for x-rays $\lambda = 10$ nm, this would require $I = 10^{22}$ W/cm^2. However, recent advancement of strong laser technique in XUV and x-ray domain, in particular, the development of XFEL facilities in DESY, SLAC, and other places over the world, raised hopes to achieve nondipole interaction $a_0 > 0.1$ with x-rays.

In high-frequency laser fields $\hbar\omega > I_p$, the strong field ionization in the dipole domain can enter into the so-called stabilization regime [83]. When the electron oscillation amplitude in the laser field $\alpha = eE_0/m\omega^2$ exceeds the atomic size, $\alpha \gg a_B$, and the electron oscillation frequency is larger than the atomic frequency ($\hbar\omega > I_p$), the average effect of the atomic potential on the electron tends to be described by a quasi molecular potential with two potential centers [84]. This regime is characterized by the property that the ionization probability does not increase with increasing laser field strength, i.e., the ionization is stabilized. The photoelectron spectrum also has a distinctive symmetry. It is known that the nondipole effects tend to suppress the stabilization [85–87], and remarkably, all these properties are no longer valid for the nondipole case [88].

An ionization in nondipole regime, i.e. with nondipole parameter $a_0 \gtrsim 0.1$, turns out to have distinctive features. To begin with, the entire wave function experiences a shift in the propagation direction [88], due to the relativistic drift induced by $\mathbf{v} \times \mathbf{B}$ Lorentz force, which breaks the symmetry of the system [89]. One more distinctive feature is related to the photoelectron spectrum. The numerical calculations of the TDSE in a x-ray field [90] reveal, that the spectrum looses its symmetry along the propagation direction, similar to the above-threshold ionization in infrared fields [91, 92]. The same effect was observed in [93] for the x-ray laser with $a_0 \approx 0.07$ and the length of the pulse 10 optical cycles (OC). An interesting interplay between the nondipole and Coulomb fields has been observed in [94], where authors numerically solve TDSE within the Kramers-Hennerberg frame for the $3-15$ OC long pulses with $a_0 \approx 0.08 - 0.16$. The angular photoelectron spectrum in these cases has two distinctive features. Firstly, two lobes, which in the dipole case are perpendicular to the wave propagation direction $\mathbf{z}$, tend to bend towards the direction opposite to the laser propagation, $-\mathbf{z}$. The reason for this are Coulomb forces. An electron, ejected to the $\mathbf{z}$ direction, is not only a subject to the electromagnetic forces, which do not change the momentum at the end of the pulse. It also experiences and influence of the Coulomb force $\nabla V(\mathbf{r})$, which is directed as $-\mathbf{z}$. Secondly, there appears a new, third lobe, directed parallel to $-\mathbf{z}$. A later Ref. [93] also shows similar results for the x-ray laser with $a_0 \approx 0.07$ and 10 OC long pulse. Both [94] and [93] were focused on the analysis of the dominant low energy spectrum. Also, in [90] it is shown that the nondipole effects manifest themselves for the ATI peaks, too. In particular, it was shown, that nondipole corrections for the photoelectron energy spectra are small, but the shift of the lobes is again clearly visible for the angular distribution.

Since nondipole effects imply, that an electron moves relativistically fast, it is reasonable to take into account relativistic effects, which was done in [46] and [72] by numerically calculating full TDDE. In [46], an author shows the presence of relativistic effects for the x-ray laser with $a_0 \approx 0.05 - 0.15$, however, it turns out, that the spin effects are at least a few orders of magnitude smaller, then spin independent ones. In [72], authors again thoroughly confirm findings of [94], [90], [93] in the fully relativistic framework.

However, despite a great attention to the nondipole ionization, a matter of the dependence of ionization probability on the pulse duration largely remained untouched. The ionization in laser pulses of different durations is discussed in Ref. [93, 94], but only for a very limited number of pulse lengths (3, 5, 10, 15 optical cycles). In this chapter, a comprehensive analysis of the question is presented via the study of a wide range (0-45 optical cycles) of the pulse lengths. It turns out, that the ionization yield oscillates with respect to the pulse duration both in dipole and nondipole cases. Moreover, there are two different mechanisms, responsible for this behavior. An analysis of the low energy spectra and the influence of the oscillations on it are also presented, as well as the classical dynamics of the electron. For the sake of clarity and comparability with the previous results, all the results are calculated for the x-ray laser and $a_0 \approx 0.06 - 0.40$. We also employ a parameters scaling, which was previously described in detail in [72].

4.2 Theoretical considerations for the 2D case

4.2.1 Scaling coordinates approach in 2D

The are two main differences between the FW expressions for the 1D Eq. (3.10) and 2D cases. First, in 2D case spin dependent terms naturally arise. Second, non dipole effects become necessary in 2D case. Both of them arise from the fact, that the vector potential depends now on the coordinate

$$\mathbf{A} = A(t, z)\mathbf{e}_x. \tag{4.2}$$

Therefore, an O^2 term in Eq. (2.96) is expanded as

$$\epsilon = mc^2\sqrt{1 + \frac{\left(p_x - \frac{e}{c}A(t,z)\right)^2}{m^2c^2} + \frac{p_z^2}{m^2c^2} - \frac{e\hbar}{m^2c^3}\Sigma_y \cdot B_y} \tag{4.3}$$

where magnetic field $\mathbf{B} = \nabla \times \mathbf{A} = \partial_z A(t,z)\hat{\mathbf{e}}_y$ and Σ is defined in Eq. (2.99). Since we presume $\partial_z A(t,z) \sim \omega A(t,z)/c$ (see Appendix A.1), then the square root Eq. (4.3) can be expanded further as

$$\epsilon = mc^2\epsilon_0(\mathbf{p},t) - \frac{e\hbar}{2mc}\frac{1}{\epsilon_0(\mathbf{p},t)}\Sigma_y \cdot B_y + \mathcal{O}\left(\frac{\hbar^2\omega^2}{mc^2}a_0^2\right) \tag{4.4}$$

where

$$\epsilon_0(\mathbf{p},t) = \sqrt{1 + \frac{\left(p_x - \frac{e}{c}A(t,z)\right)^2}{m^2c^2} + \frac{p_z^2}{m^2c^2}} \tag{4.5}$$

with the relativistic field parameter $a_0 = eA/(mc^2)$. As a result, there are no more matrices inside the square root ϵ_0, which simplifies calculations. However, the variables from different coordinate spaces, namely momenta p_x and p_z are still mixed with the regular coordinate z. In order to overcome this hurdle and clarify, how to treat the square root, we can expand it into a Taylor series. To do that, we write down $\epsilon_0(\mathbf{p}, t)$ as

$$\epsilon_0(\mathbf{p}, z, t) = \sqrt{1 + X(\mathbf{p}, z, t)} = 1 + \frac{1}{2}X(\mathbf{p}, z, t) - \frac{1}{8}X(\mathbf{p}, z, t)X(\mathbf{p}, z, t) + \dots \tag{4.6}$$

note, that the term $X^2(\mathbf{p}, t)$ produces terms, proportional to $\partial_z A(t, z)$ and $\partial^2_{zz} A(t, z)$ and so on. Thus, it makes sense to single out the terms by the different orders of $\partial^n_z A(t, z)$ and then roll back the expanded expressions (in other words, to inverse Eq. (4.6))

$$\begin{aligned}
\epsilon_0 =& \sqrt{1 + \frac{\left(-i\hbar\partial_x - \frac{e}{c}A(t,z)\right)^2}{m^2c^2} - \frac{\hbar^2\partial^2_{zz}}{m^2c^2}} = \sqrt{1 + \frac{\left(-i\hbar\partial_x - \frac{e}{c}A(t,\tilde{z})\right)^2}{m^2c^2} - \frac{\hbar^2\partial^2_{zz}}{m^2c^2}} - \\
&- \frac{i}{2}\frac{\hbar}{m^2c^2}\frac{e}{c}\frac{\partial A(t,z)}{\partial z} \cdot \left[\frac{\left(-i\hbar\partial_x - \frac{e}{c}A(t,\tilde{z})\right)}{mc}\frac{\left(-i\hbar\partial_z\right)}{mc}\right]\left[1 + \frac{\left(-i\hbar\partial_x - \frac{e}{c}A(t,\tilde{z})\right)^2}{m^2c^2} - \frac{\hbar^2\partial^2_{zz}}{m^2c^2}\right]^{-3/2} + \\
&+ \mathcal{O}\left(\frac{\hbar^2\omega^2}{m^2c^4}a_0^2\right), \quad \tilde{z} = z
\end{aligned} \tag{4.7}$$

Here the designation $\tilde{z} = z$ means, that derivative operators do not act on $A(t, z)$. In Eq. (4.7) we omit terms, proportional to $(\partial_z A(t, z))^2$ and $\partial^2_{zz} A(t, z)$, because they are $\hbar^2\omega^2/(m^2c^4)$ small.

The question to address now is how to act with the operator ϵ_0 in form Eq. (4.7) onto a wavefunction ψ, written as $\psi = \phi e^{i\varphi}$ (Eq. (2.53)). To do that, we can expand the first term into Taylor series Eq. (4.6) and then group the terms with the same order of $\lambda = \hbar/(mc)$ back. As a result, we obtain an expression, similar to the 1D case Eq. (3.13)

$$\begin{aligned}
&\sqrt{1 + \frac{\left(-i\hbar\partial_x - \frac{e}{c}A(t,\tilde{z})\right)^2}{m^2c^2} - \frac{\hbar^2\partial^2_{zz}}{m^2c^2}}\ \phi(x,z)\ e^{i\varphi(x,z)} = \phi T_0(x,z,t) - \\
&- i\lambda\left[\phi'_x T_{1,x}(x,z,t) + \phi'_z T_{1,z}(x,z,t)\right] - \\
&- \frac{\lambda^2}{2}\left[\phi''_{xx} T_{2,xx}(x,z,t) + 2\phi''_{xz} T_{2,xz}(x,z,t) + \phi''_{zz} T_{2,zz}(x,z,t)\right] + \mathcal{O}\left(\lambda^3/\lambda_e^3\right).
\end{aligned} \tag{4.8}$$

where we presume, that $\phi' \sim 1/\lambda_e$ and $\lambda/\lambda_e \ll 1$, i.e. function ϕ does not contain large relativistic oscillations. The second term can be written in the same manner

$$\left[\frac{\left(-i\hbar\partial_x - \frac{e}{c}A(t,\tilde{z})\right)}{mc}\frac{\left(-i\hbar\partial_z\right)}{mc}\right]\left[1+\frac{\left(-i\hbar\partial_x - \frac{e}{c}A(t,\tilde{z})\right)^2}{m^2c^2} - \frac{\hbar^2\partial_{zz}^2}{m^2c^2}\right]^{-3/2} = \\ = \phi W_0(x,z,t) - i\lambda\Big[\phi'_x W_{1,x}(x,z,t) + \phi'_z W_{1,z}(x,z,t)\Big] + \mathcal{O}\left(\lambda^2/\lambda_e^2\right) \tag{4.9}$$

where we omit λ^2 terms, because the coefficient by the term in Eq. (4.7) is proportional to $\hbar\omega/(mc^2)$ itself. The functions $T(x,z,t)$ and $W(x,z,t)$ can be found in Appendix A.2.

Recalling Eq. (2.96) and using Eq. (4.3),(4.7), it is possible to write down FW Hamiltonian for the 2D case in the similar way

$$H_{FW} = \beta mc^2\epsilon_0 - \frac{e\hbar}{2mc}\frac{1}{\epsilon_0}\beta\Sigma_y \cdot B_y + V + \frac{e\hbar}{8m^2c^4}\left\{\frac{1}{\epsilon_0(\epsilon_0+1)}, \Big[\boldsymbol{\Sigma}\cdot(\boldsymbol{\pi}\times\tilde{\mathbf{E}} - \tilde{\mathbf{E}}\times\boldsymbol{\pi}) - \hbar\Delta V\Big]\right\} + \mathcal{O}(\lambda^2/a_E^2 \tag{4.10}$$

where

$$\boldsymbol{\pi} = \boldsymbol{p} - \frac{e}{c}\mathbf{A}, \quad \tilde{\mathbf{E}} = \nabla V - \frac{1}{c}\dot{\mathbf{A}}. \tag{4.11}$$

With the Hamiltonian Eq. (4.10) it is possible to write a FW governing equation, similar to the Eq. (3.21).

One more question to address is a calculation of the smooth (i.e. $\varphi \gg \varphi'(t,x,z)\lambda$) phase $\varphi(t,x,z)$. In the 1D case it could be done by means of the Algorithm 1. However, in 2D case the situation is more complicated, because we no longer can include the effects from the vector potential $\mathbf{A}$ into the phase by using the kinetic momentum $\boldsymbol{\pi} = \boldsymbol{p} - \frac{e}{c}\mathbf{A}$ instead of the canonical $\boldsymbol{p}$. Thus, we no longer know the exact phase in the momentum space $\hat{\varphi}(p,t)$ of the electron for the $V = 0$ case and consequently unable to deduce the phase $\varphi(x,t)$ Of course, there is a workaround for such a problem. After all, the phase $\varphi(x,z,t)$ should not necessary be exact, it is enough, if it absorbs just most of the kinetic relativistic oscillations.

Let us consider SKGE for the electron, exposed to the laser field

$$\begin{cases} i\hbar\dot{\psi}(x,z,t) = \epsilon_0\psi(x,z,t) \\ \psi(x,z,0) = \psi_0(x,z) \end{cases} \tag{4.12}$$

where ϵ_0 is defined in Eq. (4.5). Using Eq. (4.7), we can write down

$$i\hbar\dot{\psi}(x,z,t) = \sqrt{1+\frac{\left(-i\hbar\partial_x - \frac{e}{c}A(t,\tilde{z})\right)^2}{m^2c^2} - \frac{\hbar^2\partial_{zz}^2}{m^2c^2}}\,\psi(x,z,t) + \mathcal{O}\left(\frac{\hbar\omega}{mc^2}a_0\right) \tag{4.13}$$

where $\tilde{z} = z$ in the same sense, as in Eq. (4.5), i.e. $\partial_z(A(\tilde{z}) \cdot f(z)) = A(z)f'(z)$. One can think of $\tilde{z}$ as of point, at which we expand $A(z)$ into the Taylor series. Thus, if we consider $\tilde{z}$ to be a parameter, then $A(\tilde{z})$ is not affected by the FT: $\{x, z\} \to p_x, p_z$. If so, then we are able to write Eq. (4.14) as

$$i\hbar\dot{\psi}(x, z = \tilde{z}, t) = F^{-1}\left[\sqrt{1 + \frac{\left(p_x - \frac{e}{c}A(t, \tilde{z})\right)^2}{m^2c^2} + \frac{p_z^2}{m^2c^2}}\hat{\psi}(p_x, p_z, t)\right] + \mathcal{O}\left(\frac{\hbar\omega}{mc^2}a_0\right). \tag{4.14}$$

Then, the "solution" becomes

$$\psi(x, z = \tilde{z}, t) = F^{-1}\left[\exp\left(-\frac{i}{\hbar}\int_0^t \sqrt{1 + \frac{\left(p_x - \frac{e}{c}A(t', \tilde{z})\right)^2}{m^2c^2} + \frac{p_z^2}{m^2c^2}}dt'\right)\hat{\psi}(p_x, p_z, t)\right] + \mathcal{O}\left(\frac{\hbar\omega}{mc^2}a_0\right). \tag{4.15}$$

Of course, the expression Eq. (4.15) is useless for the real calculations. Indeed, in order to calculate the solution for the just one point (x, z) in space, one must conduct the corresponding time integration in the entire space $\{p_x, p_z\}$. So, if the coordinates (as well as the corresponding momentum space) are discretized on the grid with N^2 nodes, then the number of operations to calculate the solution at every point scales as $\sim N^2 \cdot N^2 \log N$, which is inappropriate even for small $N = 100$. However, Eq. (4.15) provides us with a very useful insight regarding the phase in momentum space $\hat{\varphi}$

$$\hat{\varphi}(p_x, p_z, \tilde{z}, t) = -\int_0^t \sqrt{1 + \frac{\left(p_x - \frac{e}{c}A(t', \tilde{z})\right)^2}{m^2c^2} + \frac{p_z^2}{m^2c^2}}dt'. \tag{4.16}$$

Since we consider $\hbar\omega \ll mc^2$ and $\hat{\varphi}$ to be smooth, then it is enough to calculate Eq. (4.16) for a few reference values $\tilde{z}$ and then interpolate to obtain $\hat{\varphi}(p_x, p_z, z, t)$ for any z. Interpolation can be done via, for example, splines, or with Chebyshev polynomials, because we are free to choose reference nodes $\tilde{z}$. Then, the algorithm becomes 2.

In fact, the Algorithm 2 provides us with a decent choice of the phase φ. On Fig. 4.1 the module of the smooth envelope function $\hat{\phi}(\mathbf{p})$ and the wave function $\hat{\psi}(\mathbf{p})$ are presented. One can clearly see, that $\hat{\phi}(\mathbf{p})$ is more narrow, than $\hat{\psi}(\mathbf{p})$, and located closer to the origin. That means, that in the coordinate space function $\phi(\mathbf{x})$ is much more smooth, than the wavefunction $\psi(\mathbf{x})$.

4.2.2 Spectrum calculation

The calculation of the photoelectron spectrum has been in the focus of the community for many years. The methods to solve this problem range from projecting onto the

Algorithm 2 The procedure of the phase φ calculation at each time step Δt

```
Calculate $\hat{\varphi}(p_x, p_z, \tilde{z}, t) = \int\limits_0^t \sqrt{1 + \frac{\left(p_x - \frac{e}{c}A(t', \tilde{z})\right)^2}{m^2c^2} + \frac{p_z^2}{m^2c^2} dt'}$ for every reference value $\tilde{z} \in [-L_z, L_z]$.
Interpolate $\hat{\varphi}(p_x, p_z, \tilde{z}, t)$ to get $\hat{\varphi}(p_x, p_z, z, t)$.
Calculate critical points $x_0(p_x, p_z) = -\frac{\partial \hat{\varphi}}{\partial p_x}$ and $z_0(p_x, p_z) = -\frac{\partial \hat{\varphi}}{\partial p_z}$.
Calculate the phase as $\varphi(x)|_{x=x_0(p)} = \hat{\varphi}(p) p x_0(p)$.
Rescale $x' = \beta(t)x$ and $z' = \beta(t)z$. Since the set of points $\{x_0, z_0\}$ is non uniform and does not make up a grid but rather a mesh, it complicates an interpolation $\varphi(x, z) \to \varphi(x', z')$. One can use different technics for the solving of optimization problem in order to interpolate from the 2D non uniform mesh to the other non uniform mesh.
```

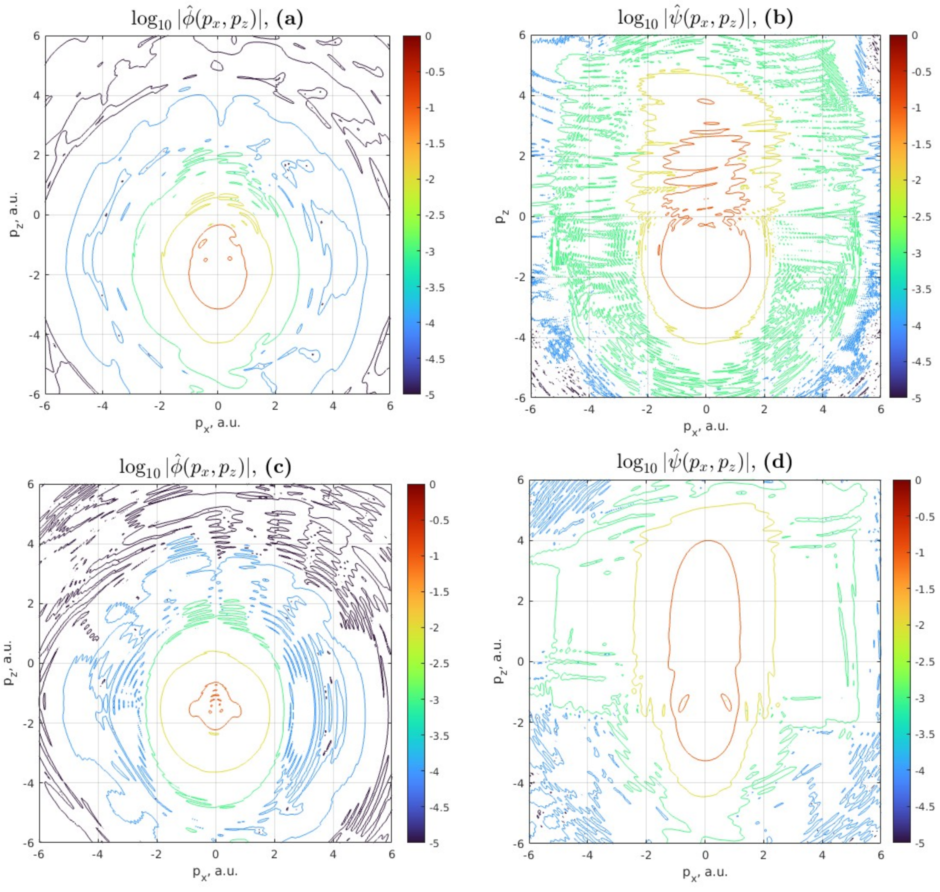

Figure 4.1: The comparison of the envelope function $|\hat{\phi}(\mathbf{p})|$ and the original wave-function $|\hat{\psi}(\mathbf{p})|$. Parameters of the field: $\omega = 14$ a.u., $E = 400$ a.u., $a_0 = 0.21$. (a) $\hat{\phi}(\mathbf{p})$ after 8 cycles, (b) $\hat{\psi}(\mathbf{p})$ after 8 cycles, (c) $\hat{\phi}(\mathbf{p})$ after 30 cycles, (d) $\hat{\psi}(\mathbf{p})$ after 30 cycles

continuum states with proper asymptotic behavior [72] to advanced techniques, working with the boundary of the simulation box [95, 96]. Here in this thesis the former approach is used, because the spreading of the wave function is taken into account by the coordinate scaling.

The main problem with the projecting onto the continuum states in our case is the lack of analytic forms for such functions for the soft-coulomb potential in 2D. In order to overcome it, one can derive the analytic form for the regular Coulomb potential in 2D and expect, that they coincide with a good degree of accuracy for some large enough distance $r > r_0$.

The 3D continuum states for the Coulomb potential can be found in [97] and their relativistic counterparts in [71]. The derivation, used there, can be adopted for the 2D case. If we introduce 2D parabolic coordinates as

$$\begin{cases} x = \sigma\tau \\ z = (\tau^2 - \sigma^2)/2, \end{cases} \tag{4.17}$$

then, following the main steps from [97], one can write down an electron's continuum state with an energy $E = p^2/2m$ as a plane wave combined with the incoming spherical wave (in a.u.)

$$w(\sigma,\tau) = 1F_1\left(i\frac{Z}{p}, \frac{1}{2}, ip\sigma^2\right) \; e^{ip(\tau^2-\sigma^2)/2} \tag{4.18}$$

where ${}_1F_1$ is a generalized hypergeometric function. In the relativistic case $w(\sigma,\tau)$ becomes

$$w(\sigma,\tau) = 1F_1\left(iZ\frac{\sqrt{1+p^2/(m^2c^2)}}{p}, \frac{1}{2}, ip\sigma^2\right) \; e^{ip(\tau^2-\sigma^2)/2}. \tag{4.19}$$

The function $w(\sigma)$ in the non relativistic limit solves the Schrodinger equation

$$\Delta w + 2\left(E + \frac{2Z}{\tau^2+\sigma^2}\right) = 0, \tag{4.20}$$

however, in the simulations in Chapter 4 the Soft Coulomb potential V [40] is used instead of the regular Coulomb V_c one. In the parabolic coordinates they read

$$V(\sigma,\tau) = -\frac{3}{2}\frac{Z}{\sqrt{3/Z^2 + \frac{\sigma^2+\tau^2}{4}}}, \quad V_c(\sigma,\tau) = -\frac{2Z}{\sigma^2+\tau^2}. \tag{4.21}$$

If we choose the same nuclear charge Z for both V and V_c, then corresponding $w(Z)$ does not deliver the solution if we insert V instead of V_c into Eq. (4.20) because $V \to -3Z/(2r)$ and $V_c \to -Z/r$. Therefore, Z used as a parameter to calculate $w(Z)$

must be $Z_w = 2Z/3$. The residue $(H-E)w$ for the soft Coulomb He$^+$ atom is shown on Fig. 4.2.

As we may see, for $r_0 > 5.0$ a.u. the difference becomes negligible. In Chapter 4 the spectrum is usually calculated after the $t = 20$ a.u. passed after the end of the laser pulse. That means, that if we exclude an area $r < r_0$, then we omit electrons with velocities $v < 0.25$ a.u. and, thus, energies $E < 0.04$ a.u. One can consider it acceptable, because we are mostly interested in photoelectron energies $E > 0.10$ a.u.

In practice, it turns out, that functions $w(\sigma, \tau)$ can be replaces by the simple plane waves. For the systems, studied in Chapter 4 , the spectra, obtained via the projection onto w states and plane waves turn out to be qualitatively indistinguishable from each other. This stems from the fact, that the function ${}_1F_1$ approaches the constant limit, as the distance from the core r and considered energies E grow.

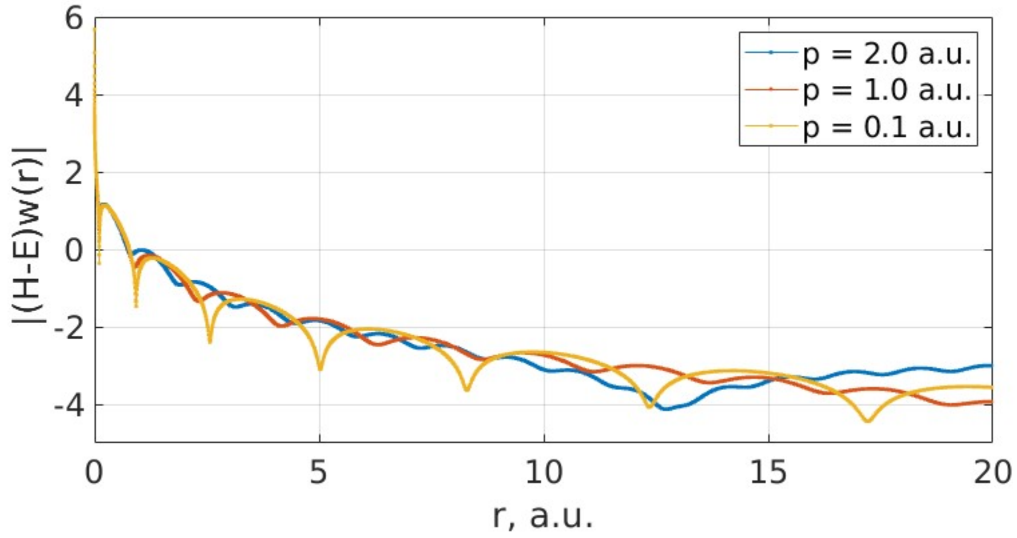

Figure 4.2: The deviation of the Coulomb scattering state $w(r)$ from the soft Coulomb scattering state.

4.3 2D quantum relativistic simulations

In this section the question of 2D simulations is addressed and the difference between nondipole and pure relativistic (such as mass shift) effects. In general, the corresponding versions of an equation of motion (Eqs. (3.20) and (3.21)) are obtained using a

2D Hamiltonian Eq. (4.10), which has additional terms, comparing to its 1D counterpart. From the computational point of view, these terms are treated similar to the square-root term ϵ Eq. (4.8).

As an observable to discuss the ionization probability is chose, since it exhibits distinctive features in the 2D case. The ionization probabilities are qualitatively different in nonrelativistic and relativistic cases due to the presence of nondipole effects in the latter, which eliminates the nonrelativistic stabilization phenomenon [98]. Also the nonrelativistic scaling law with respect to the charge of the atomic core fails in the relativistic domain and we expect the ionization rate to be different for different atomic species. As an example, we calculate the results for hydrogen and helium, and compare them to the 3D simulation by Telnov and Chu [72].

In the 2D simulation, a soft Coulomb potential is used [40,99], as usual in reduced dimensions.

$$V(r) = -\frac{3}{2}\frac{Z}{\sqrt{r^2 + 3/Z^2}} \tag{4.22}$$

with $Z = 1 - 4$ being a nuclear charge. The other parameters, such as the laser field frequency ω and peak field F were taken from [72] and correspondingly scaled for different Z [98]. As a consequence, the peak field scales as $F(Z) = FZ^3$, and the frequency as $\omega(Z) = \omega Z^2$. In this section, the same short pulse with four periods (τ) is used as in [72], with $\mathbf{A} = A(t, z)\mathbf{e}_x$

$$A(t, z) = \frac{cF}{\omega} \cdot \exp\left[-2 \cdot \ln(2) \cdot \left(\frac{t - z/c}{\tau}\right)\right] \cdot \sin\Big(\omega\,(t - z/c)\Big). \tag{4.23}$$

In order to distinguish high-order relativistic effects from the nondipole ones, we additionally perform a simulation of nondipole TDSE with the following Hamiltonian:

$$H_{\text{nondipole}} = \frac{1}{2}\left(p_x - \frac{e}{c}A(t, z)\right)^2 + \frac{1}{2}p_z^2 + V(r). \tag{4.24}$$

The results of calculations presented in Fig. 4.3 exhibit a few distinguishable features. First, an influence of the nondipole character of the field is evident. We attribute the difference between dipole and nondipole calculations to the fact, that ionization rate is mostly defined by the shift of the wave packet $\langle r \rangle = \sqrt{\langle x \rangle^2 + \langle z \rangle^2}$ from the centre of the potential after the end of the pulse. Since the magnetic field is present, then, due to the Lorentz force induced drift in the laser propagation direction, we have $\langle z \rangle \gg \langle x \rangle$ after the end of the pulse. Second, we can also notice a difference between relativistic and nonrelativistic calculations. The ionization probabilities in the relativistic case are lower than in the nondipole case. This is because the relativistic

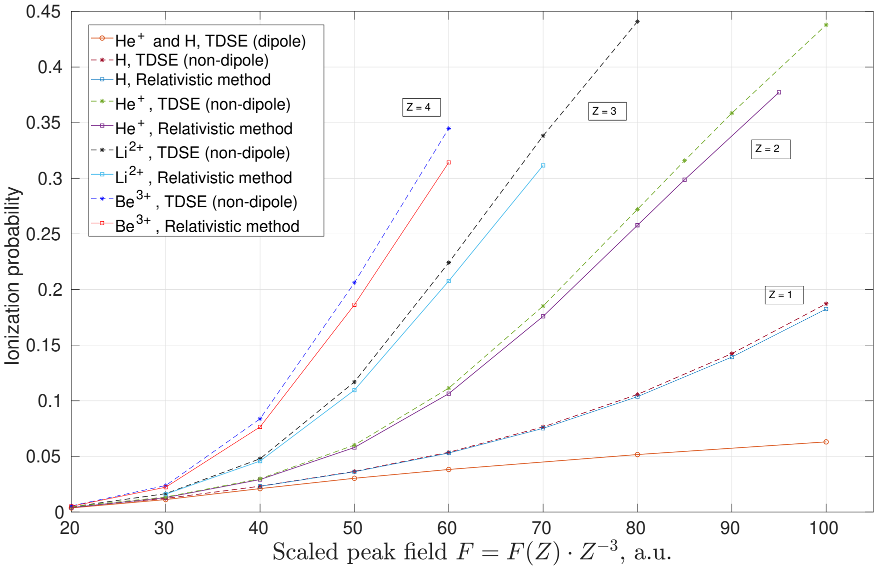

Figure 4.3: Ionization probabilities for ions $Z = 1 - 4$ in the laser field. Laser parameters are scaled, the peak field $F(Z) = FZ^3$ and the frequency as $\omega(Z) = \omega Z^2$. Dashed lines with stars – nondipole TDSE (4.24) calculations, solid lines with cubes – relativistic calculations with scaling method, solid line with circles – dipole TDSE calculations.

mass correction suppresses the drift and the final distance of the wave packet from the atomic center is decreased. Since the mass shift increases with rising a_0, the deviation of the ionization probability between relativistic and nonrelativistic nondipole cases grows along with the relativistic field parameter $a_0 \sim Z$.

Comparing to 3D calculations of Telnov and Chu [72], the results of calculations presented in Fig. 5 show deviations of the relativistic result from the nonrelativistic one larger than 10%, for hydrogen at $F > 40$ a.u., and for helium at $F > 25$ a.u. which is in a qualitative accordance with the 3D result of Ref. [72]. The dipole calculations show stabilization behavior of the ionization rate, which is suppressed in the relativistic case, again similar to the 3D calculation. While we have coincidence of the qualitative characteristic features in 2D and 3D cases, the details of the ionization rate behavior still slightly differ, which stem from the reduced dimension, and using a soft Coulomb potential in the reduced number of dimensions, rather than a regular Coulomb potential. These results indicate that the method is applicable in two dimensions without additional principal complications. The computational advantage of the scaling method in the 2D case for TDDE is expected to be similar to that of the TDSE discussed in Ref. [58].

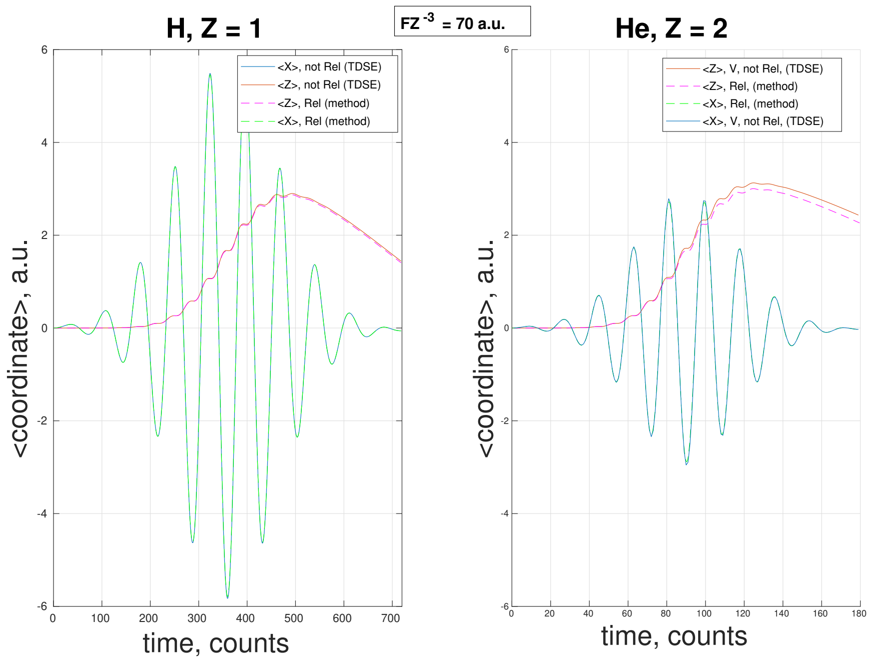

Figure 4.4: Trajectory of an electron during the laser pulse. Both TDSE (nondipole) and "the method" trajectories are depicted.

4.4 Dipole case

In this section, the ionization probability dependence on the laser pulse duration is investigated. Let us start with a comparison (Fig. 4.5) of nondipole and dipole calculations for the following parameters, typical for the stabilization regime: $a_0 = 0.13$, $Z = 2$, $\omega = 14$ a.u. (381 eV), $E = 240$ a.u. ($I = 2 \times 10^{21}\mathrm{W/cm}^2$), $\gamma = 0.12$, $EZ^{-3} = 30$ a.u., $\alpha \approx 1.22$. Here the parameters scaling [72] is employed and helium ($Z = 2$) is chosen as a model to have a pronounced Coulomb effect. The laser vector-potential $\mathbf{A}$ has only one component, namely A_x, which is given by the formula

$$\begin{aligned} A_x(\eta) &= A_0 e^{-2\ln(2)(\eta/\tau)}\sin(\omega\eta); & \eta &= t - 2\tau - z/c, & t &< 2\tau \\ &= A_0\sin(\omega\eta); & \eta &= t - 2\tau - z/c, & 2\tau &< t < N_T\frac{2\pi}{\omega} + 2\tau \\ &= A_0 e^{-2\ln(2)(\eta/\tau)}\sin(\omega\eta); & \eta &= (t - N_T\frac{2\pi}{\omega} - 2\tau) - z/c, & N_T\frac{2\pi}{\omega} + 2\tau &< t \end{aligned} \tag{4.25}$$

where $\eta = t - z/c$ for the nondipole and $\eta = t$ for dipole cases. The duration of turn on and turn off is regulated by the parameter τ. Between the turn on and turn off, the pulse consists of a simple plane wave with a period of oscillations $T = 2\pi/\omega$. In order to investigate the dependence of the ionization on the length of the pulse, we can run multiple simulations for the different number N_T of periods T in the middle of the pulse.

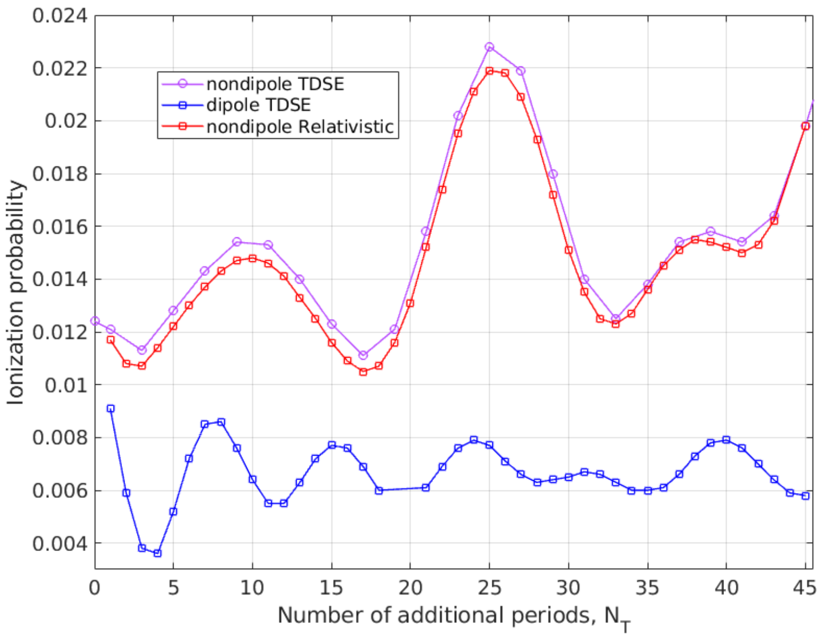

Figure 4.5: Ionization probability in dependence of the laser pulse duration , $a_0 \approx 0.13$, $Z = 2$, $\omega = 14$ a.u., $E = 240$ a.u., $\gamma = 0.12$, $EZ^{-3} = 30$ a.u.; magenta line – relativistic calculations according to the scaling method, blue line – dipole approximation, red line – nondipole TDSE. Length of the pulse is $T = N_T \cdot 2\pi/\omega + 6\tau$.

One can see in Fig. 4.5, that the ionization probabilities exhibit two key features: the ionization probability oscillates with a number of cycles; the ionization probability oscillations are significantly different in dipole and nondipole calculations, both shape-wise and amplitude-wise.

In the dipole calculation, ionization probability oscillates near an average value $P_I \approx 0.7\%$. The oscillations seem to have a constant period $T_{\mathrm{osc}} \approx 4$ a.u. Further, we will see the origin of this value and why the frequency of the oscillations is independent on the total duration of the respective pulse.

In the nondipole calculations, one can also spot oscillations, which have bigger amplitude and depend on the total duration of the pulse. Also, the nondipole effect doubles an ionization probability, making it $P_I \approx 1.4\%$. The mechanism of the nondipole oscillations is discussed in Section 4.5.

In order to address oscillations of the ionization probabilities with a number of cycles, we focus in this section on the dipole case with smaller field parameter $a_0 = 0.13$.

A typical function of the ionization probability depending on the pulse duration, $P_I(N_T) \approx 0.5\%$, is shown in Fig. 4.5. For the corresponding case, the photoelectron energy spectra are given in Figs. 4.6,4.7. From the analysis of Fig. 4.5, we can notice, that the ionization probability oscillates over the number of additional periods N_T (between switching on and off of the laser pulse) with a period of oscillations $T_{\text{osc}} \approx 2 \cdot 4.38$ cycles $= 3.96$ a.u.. An origin of this phenomenon can be understood via the analysis of the spectra in Fig. 4.7, which show the spectra for the pulses with different number of cycles N_T. The chosen pulse durations N_T correspond to the local maxima or minima of the P_I from Fig. 4.5. The spectrum is calculated according to the Sec. 4.2.2 after the interaction of the system with the laser field.

We firstly notice that spectral density at the continuum threshold, energy $E = 0$, is vanishing. This corresponds to the fact, that the final ionized part of the wave function is anti-symmetric (up to 3-4 digits of accuracy). It is in accordance with the photoelectron energy distribution (PED) scaling at the threshold at high-laser frequencies [100]. Secondly, one can again see oscillations, whose period depends on the duration of the pulse. In fact, these oscillations can be explained by the dynamic interference [101]. Indeed, if we assume, that variables E and t make up a Fourier pair $Et/\hbar$, then we expect the energy spectrum to be a Fourier transform of a function $f(t)$, describing a process of ionization with time:

$$S(E) = \int_0^\infty f(t) e^{iEt/\hbar} dt \tag{4.26}$$

Our suggestion is that ionization unfolds mainly during the pulse turn on and turn off [101]. Indeed, if the opposite was true, we would expect continuous growth of the ionization probability with the number of cycles. Then, one can present function f as

$$f(t) = f_1(t) + f_1(t - T), \tag{4.27}$$

where T is (roughly) a time between the start and the end of the pulse. According to the properties of the Fourier transform, the radial spectrum in this case is:

$$S(E) = S_1(E) + S_2(E) e^{iET/\hbar} \tag{4.28}$$

Let us examine parameter T a bit closer. A rough estimation can be given by a simple assumption, that

$$T = N_T \frac{2\pi}{\omega}. \tag{4.29}$$

However, it also makes sense to take into account, that the ionization function $f_1(t)$ must smoothly become zero after the end of the turn on stage. That means, that the

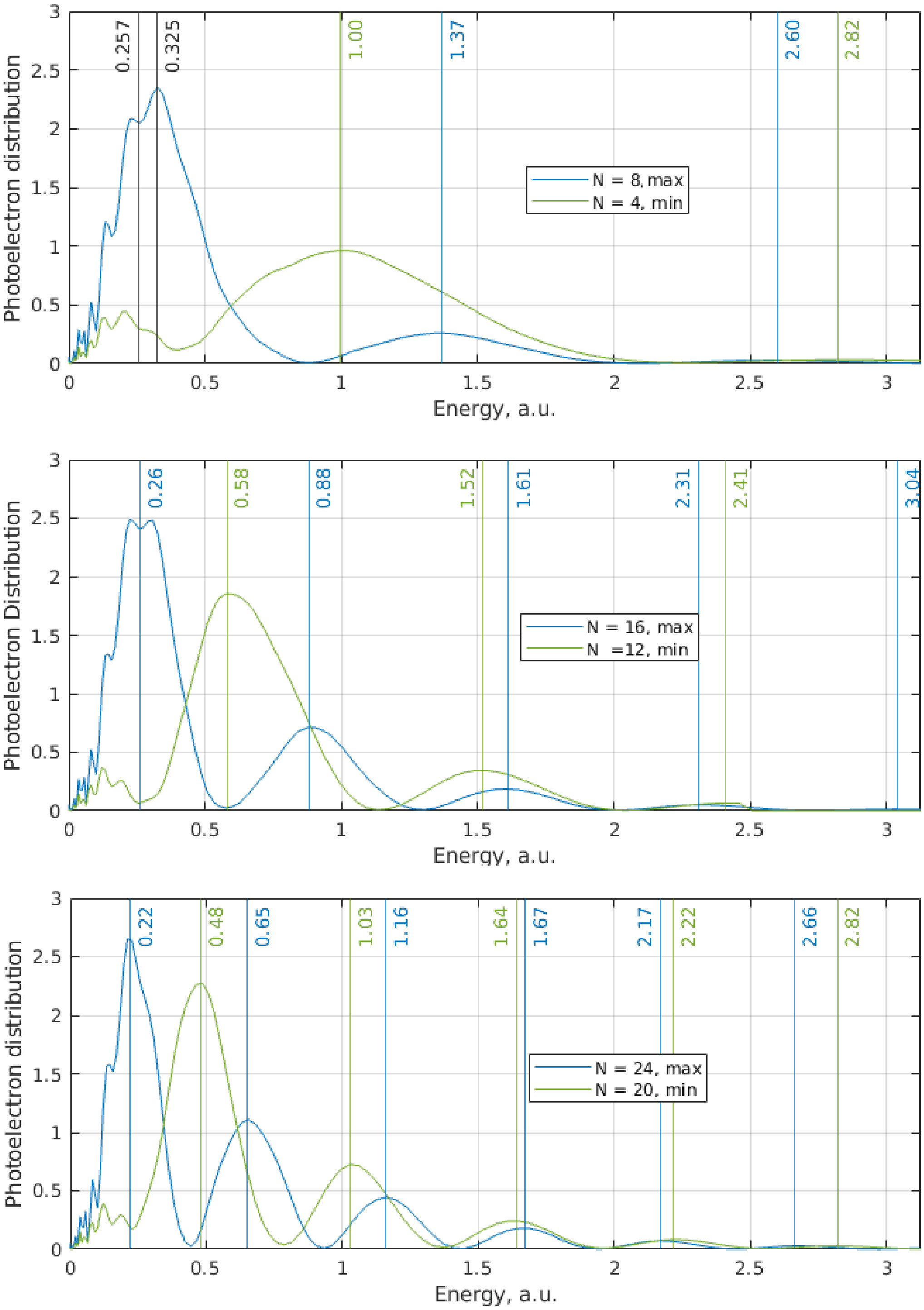

Figure 4.6: Photoelectron density in dipole case, $a_0 \approx 0.13$, $EZ^{-3} = 30$ a.u.,$\omega = 14$ a.u. Corresponds to ionization probabilities from fig. 4.5.

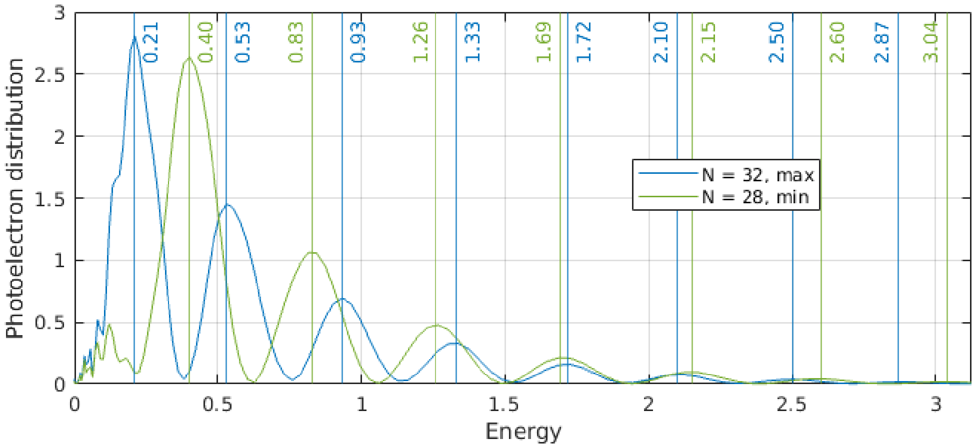

Figure 4.7: PED in dipole case, $a_0 \approx 0.13$, $EZ^{-3} = 30$ a.u., $\frac{e}{c}A_0 = 17.14$ a.u., $\omega = 14$ a.u. Corresponds to ionization probabilities from fig. 4.5.

center of $f_1(t)$ is located roughly in the middle of the turn on stage. We estimate this offset as τ, which is a characteristic of the turn on time. The same logic applies for the turn off. Hence,

$$T = \frac{3}{2}\tau + N_T\frac{2\pi}{\omega}. \tag{4.30}$$

the period of modulation of the energy spectrum, given by Eq. 4.30, match those we can observe in Fig. 4.7. To achieve even better agreement, we need to estimate a shape of the function $f_1(t)$. This can be done again from the analysis of the peaks of the spectrum. If we take a look at Fig. 4.7, we can see, that the distance between the peaks $E_0 \approx \hbar/T$ is nearly constant for N_T, corresponding to minima, and for every peak except the first one for N_T, corresponding to maxima. Also, one can point out, that peaks follow an exponential decay in amplitude, i.e. every next peak is n times smaller, than the previous. The corresponding results can be found in table 4.4:

N_T	12	20	28
$n = \text{env}[S_1^2(E+E_0)] \ / \ \text{env}[S_1^2(E)]$	0.19	0.33	0.45
E_0, a.u.	0.9	0.6	0.44

Therefore, we claim, that an envelope of the radial spectrum is

$$\text{env}[S_1(E)] = e^{-\text{const}\cdot|E|} \tag{4.31}$$

and

$$\text{env}[S_1(E+E_0)] \ / \ \text{env}[S_1(E)] = e^{-\text{const}\cdot|E_0|} \approx \sqrt{n}, \ E_0 = \hbar/T. \tag{4.32}$$

Then, we can get an estimation for the const. It turns out, that const $\approx 1.25\tau$. Let us take const $= \tau$ for simplicity. Indeed, if we recall a property of Fourier transform

$$F[f(\text{const}\cdot t)] = \hat{f}(t/\text{const}), \tag{4.33}$$

then it becomes clear, that the const represents a width of the ionization function $f_1(t)$. As was mentioned earlier, this is the parameter τ in accordance with the energy-time uncertainty relation. As a result,

$$f_1(t) = \frac{1}{1+(t/\tau)^2}. \tag{4.34}$$

If we plot a Fourier transform of the function

$$f(t) = \frac{1}{1+(t/\tau)^2} + \frac{1}{1+((t-T)/\tau)^2}, \tag{4.35}$$

with T from Eq. (4.30), then we obtain oscillations with the correct frequency for the minima ($N_T = 12, 20, 28$). However, the position of the very first peak is correct only for the large $N_T = 20, 28$, because for the small N_T the turn on and turn off stages are still very close to each other. However, the result for maxima fails. The thing is that for the maxima, Eq. (4.35) with a changed sign delivers correct results

$$f_{\text{max}}(t) = \frac{1}{1+(t/\tau)^2} - \frac{1}{1+((t-T)/\tau)^2}. \tag{4.36}$$

Indeed, so far we did not take into account, that ionization at the end of the pulse might be proportional to the length of the pulse T. We can see, that there is an energy $\tilde{E} \approx 0.28$ a.u., for which $E < \tilde{E}$ peaks start rapidly decaying. Then,

$$f_{\text{final}}(t) = \frac{1}{1+(t/\tau)^2} + \frac{1}{1+((t-T)/\tau)^2} e^{i2\pi T\tilde{E}/\hbar}. \tag{4.37}$$

Fig. 4.8 shows a good match between formula Eq. (4.37) and calculated results. Same applies for the bigger number of additional cycles N_T. The only disagreement is a presence of a zero energy peak $E = 0$ for the minima ($N_T = 20$). We attribute an absence of the the peak in the numerical results to the parity conservation, which cannot be described by the simple model of Eq. (4.37).

With Eq. (4.37) and Fig. 4.8, we are ready to explain oscillations of the ionization probability in dependence of the laser pulse duration. As we may see, an integral

$$\int_{-\infty}^{+\infty} |f(t)|^2 dt = \text{const} \tag{4.38}$$

does not depend on time. Hence, according to Parseval's theorem, neither does the total probability of ionization:

$$\int_{0}^{+\infty} |S(E)|^2 dE = \text{const}. \tag{4.39}$$

However, in our simple man model we do not take into account, that the laser field $\mathbf{A}(t)$ breaks the parity of the wave function. As a consequence, the spectrum in

Fig. 4.8 is nearly zero in a region around $E = 0$, in accordance to the PED threshold behavior [100]. In turn, the model predicts a peak at $E = 0$ for the duration of the pulses, which correspond to the minima of the ionization. Thus, we can remove the $E = 0$ peak in order to restore the parity of the resulting wave function. Of course, by doing this, we decrease the total probability $\int_0^{+\infty} |S(E)|^2 dE$. According to the Eq. (4.37), the zeroth peak appear every $\hbar/\tilde{E} \approx T_{\text{osc}}$, which coincide with the results of the simulation in Fig. 4.5. Additional straightforward explanation is that the PED modulation peaks move to higher energy with increasing pulse duration and decrease with an amplitude following the envelop. Indeed, for all the N_T, corresponding to minima, the first peak is always further, than for the N_T, corresponding to maxima, where it is always located at ≈ 0.22 a.u.

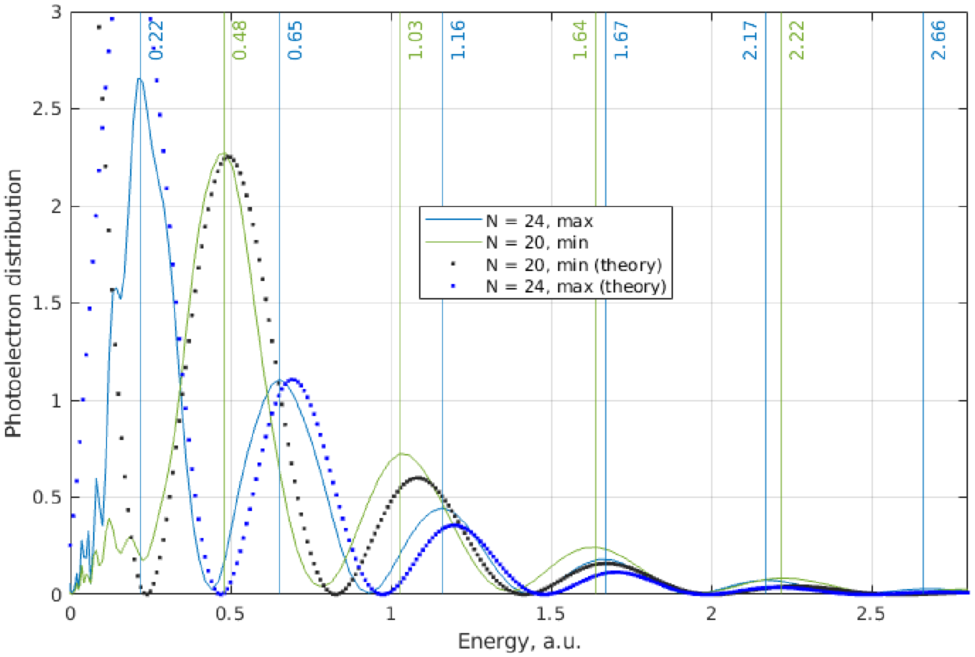

Figure 4.8: PED in dipole case, $a_0 \approx 0.13$, $EZ^{-3} = 30$ a.u., $\frac{e}{c}A_0 = 17.14$ a.u., $\omega = 14$ a.u. Corresponds to ionization probabilities from fig. 4.5. Dotted lines are obtained within the framework of a simple model Eq. (4.37).

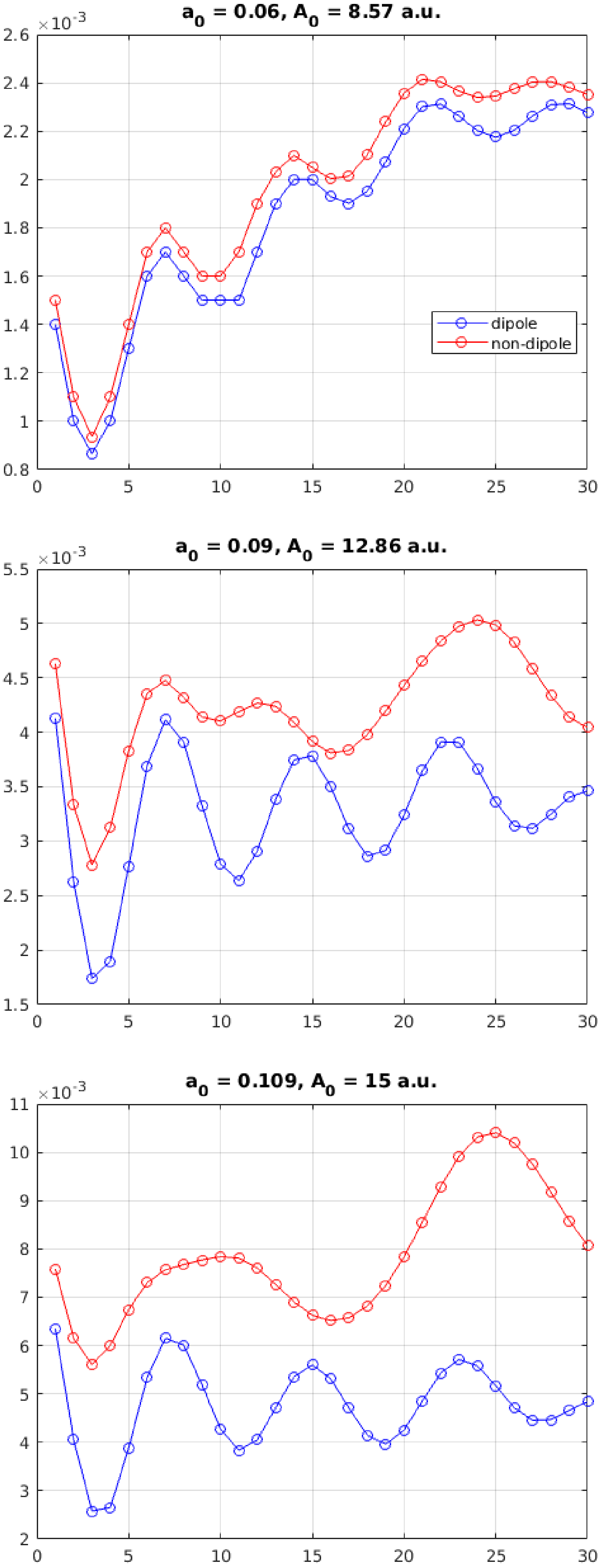

Figure 4.9: Ionization probabilities for dipole (blue) and nondipole (red) cases: (a) $a_0 = 0.06, \frac{e}{c}A_0 = 8.57$ a.u.; (b) $a_0 = 0.09, \frac{e}{c}A_0 = 12.86$ a.u.; (c) $a_0 = 0.11, \frac{e}{c}A_0 = 15$ a.u.

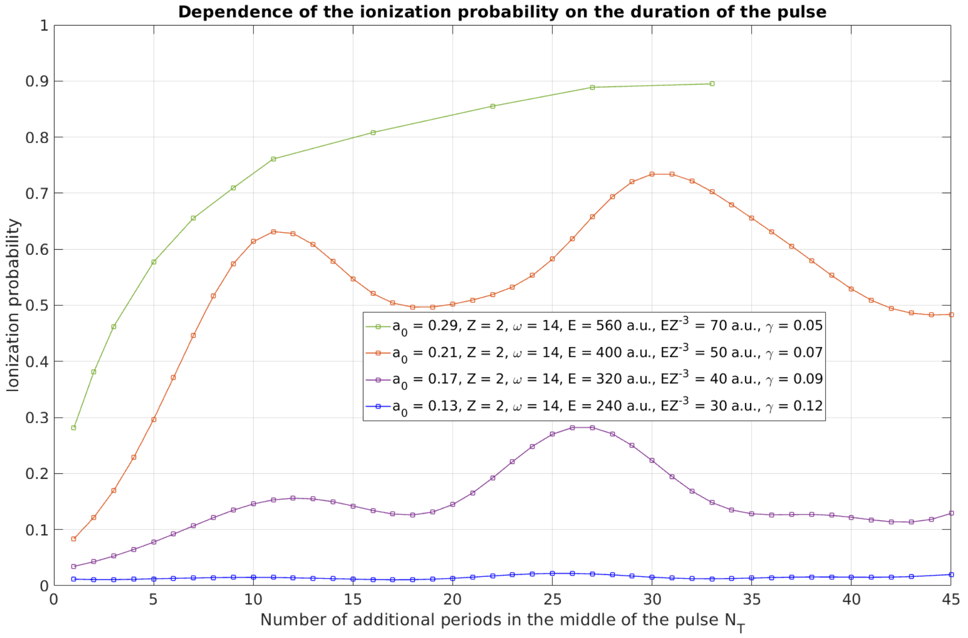

Figure 4.10: Ionization probability with respect to the duration of the pulse. Each line represent different a_0 parameter. The duration of the pulse is $T = N_T \cdot 2\pi/\omega + 6\tau$.

4.5 Nondipole case

4.5.1 Interplay between the nondipole drift and Coulomb force

Ionization probability oscillations in the dipole case are well described by the phenomenon of the dynamic interference. However, moving towards higher laser intensities $a_0 \gtrsim 0.1$, we observe, that nondipole effects start to play a crucial role. To begin with, we can compare ionization probabilities for the three different intensities (Fig. 4.9)

The parameter a_0 gradually increases from 0.06 to 0.11 by increasing the laser field strength E. For the lowest presented $a_0 = 0.06$, we see that ionization probabilities for the dipole and nondipole case follow the same pattern with the pulse duration and differ just by a constant. For the intermediate $a_0 = 0.09$, the plots are different by constant for the short laser pulses $N_T < 10$, but the deviation becomes non trivial for $N_T > 18$. As regards $a_0 = 0.11$, dipole and nondipole charts are completely different and follow different patterns.

Increasing the parameter a_0 even further up to 0.30, we observe (Fig. 4.10) a

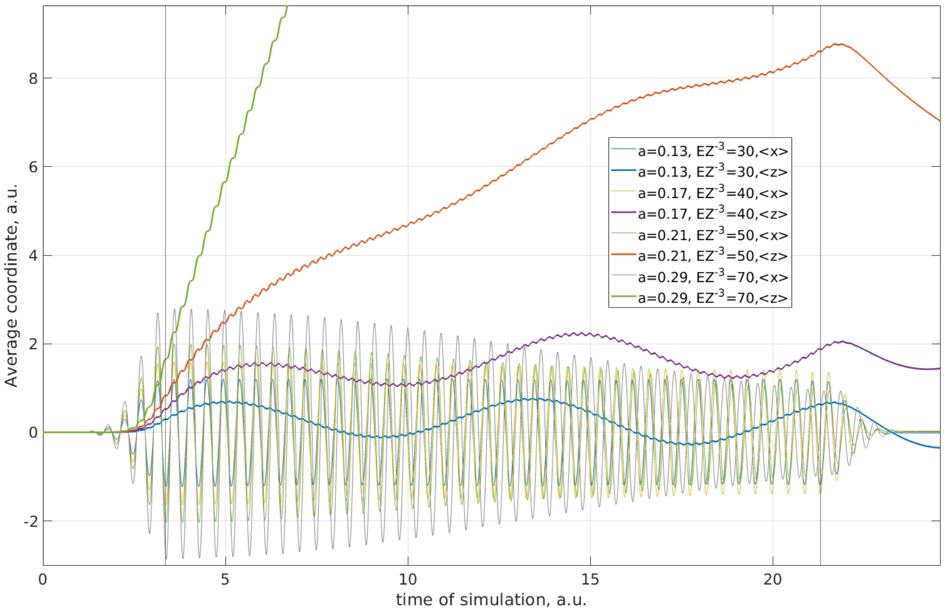

Figure 4.11: Trajectory of an electron during simulation. Different lines represent different a_0 values. The frequency is $\omega = 14$ a.u.

dramatic change of the ionization probability comparing to the dipole case. For the $a_0 = 0.13$ the curve is still similar to its dipole counterpart, although $a_0 = 0.17$ exhibits both oscillations and a smooth increase. That said, for $a_0 > \ 0.17$ ionization saturation is no longer present. The line $a_0 = 0.21$ is similar to $a_0 = 0.13$, but comes with a slightly different period of oscillations and roughly 3 times larger ionization probabilities. For the $a_0 = 0.29$, we see a change of the pattern again. There are no more large oscillations and the ionization almost gradually increases with the respect to the pulse duration.

We turn on the explanation of the differences of the pulse duration dependence of the dipole and nondipole ionization yield. We know that the main physical ingredient of the nondipole dynamics is the nondipole drift along the laser propagation direction induced by the magnetic field of the laser wave. The latter is a quasiclassical effect and can be characterized by the average coordinate $\langle z \rangle$ along the laser pulse propagation direction. The dependence of the pulse on the coordinate $\mathbf{A}(z,t)$ enables a new degree of freedom for the electron. The typical trajectories $\langle x(t) \rangle, \langle z(t) \rangle$ for the range $a_0 = 0.13 - 0.21$ are shown in Fig. 4.11. Regarding $\langle x(t) \rangle$ we can see, that the coordinate oscillates with an angular frequency ω and an anti-phase with respect to $\mathbf{A}(z,t)$. The main difference of $\langle x \rangle$ from the dipole regime becomes visible only for $a_0 > 0.17$, namely an amplitude of the oscillations starts gradually decreasing. This is a purely quantum nondipole effect, arising from the fact, that a quantum electron is not completely localized in space. Thus, different 'parts' of an electron are exposed to the different values $\mathbf{A}(z,t)$, which tend to decrease oscillations of an electron in space with time. For the $\langle z(t)\rangle$, the situation is less trivial. In case of an absence of the atomic potential, an electron would experience a drift in z direction with a speed $v_z(t) = e^2 A_x^2(t)/(2c)$. However, owing to the Coulombic potential the electron's dynamics varies. For example, in the case of $a_0 = 0.13$, the electron oscillates along z axis. This happens because the chosen A_0 value is not sufficient to overcome a Coulomb force. For the $a_0 = 0.17$ a drift component is more apparent, although the trajectory $\langle z(t)\rangle$ still has local minima and maxima with a frequency much smaller than ω. As for the $a_0 = 0.21$, the drift component starts to dominate.

The periodic oscillation of the expectation value of $\langle z(t)\rangle$ for the electron wave packet during the interaction results in oscillation of $\langle z(t)\rangle$ at the switching off the laser field. One could expect that in the stabilization regime when the main ionization takes place at the switching on and off the laser pulse, the final coordinate oscillation will yeld different probability of capturing electron by the atomic field, and will result in the oscillation of the ionization yield. We analyze this point in Fig. 4.12. It turns out, that the value of $\langle z\rangle$ after the end of the pulse might serve as a criterion only for small parameters $a_0 \sim 0.1$. In Fig. 4.12 we can see that the maximum $\langle z\rangle$ correspond to the maximum ionization yield for $a_0 = 0.09$ and $a_0 = 0.11$. On the other hand, we see that for larger $a_0 = 0.21$ the trajectory is dominated by the drift (Fig. 4.11), although the ionization probability in Fig. 4.10 still oscillates with the pulse duration. A better understanding of the ionization in nondipole regime can be found after the analysis of the spectrum.

The PED in the nondipole case is different from the nondipole one. The PED for $a_0 = 0.11$ is presented in Fig. 4.13. The PED in the nondipole ionization case is not explained by the simple model of dynamic interference. By contrast, the nondipole PED is dominated by a single low energy broad distribution, with a width determined by the switching on time of the laser pulse τ: $\Delta E \sim 1/\tau$. As there is no interference in PED corresponding to the pulse duration, we can deduce that the dipole picture of ionization assuming that the ionization emerges mostly at the switching on and off of the laser pulse is not valid in the nondipole regime. This is understandable because the final position of the ionization wave packet is quite far from the core and this point is not distinguished point for the creation of the continuum ionization wave packet. Rather, in the nondipole case the ionization wave packet first created at the switching

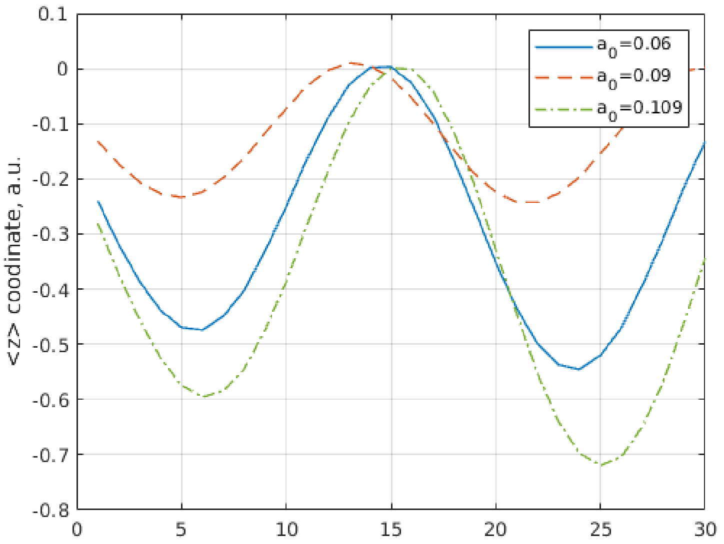

Figure 4.12: Final position $\langle z \rangle$ of an electron after the end of the pulse as a function of number of additional periods N_T in the laser pulse.

on of the laser pulse and afterward it is replenished during all interaction time. This conclusion can drawn from the results of Ref. [94].

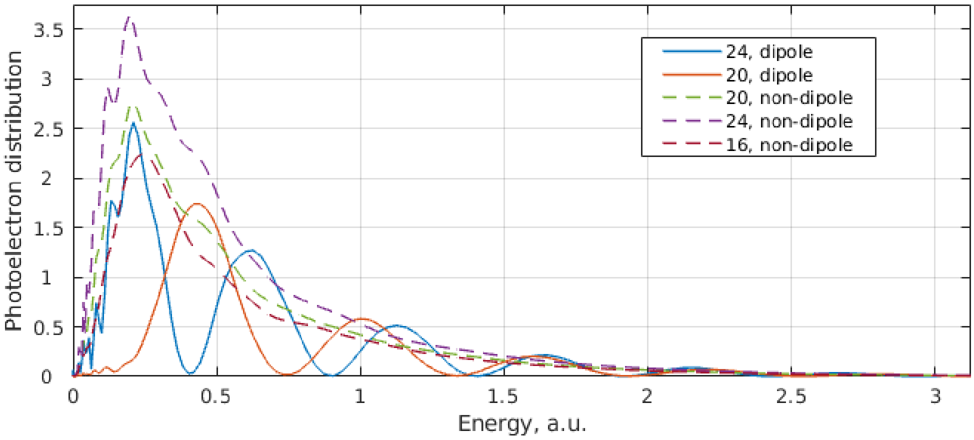

Figure 4.13: PED in the nondipole case; $a_0 = 0.11$, $\frac{e}{c}A_0 = 15$ a.u.. The dipole PEDs are shown by solid lines, the nondipole by the dashed ones.

In [94] authors noticed that although the drift velocity in the case of a free electron $v_z(t)$ is along the laser propagation direction, the ionized electron is usually ejected into the opposite negative $-\hat{\mathbf{z}}$ direction. This counterintuitive behavior is claimed to be a result of the interplay between the electromagnetic and Coulomb forces. Due to the drift electron spend more time during the interaction at $z > 0$ and get the momentum transfer from the Coulomb field in the opposite direction. Moreover, via classical

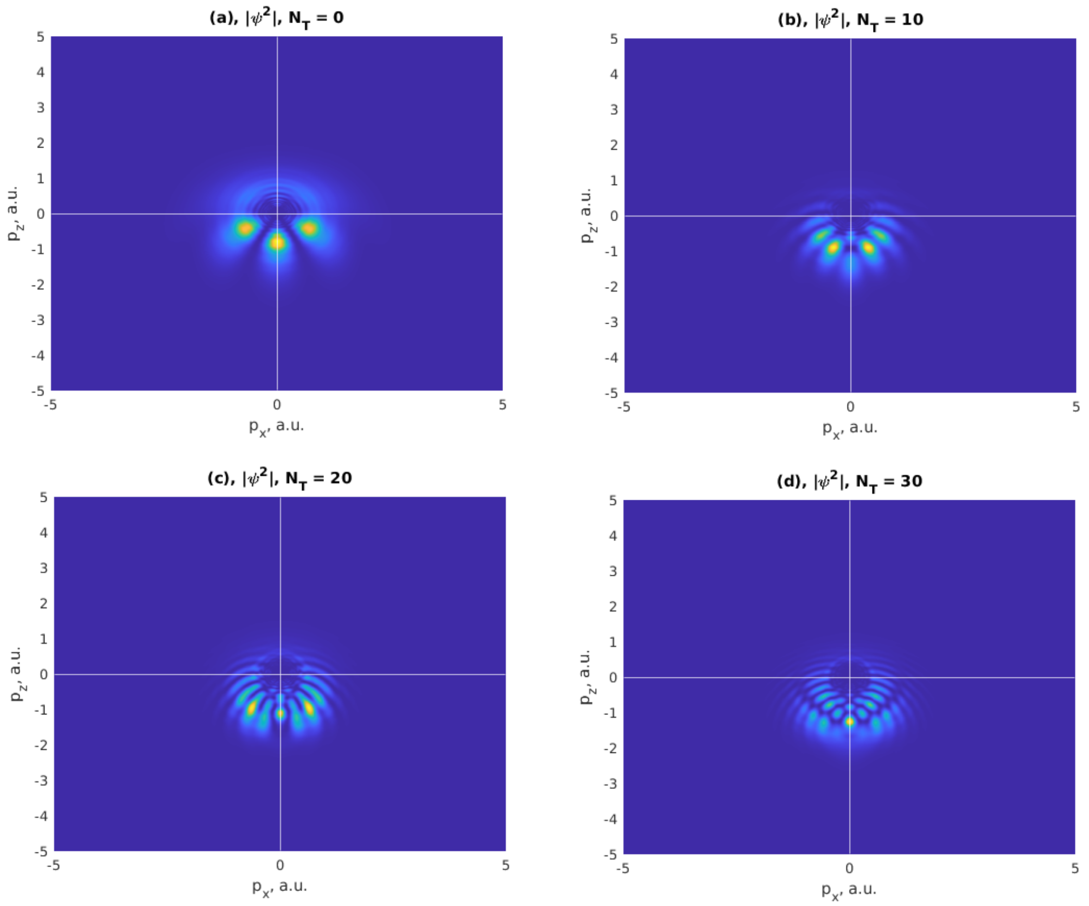

Figure 4.14: Distributions of $|\hat{\psi}(p_x, p_z)|^2$ for different durations of the pulse ($N_T = 0, 10, 20, 30$ periods). The parameters are: $a_0 = 0.21$, $EZ^{-3} = 50$ a.u., $\frac{e}{c}A_0 = 28.57$ a.u., $\omega = 14$ a.u. Corresponds to the red line in Fig.4.10 and Fig.4.11.

Monte Carlo trajectory analysis they concluded that the trajectories of ionized electrons which contribute to the anomalous nondipole lobe of the angular distribution (opposite to the laser propagation direction) will be captured in the case of the dipole interaction. This means that the asymmetric Coulomb interaction in the nondipole case leads to additional ionization, creating electrons with anomalous angular distribution.

In our case of $a_0 = 0.21$, an electron is also ejected into the $-z$ direction for different pulse durations, see Fig. 4.14. In turn, the final position of an electron right after the interaction gradually increases in $+z$ direction (Fig. 4.11). Thus, we assume that an ionization along z axis is mostly related to the Coulomb momentum kick which is acquired by an electron during the interaction. In order to verify this assumption, we estimate from our simulation the total Coulomb momentum transfer to the electron wave packet during the interaction:

$$\langle \mathbf{p}^C(t)\rangle = -\int_{-\infty}^{t} dt \langle \boldsymbol{\nabla} V(r)\rangle, \tag{4.40}$$

with the expectation value of the Coulomb force $\langle -\boldsymbol{\nabla} V(r)\rangle$. The evolution of the Coulomb induced momentum $\langle p_z^C(t)\rangle$ with time is depicted in Fig. 4.15(a). The final value of $\langle p_z^C\rangle$ together with the ionization probability is shown in Fig. 4.15(b). Moreover, if we take a look at the spectrum Fig. 4.14, we see, that the main contribution comes from p_z, corresponding to quasiclassical calculations of $\langle p_z^C\rangle$.

One more argument for the Coulomb kick importance is the fact, that the Coulomb kick is correlated with the slowing down of the electron motion in $\mathbf{z}$ (Fig. 4.16). Indeed, although the velocity $\langle v_z\rangle$ remains positive during the simulation because of the drift, it also oscillates, which correspond to the kicks in Fig. 4.15(a).

All the mentioned above confirms the conclusion, that nondipole ionization oscillations are mostly determined and governed by the Coulomb momentum kicks, which ionize an electron in the direction opposite to the main drift during the pulse duration.

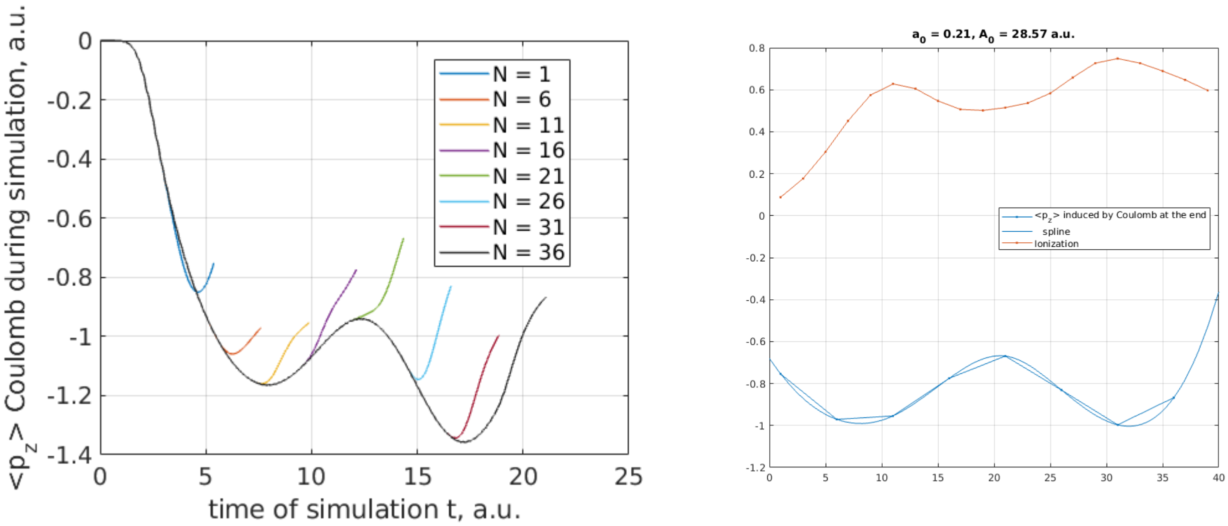

Figure 4.15: (a) Average momentum $\langle p_z(t)\rangle$, induced by coulomb force, with respect to the time of simulation t and a durations of the pulse; (b) A value of the average Coulomb induced momentum $\langle p_z\rangle$ after the end of the pulse together with the respective ionization probability. The parameters are: $a_0 = 0.21,\ EZ^{-3} = 50$ a.u., $\frac{e}{c}A_0 = 28.57$ a.u., $\omega = 14$ a.u.

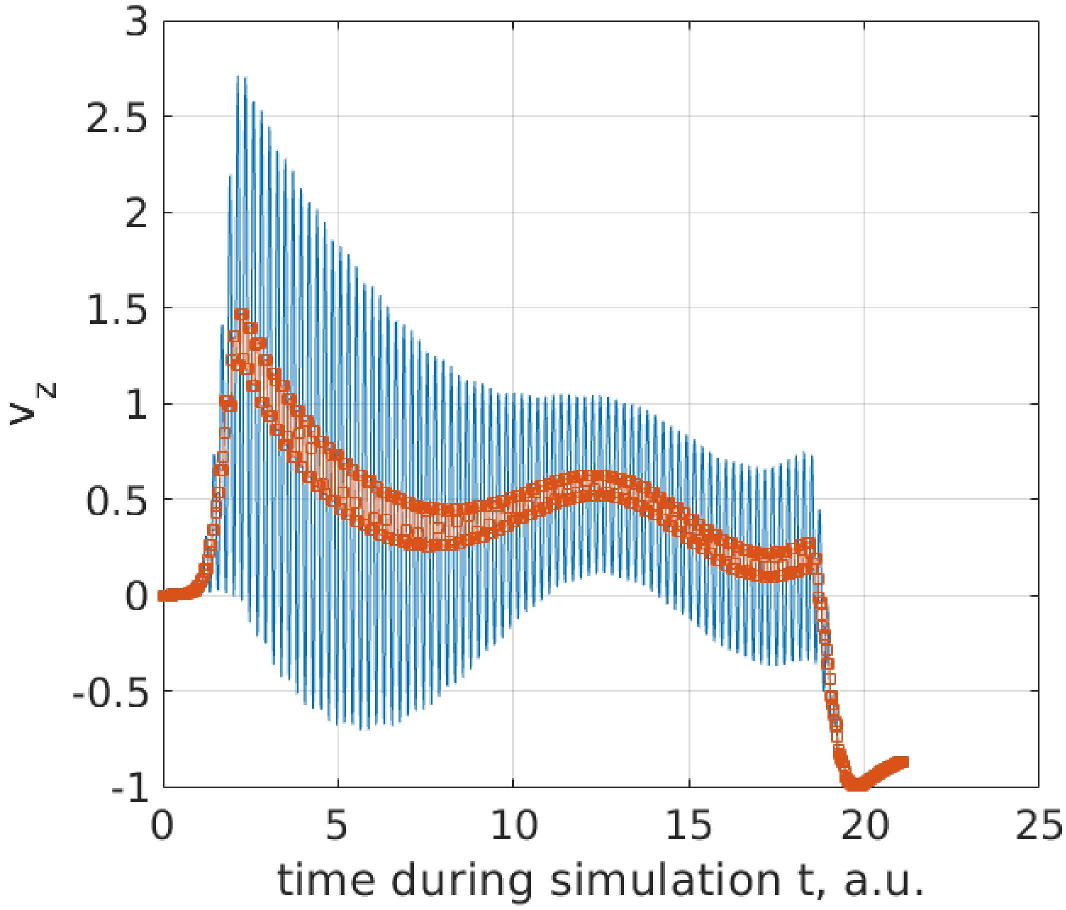

Figure 4.16: An average velocity $\langle v_z(t)\rangle$ of an electron as a function of time. Blue line is a calculated $\langle v_z(t)\rangle$, the red line is an everaged $\langle v_z(t)\rangle$ over the period $2\pi/\omega$ of the fast oscillations. The parameters are: $a_0 = 0.21$, $EZ^{-3} = 50$ a.u., $\frac{e}{c}A_0 = 28.57$ a.u., $\omega = 14$ a.u.

4.5.2 Angular distribution

Another interesting question is the photoelectron angular distribution (PAD). The PAD in the dipole case is relatively simple and depicted in Fig. 4.17. In this regime, an electron is ejected evenly both in $\mathbf{x}$ and $-\mathbf{x}$ directions and also symmetrical along $\mathbf{z}$ axis. For the small non zero parameter $a_0 = 0.11$ and rather short pulse duration ($N_T = 16$) we see, that the spectrum is slightly deformed. However, we can already spot a new third lobe, which is aimed right into the $-\mathbf{z}$ direction. For the longer pulses, two initial lobes tend to bend into the $-\mathbf{z}$ direction and a third lobe keeps growing.

For the stronger pulse $a_0 = 0.21$ in Fig. 4.18 the difference with the dipole case is even more noticeable. Just as in Fig. 4.10, the ionization is now dominated by the nondipole effects. All the lobes are directed into $-\mathbf{z}$ direction. However, all the normal lobes, apparently originating from the interaction of the fast moving along the $\mathbf{x}$ axis, are only bended in $-\mathbf{z}$, keeping a certain $-\mathbf{x}$. In turn, an anomalous lobe is directed right to the $-\mathbf{z}$ direction and represent the Coulomb kick. The lobe oscillates together with the total ionization, at least for the adjacent minima and maxima. That reads, that the length of the lobe is not necessarily proportional to the ionization probability for the certain N, but it reflects the derivative of the total ionization probability function.

For the strongest observed pulse $a_0 = 0.29$, Fig. 4.19, the lobes become more narrow. Since the total ionization probability no longer oscillates in this case (it least for the N concerned), but gradually rises, so does the main lobe. With time, other lobes tend to bend closer to the anomalous lobe.

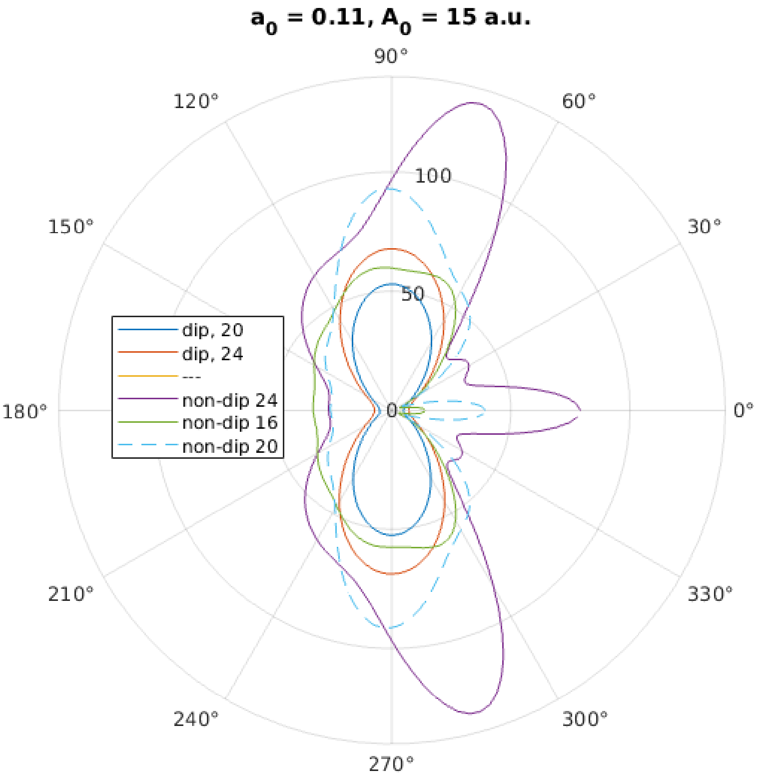

Figure 4.17: Angular spectrum for $a_0 = 0.11$, $\frac{e}{c}A_0 = 15$ a.u. Numbers denote number of the additional cycles N_T. The direction 0^o corresponds to the $-\hat{\mathbf{z}}$ direction.

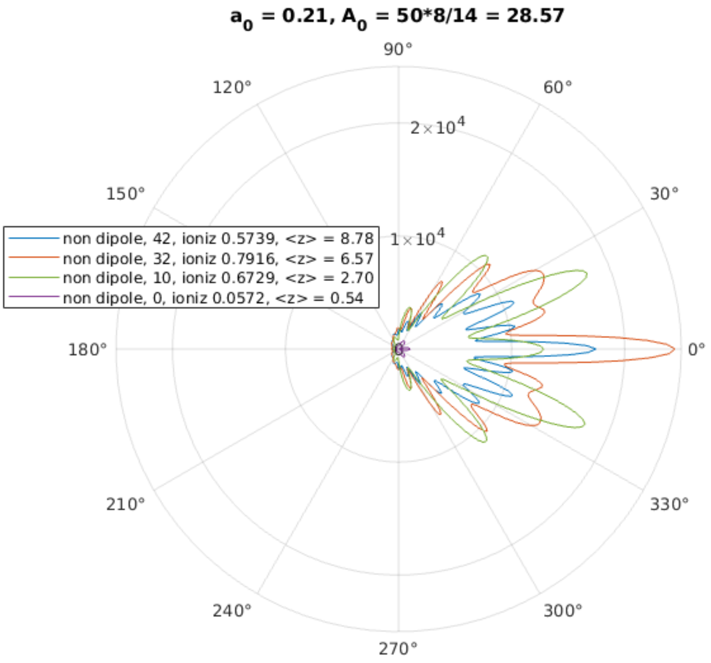

Figure 4.18: Angular spectrum for $a_0 = 0.17$, $\frac{e}{c}A_0 = 28.57$ a.u., $EZ^{-3} = 59$ a.u. Numbers denote number of the additional cycles N_T. The direction 0^o corresponds to the $-\hat{\mathbf{z}}$ direction.

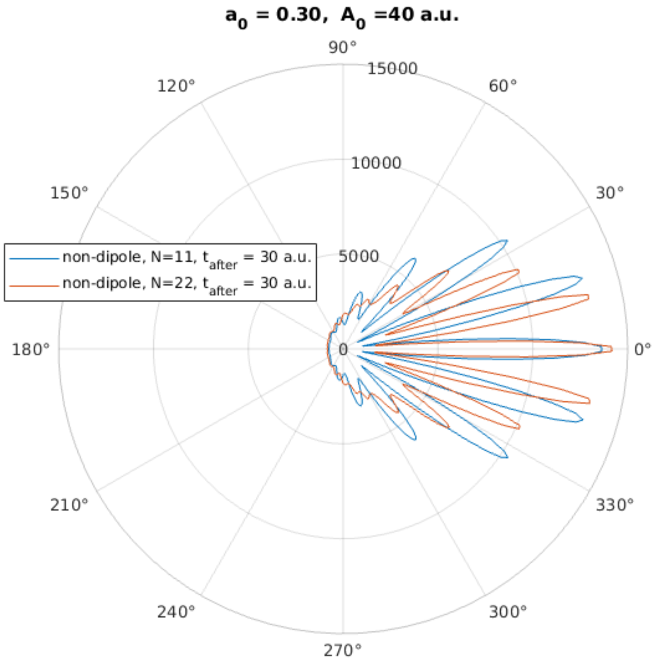

Figure 4.19: Angular spectrum for $a_0 = 0.29$, $\frac{e}{c}A_0 = 40$ a.u., $EZ^{-3} = 70$ a.u. Numbers denote number of the additional cycles N_T. The direction 0^o corresponds to the $-\hat{\mathbf{z}}$ direction.

4.5.3 Electron wave packet oscillation in the laser propagation direction

In this section we analyze the electron wave packet oscillation in the laser propagation direction z, which yields in the dipole case to the final $\langle z\rangle$ oscillation and in the nondipole case to the $\langle p_z^C\rangle$ oscillation, and explain the ionization yield oscillatory dependence on the laser pulse duration.

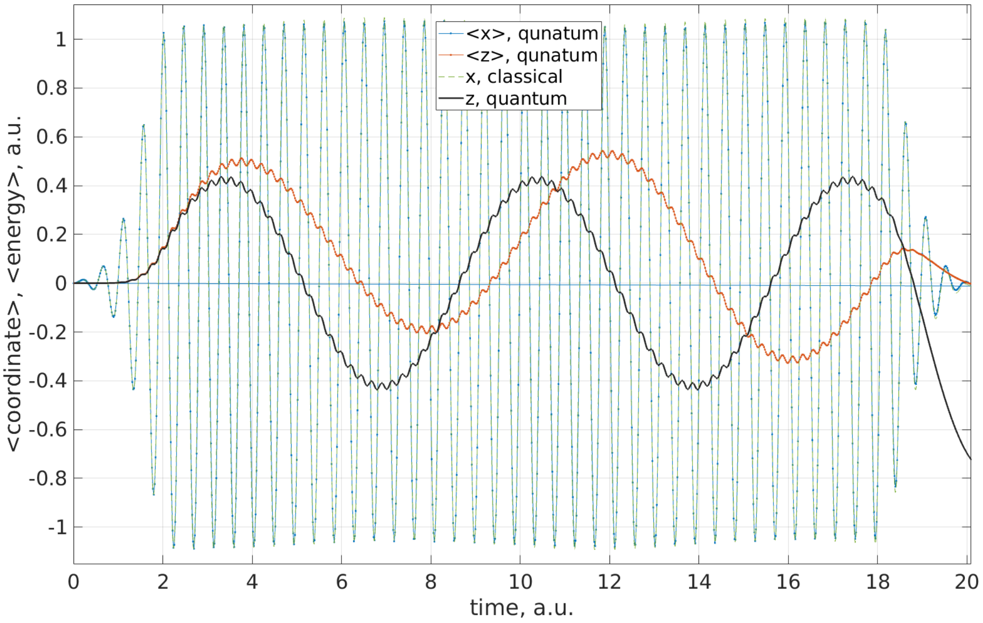

Figure 4.20: A comparison of trajectories from 2D classical and 2D quantum simulations. Parameters are $a_0 = 0.11,\ \omega = 14$ a.u., $\frac{e}{c}A_0 = 15$ a.u.

In order to quantitatively describe the difference in ionization probabilities for the dipole and nondipole cases for $a_0 \approx 0.1$, we introduce a simple classical single electron model, which effectively describe the ionization wave packet dynamics driven by the laser field in the Coulomb field of the atomic core. To begin, we need to take into account the quantum nature of an electron. For this purpose, we introduce an effective atomic potential by means of smoothing the original soft-Coulomb atomic potential with an original ground state as

$$V_{\text{eff}}(\mathbf{r}) = \int_0^\infty V(\mathbf{r}')|\psi(\mathbf{r}-\mathbf{r}')|^2 d\mathbf{r}'. \tag{4.41}$$

In our model the effective classical electron moves in the effective potential $V_{\text{eff}}(\mathbf{r})$ driven by the laser field. The effective electron in $V_{\text{eff}}(0) = -2.5$ a.u. has the same potential energy, as a quantum one. Using V_{eff} as a potential, we launch a simple classical 2D simulation [102] with an original vector potential $A(z,t)$ and initial electron parameters $\mathbf{q} = 0$, $\mathbf{p} = 0$. The result is depicted for $a_0 = 0.11$a.u. in Fig. 4.20. The trajectory $\langle x(t)\rangle$ and $x(t)$ nearly coincide in quantum and classical cases. Indeed, as was mentioned earlier, for $a_0 \sim 0.1$ nondipole effects do not influence the quiver motion of an electron along the x axis. In the absence of central potential and $A \neq A(z)$ the motion of a classical electron is governed by the formula

$$\alpha(t) = \frac{e}{mc}\int_0^t A(t')dt' = \frac{E(t)}{\omega^2}, \tag{4.42}$$

and in our case $|\alpha_{\max}| = 1.07$ a.u., which is in the perfect agreement with Fig. 4.20. As for the $\langle z(t)\rangle$, the nondipole interaction plays a more important role. For instance, one can notice, that the quantum trajectory is slightly not symmetrical with respect to zero. However, such an effect cannot be resolved within the framework of the classical simulation. Never the less, the point-like particle still reflects the leading order of nondipole correction to the trajectory. This yields oscillations of $\langle z(t)\rangle$ with a frequency, which is only 20% smaller, than a quantum one.

For a test of our simple effective model, we analyze the time dependence of the energy comparing TDSE results with the model in Figs. 4.21. Average potential energy $\langle V(t)\rangle$ for quantum case and $V(t)$ are close to each other and both oscillate slightly below -2 a.u. value. The total energies are different by the value of 0.5 a.u., which corresponds to the initial kinetic energy of a quantum electron. As can be seen from Fig. 4.22, the total kinetic energy of an electron oscillates around 0.5 a.u. throughout the simulation. In order to incorporate this energy component into the classical simulation, one could introduce a Bohr orbit and respective initial position $\mathbf{q}_0$ and momentum $\mathbf{p}_0$. However, this would bring antisymmetry to the initial conditions of the problem and would require averaging over many initial $\mathbf{q}_0$ and $\mathbf{p}_0$, which contradicts with the idea of a simple one-particle classical model.

As was shown in Fig. 4.15, the total ionization is correlated with the Coulomb kick in the nondipole case. Our simple 2D classical model captures the Coulomb kick, too. As one can see in Fig. 4.24, the $\langle p_z\rangle_C$ are very similar. Regarding the amplitude, the deviation is no more than 20%. The point of the minimum of $\langle p_z\rangle_C$ is also slightly shifted, which is explained by the fact, that the frequency of the oscillations in the classical case is by 20% bigger, than in the quantum one.

Returning to the idea of a simple quasiclassical model of the nondipole ionization, it is possible to simplify it even further. The fact, that the motion along x axis is nearly described by Eq. (4.42) even in quantum case, suggests that it is possible to remove

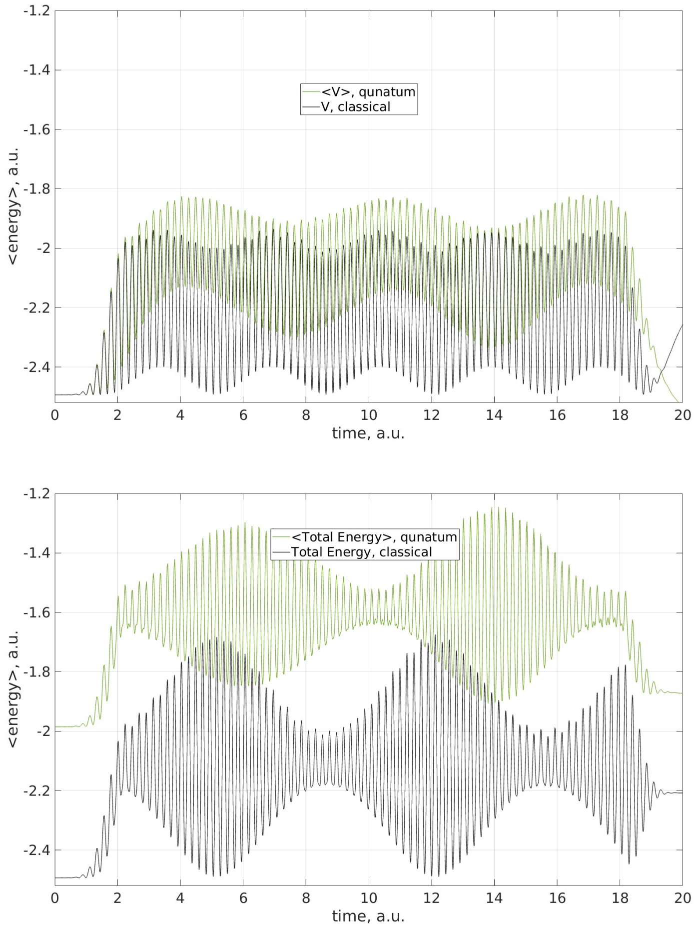

Figure 4.21: (a) A comparison of total energies in a quantum simulation and 2D model simulation; (b) A comparison of potential energies in a quantum simulation and 2D model simulation.

x dimension completely. It can be done by moving into the Kramers-Henneberger frame, specifically by averaging the potential over the oscillation period $2\pi/\omega$

$$V_{\text{eff}}(z) = \int_0^{2\pi/\omega} V(A_0 \sin(\omega t), z) dt. \tag{4.43}$$

Averaging of the kinetic term over the period yields just a free particle term. As a result, we receive a 1D system, which does not explicitly depend on vector potential $\mathbf{A}(z,t)$. The oscillations along z axis can be incorporated via initial conditions. For example, one can take an averaged over the period value of $p_z^2/2$ from the classical 2D simulation (Fig. 4.23). Then, the initial conditions are

$$q_0 = 0,\ p_0 = \langle |p_z| \rangle = 0.55 \text{ a.u.} \tag{4.44}$$

The trajectory obtained via such a 1D simulation is depicted in Fig. 4.23.

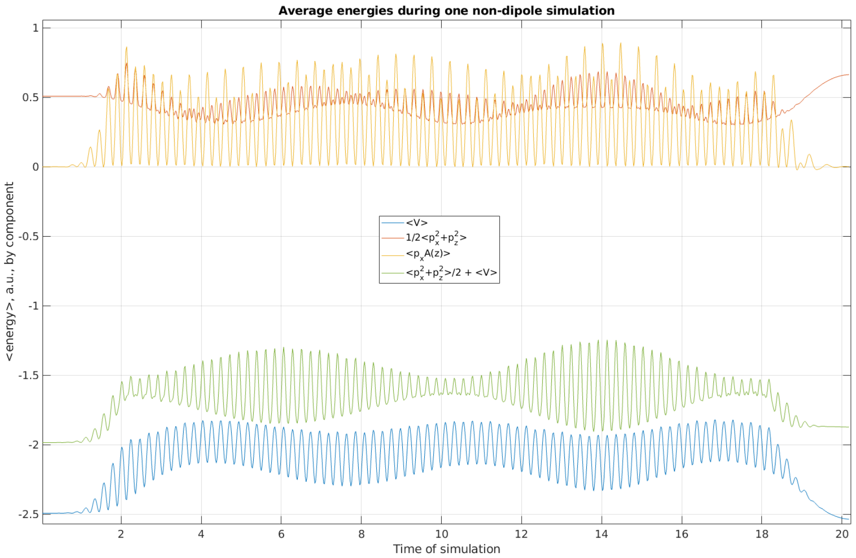

Figure 4.22: Average electron energies with the respect to the simulation time. Quantum simulation, $a_0 = 0.11,\ \omega = 14$ a.u., $\frac{e}{c}A_0 = 15$ a.u.

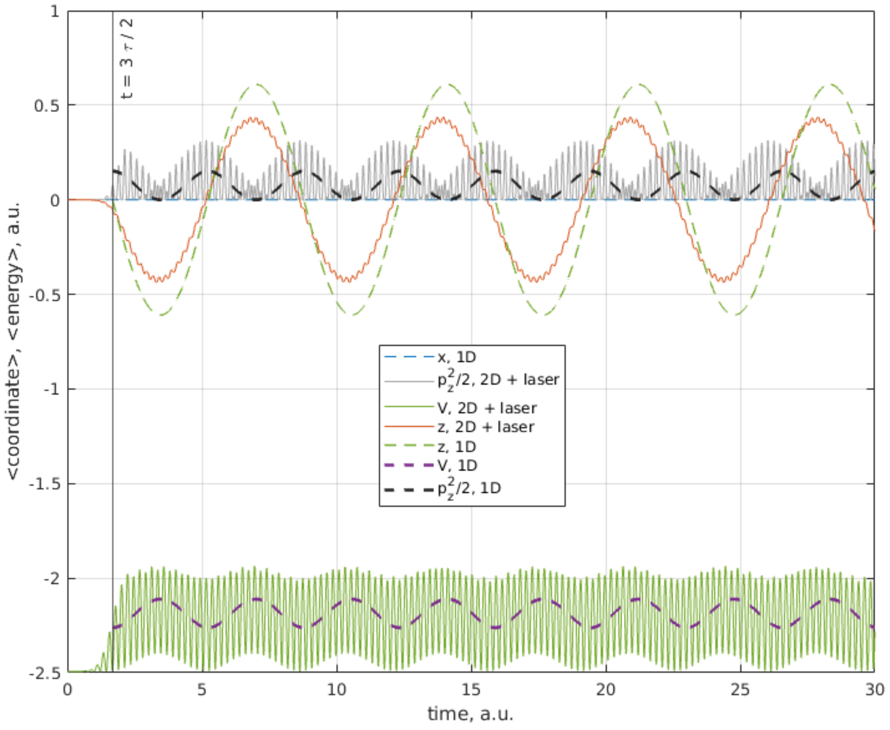

Figure 4.23: A comparison of trajectories and energies from 2D classical and 1D classical simulations. The lines for the 1D case are shifted by τ, which is a laser turn on value. The parameters are: $a_0 = 0.11,\ \omega = 14$ a.u., $\frac{e}{c}A_0 = 15$ a.u.

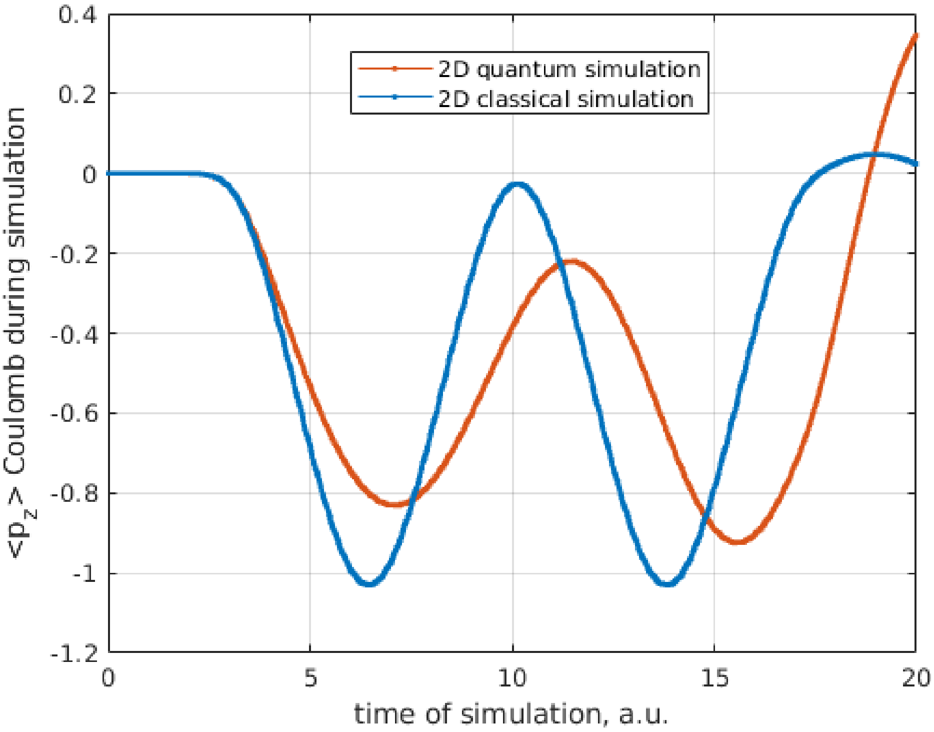

Figure 4.24: The parameters are: $a_0 = 0.13$, $\omega = 14$ a.u., $EZ^{-3} = 30$ a.u.

Chapter 5

Conclusion

In this thesis, a method for the numerical solution of time-dependent Dirac equation is developed for the aim of treating the strong field ionization in the relativistic regimes. Our method is based on the coordinates scaling ansazt that absorbs as well the kinetic propagation phase of the wave function. The method is tested and analyzed on a simple 1D example of relativistic ionization. As an application of the method, we solve numerically 2D problem of the strong field ionization of light hydrogen-like atoms in a high-frequency strong laser field. We have found a new effect that the ionization probabilities in the stabilization regime oscillate with the laser pulse duration. While this effect exists as in the dipole regime as well in the nondipole one, the features of the yield oscillation as well as the underlying physical mechanism are quite different.

Regarding the particular results, in the Chapter 3, the coordinate scaling method for the numerical treatment of the atomic ionization problem in relativistically strong laser fields was developed. There, the scheme of the relativistic generalization and the study of its performance was carried out for the case of the 1D ionization problem. The relativistic problem requires the application of an additional Foldy-Wouthuysen transformation along with the scaling method to avoid fast oscillation of the wave function due to the virtual transitions to negative energies. To do that, the quasiclassical approximation method, recently developed by Silenko, was invoked, in contrast to the more common v/c-approximation used in textbooks. The accuracy of the results of the scaling method was proved in the 3rd chapter on a concrete example in the main region of the wave function. The sources of the inaccuracy on the tails of the wave function were analyzed. The computational advantage of the relativistic scaling method over the standard numerical TDDE [25] solution were also demonstrated.

In Chapter 4, the method was used to investigate an ionization process of the 2D light atoms, exposed to the relativistically strong laser fields. The study revealed, that the ionization probabilities depend on the exposure time. Moreover, the dependence is different for the dipole and non dipole regimes, because there are two different mechanisms, responsible for the effect. In the dipole case, the oscillations can be explained by means of the dynamic interference theory. I the non dipole one, the ionization dominates by the electron drift and its subsequent Coulomb kick.

Also, Chapter 4 brings some insights on how the respective phenomena can be observed experimentally. It was shown, that oscillating ionization impacts both radial and angular photoelectron spectrum. As of radial spectrum, the ionization peaks in the dipole case move as the laser duration increases. In the nondipole case, the peaks merge and correspond to the energy of the respective Coulomb kick. An angular spectrum also exhibits different behavior for the dipole and non dipole cases. It was shown, that in the non dipole case the lobes tend to bend towards the opposite to the drift direction. Also, the main lube, which has a pure nondipole origin, oscillates in magnitude together with the total ionization probability.

For the outline, a few possible directions of the further research can be pointed out. From the computational perspective, a question ”How to efficiently act with a pseudo-differential operator, such as a square root, onto a wave function?” still remains open. Particularly, an Algorithm 2 can serve as a starting point for the new research. Regarding the physics studied, one could investigate the systems, in which spin effects become non negligible. The scaling coordinates approach, in principle, provides a possibility for such a research. Also, Fig.4.14 depicts an interference of the wavepacket, which evolves with the duration of the pulse. Describing an origin of this phenomenon and its main properties is an interesting task to be accomplished in the future.

Appendix A

A.1 Appendix A

Dirac equation in 3D reads

$$i\hbar\dot{\psi} = \left[\beta mc^2 + c\sum_{n=1}^{3}\alpha_n\left(p_n - \frac{e}{c}A_n(\boldsymbol{x},t)\right) + V(\boldsymbol{x})\right]\psi \tag{A.1}$$

where β and $\alpha_{1,2,3}$ are Dirac matrices. FW Hamiltonian with terms up to $\hbar^2$ [59]

$$\begin{gathered}H_{FW} = \beta\varepsilon + V(\boldsymbol{x}) + H_{SO,DW} + \mathcal{O}\left(\lambda^2\right), \text{where} \\ \varepsilon = mc^2\sqrt{1 + \frac{\left(\boldsymbol{p} - \frac{e}{c}A(\boldsymbol{x},t)\right)^2}{m^2c^2} - \frac{e\hbar}{m^2c^3}\boldsymbol{\sigma}\cdot\boldsymbol{B}}\,, \quad H_{SO,DW} = \frac{\hbar^2}{8}\left\{\frac{1}{\varepsilon(\varepsilon+mc^2)}, [O,[O,F]]\right\}. \\ F = V - i\hbar\frac{\partial}{\partial t}, \quad O = c\sum_{n=1}^{3}\alpha_n\left(p_n - \frac{e}{c}A_n(\boldsymbol{x},t)\right)\end{gathered} \tag{A.2}$$

In order to show that additional $\hbar^2$-order terms are negligible in case of relativistic ionization problem with laser frequency $\hbar\omega \ll mc^2$ and $Z\alpha < 1$, we analyze leftover terms from Ref. [59]. We introduce a dimensionless field parameter: $a_0 = eA_0/(mc^2) \sim p/(mc)$ with the laser vector potential

$$\boldsymbol{A} = A_0 \sin\left[\omega\left(t - \frac{\boldsymbol{x}}{c}\right)\right]. \tag{A.3}$$

The equation (A.2) is obtained in the quasiclassical limit applying $\hbar$-expansion [59] and it is valid without restriction of the field value. However, for the sake of error analysis and comparison with the common v/c-expansion results [71], let us following Ref. [59], consider the weak-limit. In this limit, Eq. (A.2) yields the known Hamiltonian with relativistic corrections [71]:

$$H_{FW} = \left[mc^2 + \frac{1}{2m}\left(\boldsymbol{p} - \frac{e}{c}A(\boldsymbol{x},t)\right)^2 - \frac{p^4}{8m^3c^2}\right] + V + H_S + H_{SO} + H_{DW}. \tag{A.4}$$

Let us estimate the magnitude of spin and spin-orbital terms:

$$
\begin{aligned}
H_S &= -\frac{e\hbar}{2mc}\boldsymbol{\sigma}\cdot\boldsymbol{B} \sim \frac{\hbar\omega}{2}a_0 && \text{(A.5)}\\
H_{SO} &= H_{SOI} + H_{SOII} = -i\frac{e\lambda^2}{8}\boldsymbol{\sigma}\cdot\nabla\times\boldsymbol{E} + i\frac{e\lambda^2}{4}\boldsymbol{\sigma}\cdot\boldsymbol{E}\times\nabla && \text{(A.6)}\\
H_{SOI} &= i\frac{e\hbar^2}{8m^2c^2}\frac{1}{c}\boldsymbol{\sigma}\dot{\boldsymbol{B}} \sim \frac{e\hbar^2}{8m^2c^2}\frac{\omega^2}{c^2}A = \frac{\hbar^2\omega^2}{mc^2}a_0 && \text{(A.7)}\\
H_{SOII} &= \frac{e\hbar}{4m^2c^2}\boldsymbol{\sigma}(\nabla V)\times\boldsymbol{p} + \frac{e\hbar}{4m^2c^3}\boldsymbol{\sigma}\cdot\dot{\boldsymbol{A}}\times\boldsymbol{p} \sim \frac{\lambda}{4}(\nabla V)a_0 + \frac{\hbar\omega}{4}a_0^2 && \text{(A.8)}\\
H_{DW} &= \frac{\lambda^2}{8}\Delta V && \text{(A.9)}
\end{aligned}
$$

Second, we estimate leftover terms in Eqs. (16)-(17) from Ref. [59], which are written in a weak-field limit in stationary case. Restricting ourselves to the 1D case, the operators ε and O from [59] become

$$O = c(p_x - \frac{e}{c}A(x)), \quad \varepsilon = V(x) \tag{A.10}$$

Defining also the terms of Eq. (16) in Ref. [59] via their denominators, we obtain

$$H_{512} \sim \lambda^2 eV'' \left[a_0^2 + \mathcal{O}\left(a_0^4\right)\right] + \mathcal{O}\left(\lambda^3\right) \tag{A.11}$$

Apparently, the term H_{512} plays a role of relativistic corrections to Darwin term in terms of parameter a_0. The next two terms, which have not been calculated explicitly in [59], are

$$H_{16} \sim \frac{\lambda^2}{mc^2}e^2V'^2 + \mathcal{O}\left(\lambda^3\right), \quad H_{256} \sim \frac{\lambda^2}{mc^2}e^2V'^2a_0^2 + \mathcal{O}\left(\lambda^3\right). \tag{A.12}$$

The terms in the latter $\propto \lambda^2$, have an additional small factor $eV/(mc^2)$ compared to H_{DW} of Eq. (A.9) and H_{512}. Thus, we conclude that Ref. [59] provides analytical expressions for the all relevant terms in the order of λ^2.

A.2 Appendix B

Let us introduce a "shifted phase derivative" function

$$b = \varphi' - \frac{e}{c\hbar}A \tag{A.13}$$

Then the respective formulae for Eq. (3.20) become

$$T_0(x,t) \approx e^{i\varphi}\sqrt{1+\lambda^2b^2}\left[1 - \frac{i}{2}\lambda^2\varphi''\left[1+\lambda^2b^2\right]^{-2}\right] + \mathcal{O}\left(\frac{\lambda^2}{\lambda_l^2}\right) \tag{A.14}$$

$$T_1(x,t) \approx e^{i\varphi}\frac{b}{\sqrt{1+\lambda^2b^2}}\left[1 + 3\frac{i}{2}\lambda^2\varphi''\left[1+\lambda^2b^2\right]^{-2}\right] + \mathcal{O}\left(\frac{\lambda^2}{\lambda_l^2}\right) \tag{A.15}$$

$$T_2(x,t) \approx e^{i\varphi} \frac{1}{\left[1+\lambda^2 b^2\right]^{3/2}} \left[1 + 3\frac{i}{2}\lambda^2 \varphi'' \left[1-4b^2\right] \left[1+\lambda^2 b^2\right]^{-2}\right] + \mathcal{O}\left(\frac{\lambda^2}{\lambda_l^2}\right) \tag{A.16}$$

In 2D, the supplementary expressions for the Eq. (4.8) and Eq. (4.9) read

$$b_x = \varphi'_x - \frac{e}{c\hbar}A, \; b_z = \varphi'_z \tag{A.17}$$

$$T_0(x,z,t) \approx e^{i\varphi}\sqrt{1+\lambda^2 b_x^2 + \lambda^2 b_z^2}\left[1 - \frac{i}{2}\lambda^2 \frac{(\varphi''_{xx} M_{0xx} + 2\varphi''_{xz} M_{0xz} + \varphi''_{zz} M_{0zz})}{(1+\lambda^2 b_x^2 + \lambda^2 b_z^2)^2}\right] + \mathcal{O}\left(\frac{\lambda^2}{\lambda_l^2}\right) \tag{A.18}$$

where

$$M_{0xx} = 1+\lambda^2 b_z^2, \quad M_{0zz} = 1+\lambda^2 b_x^2, \quad M_{0xz} = \lambda^2 b_x b_z \tag{A.19}$$

$$\begin{aligned}
T_{1,x}(x,z,t) &\approx e^{i\varphi}\frac{1}{\sqrt{1+\lambda^2 b_x^2+\lambda^2 b_z^2}}\left[\lambda b_x - \frac{i}{2}\lambda^2 \frac{(-3\varphi''_{xx} M_{1x} - \varphi''_{zz} b_x M_{1a} - 2\varphi''_{xz} b_z M_{1b})}{(1+\lambda^2 b_x^2 + \lambda^2 b_z^2)^{5/2}}\right] + \mathcal{O}\left(\frac{\lambda^2}{\lambda_l^2}\right) \\
T_{1,z}(x,z,t) &\approx e^{i\varphi}\frac{1}{\sqrt{1+\lambda^2 b_x^2+\lambda^2 b_z^2}}\left[\lambda b_z - \frac{i}{2}\lambda^2 \frac{(-3\varphi''_{zz} M_{1z} - \varphi''_{zz} b_z M_{1b} - 2\varphi''_{xz} b_x M_{1a})}{(1+\lambda^2 b_x^2 + \lambda^2 b_z^2)^{5/2}}\right] + \mathcal{O}\left(\frac{\lambda^2}{\lambda_l^2}\right)
\end{aligned} \tag{A.20}$$

$$\begin{aligned}
M_{1x} &= \lambda b_x(1+\lambda^2 b_z^2), \quad M_{1z} = \lambda b_z(1+\lambda^2 b_x^2) \\
M_{1a} &= (\lambda^2 b_x^2 - 2\lambda^2 b_z^2 + 1), \quad M_{1b} = (\lambda^2 b_z^2 - 2\lambda^2 b_x^2 + 1)
\end{aligned} \tag{A.21}$$

$$\begin{aligned}
T_{2,xx}(x,z,t) &\approx e^{i\varphi}\frac{1+\lambda^2 b_z^2}{[1+\lambda^2 b_x^2 + \lambda^2 b_z^2]^{3/2}} - \frac{i}{2}\frac{\lambda^2\left[\varphi''_{xx} M_{2x^4} + \varphi''_{zz} M_{2x^2z^2} + 2\varphi''_{xz} M_{2x^3z}\right]}{[1+\lambda^2 b_x^2 + \lambda^2 b_z^2]^{7/2}} + \mathcal{O}\left(\frac{\lambda^2}{\lambda_l^2}\right) \\
T_{2,zz}(x,z,t) &\approx e^{i\varphi}\frac{1+\lambda^2 b_x^2}{[1+\lambda^2 b_x^2 + \lambda^2 b_z^2]^{3/2}} - \frac{i}{2}\frac{\lambda^2\left[\varphi''_{xx} M_{2x^2z^2} + \varphi''_{zz} M_{2z^4} + 2\varphi''_{xz} M_{2xz^3}\right]}{[1+\lambda^2 b_x^2 + \lambda^2 b_z^2]^{7/2}} + \mathcal{O}\left(\frac{\lambda^2}{\lambda_l^2}\right) \\
T_{2,xz}(x,z,t) &\approx e^{i\varphi}\frac{-\lambda^2 b_x b_z}{[1+\lambda^2 b_x^2 + \lambda^2 b_z^2]^{3/2}} - \frac{i}{2}\frac{\lambda^2\left[\varphi''_{xx} M_{2x^3z} + \varphi''_{zz} M_{2xz^3} + 2\varphi''_{xz} M_{2x^2z^2}\right]}{[1+\lambda^2 b_x^2 + \lambda^2 b_z^2]^{7/2}} + \mathcal{O}\left(\frac{\lambda^2}{\lambda_l^2}\right)
\end{aligned} \tag{A.22}$$

$$\begin{aligned}
M_{2x^4} &= 3(1+\lambda^2 b_z^2)(4\lambda^2 b_x^2 - \lambda^2 b_z - 1), \quad M_{2xz^3} = 3\lambda^2 b_x b_z(3+3\lambda^2 b_x^2 - 2\lambda^2 b_z^2) \\
M_{2z^4} &= 3(1+\lambda^2 b_x^2)(4\lambda^2 b_z^2 - \lambda^2 b_x^2 - 1), \quad M_{2x^3z} = 3\lambda^2 b_x b_z(3+3\lambda^2 b_z^2 - 2\lambda^2 b_x^2) \\
M_{2x^2z^2} &= (2\lambda^4 b_x^4 + 2\lambda^4 b_z^4 + \lambda^2 b_x^2 + \lambda^2 b_z^2 - 11\lambda^4 b_x^2 b_z^2 - 1)
\end{aligned} \tag{A.23}$$

$$W_0(x,z,t) \approx e^{i\varphi}\lambda^2 \frac{b_x b_z}{[1+\lambda^2 b_x^2 + \lambda^2 b_z^2]^{3/2}} + \mathcal{O}\left(\frac{\lambda^2}{\lambda_l^2}\right) \tag{A.24}$$

A.3 Appendix C

The programming code for both scaling method and standard TDDE [25] solution, along with the corresponding data and figures can be accessed via a link: `https://github.com/arboec/relativistic_ionization_1D`

Hardware specifications. For 1D calculations: Intel(R) Core(TM) i7-2600 CPU @ 3.40GHz; 16 GB RAM. For 2D calculations: AMD EPYC 9654 96-Core Processor; 1584 GB RAM (shared).

Software specifications. For 1D calculations: MATLAB(R) 2022b; no explicit parallelization was used. For 2D calculations: C++, Eigen library was used for matrix-vector operations; openMP for parallelization; Intel(R) oneAPI Math Kernel Library for implementing FFT. Bound states for the soft-Coulomb potential were calculated with MATSLISE package [65].

There are also parameters, which are used in the course of the simulations, but are not explicitly mentioned in Sec. 3.1.2 or Sec. 3.2. The first of them is a tolerance ϵ_{tol}, used to compute an approximation to the matrix exponent by means of Krylov-Arnoldi method [78]. The typical for ϵ_{tol} value was $\epsilon_{\text{tol}} \sim 10^{-6} - 10^{-8}$. The second one is responsible for the frequency of updating a mesh. As was mentioned in Sec. 3.2, in case of a non-uniform mesh, one can add additional nodes to the mesh, as expansion factor $R(t)$ grows. However, adding nodes requires an interpolation, which may lead to the occurrence of numerical artifacts. For the parameters used, we employed a simple procedure, which triggers mesh refinement every time $t_{\text{new ref}}$ when $R(t_{\text{new ref}}) = 1.05 \cdot R(t_{\text{previous ref}})$. Such a choice of parameters allows us to keep the magnitude of artifacts at the level, which does not influence the results of computations.

Method	Δt, a.u.	t_{comp}, minutes	ϵ_{tol}	Diff.$\cdot 10^{-2}$, a.u.
Dirac	10^{-4}	30	-	-57.1
Dirac	10^{-5}	290	-	1.10
Dirac	$5 \cdot 10^{-6}$	576	-	0.28
Dirac	$2.5 \cdot 10^{-6}$	1194	-	0.07
Scaled FW	10^{-3}	97	10^{-7}	-0.34
Scaled FW	10^{-4}	190	10^{-6}	0.02

Table A.1: A supplementary table to Fig. 3.5. The quantity "Difference" is defined as $\langle x_{\text{Dirac}} \rangle - \langle x_{\text{SKGE}} \rangle$ or $\langle x_{\text{FW}} \rangle - \langle x_{\text{SKGE}} \rangle$ at the end of simulation.

A.4 Appendix D

Then the question may arise why the scaling method accuracy is deteriorated for the scattered part of the wavepacket. The matter is the change of the phase of the wavepacket at scattering. In the scaling method, the phase of the wave function originating from the kinetic (ballistic) propagation is accurately canceled, irrespective of the range of this velocities. As was illustrated on Figs. 3.1-3.4, all the components of the wave function, regardless of their v, will lose their kinetic phase and stop. The phase cancellation and related inaccuracies arises when the wave packet acquires an additional scattering phase. In this case the kinetic phase cancellation is described only in an approximated manner in our method. This is illustrated in Fig. A1 (not an actual simulation).

In this scenario, a wavepacket impinges from the left (blue) to the localized at $\xi = 0$ potential and scatters, producing the transferred wave packet (red) and the scattered one (green). After the application of the scaling method, see Fig. A2, the blue and red wave packets are smooth, but the scattered one is not. The latter breaks the assumption for the expansion of Eq. (3.13).. This happens because the kinetic phase is not canceled properly, since we rely on the procedure of Algorithm 1.

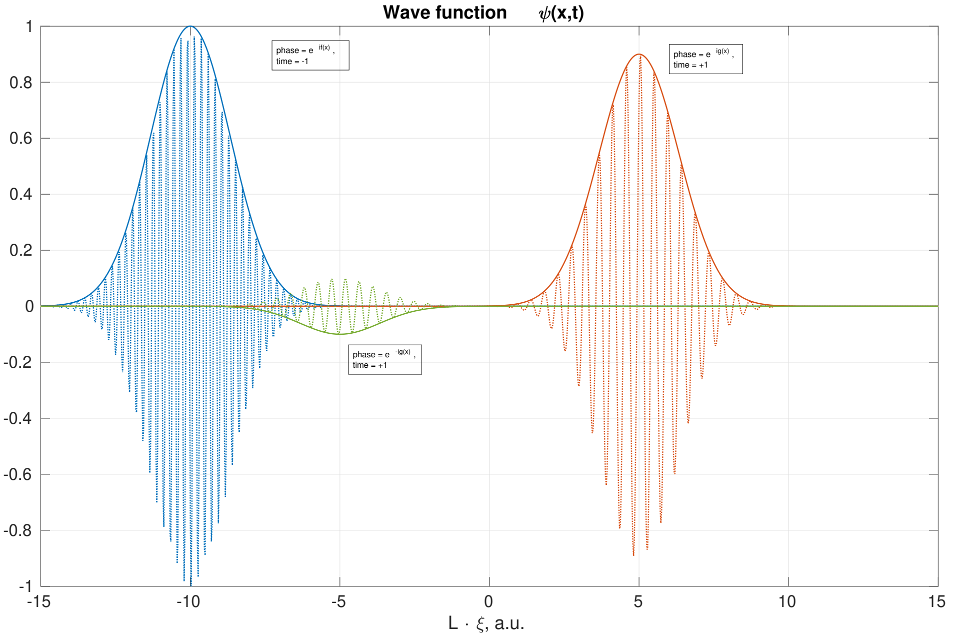

Fig. A1: A scheme of a scattering process (not an actual simulation). No scaling is applied.

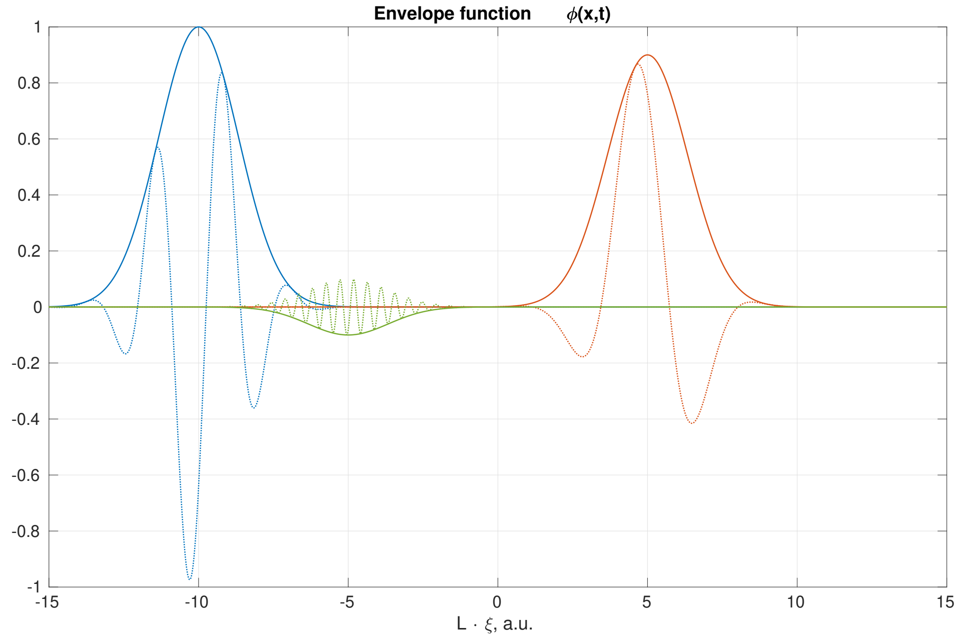

Fig. A2: A scheme of a scattering process (not an actual simulation). Scaling is applied and an "envelope" function ϕ is depicted.

The procedure is good for the prediction of the ballistic propagation, but does not include the scattering phase. As a result, the evolution of the scattered part is not described accurately. Eventually, at asymptotic large times $t \to \infty$, both green and red packets will stop, because the kinetic phase will prevail. However, the accuracy of the description will be determined by the accuracy of the applied order of the v/c-expansion in Eq. (3.13).

Publications

Regarding the content of the Chapter 3, one article has been published in a peer reviewed journal:

- A. V. Boitsov, K. Z. Hatsagortsyan and C. H. Keitel
  Scaling method for the numerical solution of the strong-field ionization problem in the relativistic regime. Computer Physics Communications, 310: 109511 (2025). doi:10.1016/j.cpc.2025.109511

While another article summarizing the content of the Chapter 4 is in preparation:

- A. V. Boitsov, K. Z. Hatsagortsyan and C. H. Keitel
  Relativistic scaling method for the numerical simulation of the x-ray strong field ionization

Bibliography

[1] P. B. Corkum and F. Krausz. Attosecond science. *Nature Phys.*, 3:381, 2007.

[2] F. Krausz and M. Ivanov. Attosecond physics. *Rev. Mod. Phys.*, 81:163, 2009.

[3] Jin Woo Yoon, Yeong Gyu Kim, Il Woo Choi, Jae Hee Sung, Hwang Woon Lee, Seong Ku Lee, and Chang Hee Nam. Realization of laser intensity over 10^{23} W/cm^2. *Optica*, 8(5):630, may 2021.

[4] A. Di Piazza, C. Müller, K. Z. Hatsagortsyan, and C. H. Keitel. Extremely high-intensity laser interactions with fundamental quantum systems. *Rev. Mod. Phys.*, 84:1177, 2012.

[5] C. I. Moore, A. Ting, S. J. McNaught, J. Qiu, H. R. Burris, and P. Sprangle. A laser-accelerator injector based on laser ionization and ponderomotive acceleration of electrons. *Phys. Rev. Lett.*, 82:1688, 1999.

[6] Enam A. Chowdhury, C. P. J. Barty, and Barry C. Walker. “nonrelativistic” ionization of the L-shell states in argon by a “relativistic” 10^{19} w/cm^2 laser field. *Phys. Rev. A*, 63:042712, 2001.

[7] Matthias Dammasch, Martin Dörr, Ulli Eichmann, Ernst Lenz, and Wolfgang Sandner. Relativistic laser-field-drift suppression of nonsequential multiple ionization. *Phys. Rev. A*, 64:061402, 2001.

[8] K. Yamakawa, Y. Akahane, Y. Fukuda, M. Aoyama, N. Inoue, and H. Ueda. Ionization of many-electron atoms by ultrafast laser pulses with peak intensities greater than 10^{19} w/cm^2. *Phys. Rev. A*, 68:065403, 2003.

[9] A. Maltsev and T. Ditmire. Above threshold ionization in tightly focused, strongly relativistic laser fields. *Phys. Rev. Lett.*, 90:053002, Feb 2003.

[10] A. D. DiChiara, I. Ghebregziabher, R. Sauer, J. Waesche, S. Palaniyappan, B. L. Wen, and B. C. Walker. Relativistic mev photoelectrons from the single atom response of argon to a 10^{19} w/cm^2 laser field. *Phys. Rev. Lett.*, 101:173002, 2008.

[11] A. Yandow, T. N. Ha, C. Aniculaesei, H. L. Smith, C. G. Richmond, M. M. Spinks, H. J. Quevedo, S. Bruce, M. Darilek, C. Chang, D. A. Garcia, E. Gaul, M. E. Donovan, B. M. Hegelich, and T. Ditmire. Above-threshold ionization at laser intensity greater than $10^{20}\mathrm{W/cm}^2$. *Phys. Rev. A*, 109:023119, Feb 2024.

[12] C. T. L. Smeenk, L. Arissian, B. Zhou, A. Mysyrowicz, D. M. Villeneuve, A. Staudte, and P. B. Corkum. *Phys. Rev. Lett.*, 106:193002, 2011.

[13] A. Ludwig, J. Maurer, B. W. Mayer, C. R. Phillips, L. Gallmann, and U. Keller. Breakdown of the dipole approximation in strong-field ionization. *Phys. Rev. Lett.*, 113:243001, 2014.

[14] Alexander Hartung, Felipe Morales, Maksim Kunitski, Kevin Henrichs, Alina Laucke, Martin Richter, Till Jahnke, Anton Kalinin, Markus Schöffler, Lothar Ph. H. Schmidt, M Ivanov, O Smirnova, and R Dörner. Electron spin polarization in strong-field ionization of xenon atoms. *Nature Photonics*, 10(8):526–528, 2016.

[15] B Willenberg, J Maurer, Benedikt W. Mayer, and U Keller. Sub-cycle time resolution of multi-photon momentum transfer in strong-field ionization. *Nat. Commun.*, 10:5548, 2019.

[16] A. Hartung, S. Eckart, S. Brennecke, J. Rist, D. Trabert, K. Fehre, M. Richter, H. Sann, S. Zeller, K. Henrichs, et al. Magnetic fields alter strong-field ionization. *Nat. Phys.*, 15(12):1222–1226, 2019.

[17] S. Grundmann, D. Trabert, K. Fehre, N. Strenger, A. Pier, L. Kaiser, M. Kircher, M. Weller, S. Eckart, L. Ph. H. Schmidt, F. Trinter, T. Jahnke, M. S. Schöffler, and R. Dörner. Zeptosecond birth time delay in molecular photoionization. *Science*, 370(6514):339–341, 2020.

[18] R.M. Potvliege C.J. Joachain, N.J. Kylstra. *Atoms in Intense Laser Fields.* Cambridge University Press, 2012.

[19] R Reiff, T Joyce, A Jaroń-Becker, and A Becker. Single-active electron calculations of high-order harmonic generation from valence shells in atoms for quantitative comparison with tddft calculations. *Journal of Physics Communications*, 4(6):065011, jun 2020.

[20] Vladimir S Popov. Tunnel and multiphoton ionization os atoms and ions in a strong laser field. *Phys. Usp.*, 47:855, 2004.

[21] H. R. Reiss. Complete Keldysh theory and its limiting cases. *Phys. Rev. A*, 42:1476, 1990.

[22] B. Hafizi, D. F. Gordon, and J. P. Palastro. First benchmark of relativistic photoionization theories against 3d ab initio simulation. *Phys. Rev. Lett.*, 118:133201, Mar 2017.

[23] Michael Klaiber, Karen Z. Hatsagortsyan, and Christoph H. Keitel. Generalized analytical description of relativistic strong-field ionization. *Phys. Rev. A*, 110:023103, 2024.

[24] Michael Klaiber, Enderalp Yakaboylu, Heiko Bauke, Karen Z. Hatsagortsyan, and Christoph H. Keitel. Under-the-barrier dynamics in laser-induced relativistic tunneling. *Phys. Rev. Lett.*, 110:153004, 2013.

[25] Heiko Bauke. Time-dependent relativistic wave equations: Numerics of the dirac and the klein-gordon equation. In Dieter Bauer, editor, *Computational Strong-Field Quantum Dynamics*, pages 77–110. De Gruyter, 2017.

[26] X. Antoine and E. Lorin. Computational performance of simple and efficient sequential and parallel dirac equation solvers. *Computer Physics Communications*, 220:150–172, 2017.

[27] J. W. Braun, Q. Su, and R. Grobe. Numerical approach to solve the time-dependent dirac equation. *Phys. Rev. A*, 59:604–612, Jan 1999.

[28] Jia Yin. A fourth-order compact time-splitting method for the Dirac equation with time-dependent potentials. 6 2021.

[29] Weizhu Bao, Yongyong Cai, Xiaowei Jia, and Qinglin Tang. A uniformly accurate multiscale time integrator pseudospectral method for the dirac equation in the nonrelativistic limit regime. *SIAM Journal on Numerical Analysis*, 54(3):1785–1812, 2016.

[30] Weizhu Bao, Yongyong Cai, and Xiaowei Jiao. Numerical methods and comparison for the dirac equation in the nonrelativistic limit regime. *Journal of Scientific Computing*, 71, 06 2017.

[31] Weizhu Bao and Jia Yin. A fourth-order compact time-splitting fourier pseudospectral method for the dirac equation. *Research in the Mathematical Sciences*, 6, 12 2018.

[32] Weizhu Bao, Yongyong Cai, and Yue Feng. Improved uniform error bounds on time-splitting methods for the long-time dynamics of the weakly nonlinear dirac equation. *IMA Journal of Numerical Analysis*, 44, 05 2023.

[33] S. X. Hu and C. H. Keitel. Spin signatures in intense laser-ion interaction. *Phys. Rev. Lett.*, 83:4709, 1999.

[34] C. H. Keitel and S. X. Hu. Coherent x-ray pulse generation in the sub-Ångström regime. *Appl. Phys. Lett.*, 80:541, 2002.

[35] M. W. Walser, D. J. Urbach, K. Z. Hatsagortsyan, S. X. Hu, and C. H. Keitel. Spin and radiation in intense laser fields. *Phys. Rev. A*, 65:043410, 2002.

[36] N J Kylstra, A M Ermolaev, and C J Joachain. Relativistic effects in the time evolution of a one-dimensional model atom in an intense laser field. *Journal of Physics B: Atomic, Molecular and Optical Physics*, 30(13):L449, jul 1997.

[37] M. Boca and V. Florescu. Relativistic effects in the time evolution of an one-dimensional model atom in a laser pulse. *The European Physical Journal D*, 46:15–20, 2008.

[38] Guido R Mocken and Christoph H Keitel. Bound atomic dynamics in the mev regime. *J. Phys. B*, 37:L275, 2004.

[39] Guido R. Mocken and Christoph H. Keitel. Fft-split-operator code for solving the dirac equation in 2+1 dimensions. *Computer Physics Communications*, 178(11):868–882, 2008.

[40] Randolf Beerwerth and Heiko Bauke. Krylov subspace methods for the dirac equation. *Computer Physics Communications*, 188:189–197, 2015.

[41] H. G. Hetzheim and C. H. Keitel. Ionization dynamics versus laser intensity in laser-driven multiply charged ions. *Phys. Rev. Lett.*, 102:083003, 2009.

[42] Heiko Bauke, Henrik G. Hetzheim, Guido R. Mocken, Matthias Ruf, and Christoph H. Keitel. Relativistic ionization characteristics of laser-driven hydrogenlike ions. *Phys. Rev. A*, 83:063414, Jun 2011.

[43] M. S. Pindzola, Sh. A. Abdel-Naby, F. Robicheaux, and J. Colgan. Single photoionization of highly charged atomic ions including the full electromagnetic-field potential. *Phys. Rev. A*, 85:032701, Mar 2012.

[44] Yulian V. Vanne and Alejandro Saenz. Solution of the time-dependent dirac equation for multiphoton ionization of highly charged hydrogenlike ions. *Phys. Rev. A*, 85:033411, Mar 2012.

[45] Tor Kjellsson, Sølve Selstø, and Eva Lindroth. Relativistic ionization dynamics for a hydrogen atom exposed to superintense xuv laser pulses. *Phys. Rev. A*, 95:043403, Apr 2017.

[46] I. A. Ivanov. Spin-flip processes and nondipole effects in above-threshold ionization of hydrogen in ultrastrong laser fields. *Phys. Rev. A*, 96:013419, Jul 2017.

[47] Dmitry A. Telnov and Shih-I Chu. Relativistic ionization dynamics of hydrogen-like ions in strong electromagnetic fields: Generalized pseudospectral method for the time-dependent dirac equation. *Phys. Rev. A*, 102:063109, Dec 2020.

[48] Johanne Elise Vembe, Esther A. B. Johnsen, and Morten Førre. Relativistic and nondipole effects in multiphoton ionization of hydrogen by a high-intensity x-ray laser pulse. *Phys. Rev. A*, 109:013107, Jan 2024.

[49] Lei Geng, Hao Liang, Zi-Yang Lin, and Liang-You Peng. Solving the time-dependent klein-gordon and square-root klein-gordon equations with krylov-subspace methods. *Phys. Rev. A*, 107:053115, May 2023.

[50] Sang Tae Park. Propagation of a relativistic electron wave packet in the dirac equation. *Phys. Rev. A*, 86:062105, Dec 2012.

[51] Sølve Selstø, Eva Lindroth, and Jakob Bengtsson. Solution of the dirac equation for hydrogenlike systems exposed to intense electromagnetic pulses. *Phys. Rev. A*, 79:043418, Apr 2009.

[52] Armin Scrinzi. Infinite-range exterior complex scaling as a perfect absorber in time-dependent problems. *Phys. Rev. A*, 81:053845, May 2010.

[53] U. V. Riss and H.-D. Meyer. Investigation on the reflection and transmission properties of complex absorbing potentials. *The Journal of Chemical Physics*, 105(4):1409–1419, 07 1996.

[54] Tor Kjellsson, Morten Førre, Aleksander Skjerlie Simonsen, Sølve Selstø, and Eva Lindroth. Alternative gauge for the description of the light-matter interaction in a relativistic framework. *Phys. Rev. A*, 96:023426, Aug 2017.

[55] E A Soloviev and S I Vinitsky. Suitable coordinates for the three-body problem in the adiabatic representation. *Journal of Physics B: Atomic and Molecular Physics*, 18(16):L557, aug 1985.

[56] E. Y. Sidky and B. D. Esry. Boundary-free propagation with the time-dependent schrödinger equation. *Phys. Rev. Lett.*, 85:5086–5089, Dec 2000.

[57] Z. X. Zhao, B. D. Esry, and C. D. Lin. Boundary-free scaling calculation of the time-dependent schrödinger equation for laser-atom interactions. *Phys. Rev. A*, 65:023402, Jan 2002.

[58] Vladimir Roudnev and B. D. Esry. HD^+ photodissociation in the scaled coordinate approach. *Phys. Rev. A*, 71:013411, Jan 2005.

[59] Alexander Ya. Silenko. Comparative analysis of direct and "step-by-step" foldy-wouthuysen transformation methods. *Theoretical and Mathematical Physics*, 176:987, 2013.

[60] Alexander J. Silenko. General method of the relativistic foldy-wouthuysen transformation and proof of validity of the foldy-wouthuysen hamiltonian. *Phys. Rev. A*, 91:022103, Feb 2015.

[61] Alexander J. Silenko. General properties of the foldy-wouthuysen transformation and applicability of the corrected original foldy-wouthuysen method. *Phys. Rev. A*, 93:022108, 2016.

[62] I.P. Omelyan, I.M. Mryglod, and R. Folk. Symplectic analytically integrable decomposition algorithms: classification, derivation, and application to molecular dynamics, quantum and celestial mechanics simulations. *Computer Physics Communications*, 151(3):272–314, 2003.

[63] Steven G. Johnson. Notes on fft-based differentiation. *MIT Applied Mathematics*, April 2011.

[64] John P. Boyd. Dover Publications, Inc., 2000.

[65] Veerle Ledoux and Marnix Van Daele. Matslise 2.0: A matlab toolbox for sturm-liouville computations. *ACM Transactions on Mathematical Software*, 42:1–18, 06 2016.

[66] Edwin M. McMillan. The origin of cosmic rays. *Phys. Rev.*, 79:498–501, Aug 1950.

[67] A. H. Nayfeh. *Introduction to Perturbation Techniques.* Wiley-lnterscience, N.Y., 1993.

[68] Leslie L. Foldy and Siegfried A. Wouthuysen. On the dirac theory of spin 1/2 particles and its non-relativistic limit. *Phys. Rev.*, 78:29–36, Apr 1950.

[69] Alexander J. Silenko. Foldy-wouthyusen transformation and semiclassical limit for relativistic particles in strong external fields. *Phys. Rev. A*, 77:012116, 2008.

[70] Erik Eriksen. Foldy-wouthuysen transformation. exact solution with generalization to the two-particle problem. *Phys. Rev.*, 111:1011–1016, Aug 1958.

[71] V. B. Berestetskii, , E. M. Lifshitz, and L. P. Pitevskii. *Quantum electrodynamics.* Pergamon, Oxford, 1982.

[72] Dmitry A. Telnov and Shih-I Chu. Relativistic ionization probabilities and photoelectron distributions of hydrogenlike ions in superstrong electromagnetic fields. *Phys. Rev. A*, 104:023111, 2021.

[73] Alexander J. Silenko. Leading correction to the relativistic foldy-wouthuysen hamiltonian. *Phys. Rev. A*, 111:032210, Mar 2025.

[74] F. D. Tappert and Michael G. Brown. Asymptotic phase errors in parabolic approximations to the one-way helmholtz equation. *The Journal of the Acoustical Society of America*, 99(3):1405–1413, 03 1996.

[75] Mark R. Hermann and J. A. Fleck. Split-operator spectral method for solving the time-dependent schrödinger equation in spherical coordinates. *Phys. Rev. A*, 38:6000–6012, 1988.

[76] Masuo Suzuki. General decomposition theory of ordered exponentials. *Proceedings of the Japan Academy, Series B*, 69(7):161–166, 1993.

[77] David A Kopriva. *Implementing spectral methods for partial differential euqations.* Springer, 2009.

[78] Mikhail A. Bochev. *A short guide to exponential Krylov subspace time integration for Maxwell's equations.* Number 1992 in Memorandum. University of Twente, Netherlands, September 2012.

[79] S. Palaniyappan, I. Ghebregziabher, A. DiChiara, J. MacDonald, and B. C. Walker. Emergence from nonrelativistic strong-field rescattering to ultrastrong-field laser-atom physics: A semiclassical analysis. *Phys. Rev. A*, 74:033403, 2006.

[80] M Klaiber, K Z Hatsagortsyan, J Wu, S S Luo, P Grugan, and B C Walker. Limits of Strong Field Rescattering in the Relativistic Regime. *Phys. Rev. Lett.*, 118(9):093001, 2017.

[81] D. F. Gordon, J. P. Palastro, and B. Hafizi. Superponderomotive regime of tunneling ionization. *Phys. Rev. A*, 95:033403, 2017.

[82] Michael Klaiber, Enderalp Yakaboylu, Carsten Müller, Heiko Bauke, Gerhard G Paulus, and Karen Z Hatsagortsyan. Spin dynamics in relativistic ionization with highly charged ions in super-strong laser fields. *J. Phys. B*, 47(6):065603, 2014.

[83] Mihai Gavrila. Atomic stabilization in superintense laser fields. *Journal of Physics B: Atomic, Molecular and Optical Physics*, 35(18):R147, sep 2002.

[84] A Patel, N J Kylstra, and P L Knight. Effect of laser pulse shapes on the stabilization of a model atom. 32(24):5759, dec 1999.

[85] M Protopapas, C H Keitel, and P L Knight. Relativistic mass shift effects in adiabatic intense laser field stabilization of atoms. *Journal of Physics B: Atomic, Molecular and Optical Physics*, 29(16):L591, 1996.

[86] L. N. Gaier and C. H. Keitel. Relativistic classical monte carlo simulations of stabilization of hydrogenlike ions in intense laser pulses. *Phys. Rev. A*, 65:023406, 2002.

[87] Andreas Staudt and Christoph H Keitel. Stabilization of helium in intense high-frequency laser pulses beyond the dipole approximation. *Journal of Physics B: Atomic, Molecular and Optical Physics*, 36(13):L203, jun 2003.

[88] M Protopapas, C H Keitel, and P L Knight. Atomic physics with super-high intensity lasers. *Reports on Progress in Physics*, 60(4):389, 1997.

[89] Darko Dimitrovski, Morten Førre, and Lars Bojer Madsen. Strong-field short-pulse nondipole dynamics. *Phys. Rev. A*, 80:053412, Nov 2009.

[90] M. Dondera and H. Bachau. Exploring above-threshold ionization of hydrogen in an intense x-ray laser field through nonperturbative calculations. *Phys. Rev. A*, 85:013423, Jan 2012.

[91] Michael Klaiber, Karen Z. Hatsagortsyan, and Christoph H. Keitel. Above-threshold ionization beyond the dipole approximation. *Phys. Rev. A*, 71(3):033408, 2005.

[92] Michael Klaiber, Karen Z. Hatsagortsyan, and Christoph H. Keitel. Relativistic ionization rescattering with tailored laser pulses. *Phys. Rev. A*, 74:051803, 2006.

[93] Zhongyuan Zhou and Shih-I Chu. Multiphoton above-threshold ionization in superintense free-electron x-ray laser fields: Beyond the dipole approximation. *Phys. Rev. A*, 87:023407, Feb 2013.

[94] M. Førre, J. P. Hansen, L. Kocbach, S. Selstø, and L. B. Madsen. Nondipole ionization dynamics of atoms in superintense high-frequency attosecond pulses. *Phys. Rev. Lett.*, 97:043601, Jul 2006.

[95] Volker Mosert and Dieter Bauer. Photoelectron spectra with qprop and t-surff. *Computer Physics Communications*, 207:452–463, 2016.

[96] F Morales, T Bredtmann, and S Patchkovskii. isurf: a family of infinite-time surface flux methods. 49(24):245001, nov 2016.

[97] L. D. Landau and E. M. Lifshitz. *Quantum Mechanics.* Pergamon, Oxford, 1977. Chapt.53.

[98] C. H. Keitel and P. L. Knight. Monte carlo classical simulations of ionization and harmonic generation in the relativistic domain. *Phys. Rev. A*, 51:1420–1430, 1995.

[99] Charles W Clark. Closed-form solutions of the schrödinger equation for a class of smoothed coulomb potentials. *Journal of Physics B: Atomic, Molecular and Optical Physics*, 30(11):2517, jun 1997.

[100] Sajad Azizi, Ulf Saalmann, and Jan M. Rost. Zero-energy photoelectric effect. *Phys. Rev. Lett.*, 134:103201, 2025.

[101] Wei-Chao Jiang and Joachim Burgdörfer. Dynamic interference as signature of atomic stabilization. *Opt. Express*, 26(16):19921–19931, 2018.

[102] Molei Tao. Explicit high-order symplectic integrators for charged particles in general electromagnetic fields. *Journal of Computational Physics*, 327:245–251, 2016.

Acknowledgements

I am very grateful to my supervisor, Karen Z. Hatsagortsyan, for his continuous help. Also, I thank Prof. Christoph H. Keitel for providing me with an opportunity to work in Max Planck Institute for Nuclear Physics and for the review of my thesis. In addition, I thank Sibel Babacan and Denitsa Dzhigova for their help with organizational matters.

I appreciate a will of Thomas Gasenzer to review my thesis, as well as Christian Ott and Werner Aeschbach participation in my thesis committee.

I would also like to thank my former supervisors: Kálmán K. Szabó, Vitaly A. Gradusov, Vladimir A. Roudnev, Sergei P. Merts and Sergei A. Nemnyugin.

I am very thankful to my mother, father, brother and to all my family, as well as to my friends and colleagues for their support during my PhD studies.